

REPORT DOCUMENTATION PAGE			Form Approved OMB No. 0704-0188	
Public reporting burden for this collection of information is estimated to average 1 hour per response, including the time for reviewing instructions, searching existing data sources, gathering and maintaining the data needed, and completing and reviewing the collection of information. Send comments regarding this burden estimate or any other aspect of this collection of information, including suggestions for reducing this burden, to Washington Headquarters Services, Directorate for Information Operations and Reports, 1215 Jefferson Davis Highway, Suite 1204, Arlington, VA 22202-4302, and to the Office of Management and Budget, Paperwork Reduction Project (0704-0188), Washington, DC 20503.				
1. AGENCY USE ONLY (Leave blank)		2. REPORT DATE 7 August 1998		3. REPORT TYPE AND DATES COVERED
4. TITLE AND SUBTITLE Development and Evaluation of a New Spectral Planetary Boundary-Layer Architecture for the MM5			5. FUNDING NUMBERS	
6. AUTHOR(S) Daniel T. Pawlak				
7. PERFORMING ORGANIZATION NAME(S) AND ADDRESS(ES) The Pennsylvania State University			8. PERFORMING ORGANIZATION REPORT NUMBER  98-047	
9. SPONSORING/MONITORING AGENCY NAME(S) AND ADDRESS(ES) THE DEPARTMENT OF THE AIR FORCE AFIT/CIA, BLDG 125 2950 P STREET WPAFB OH 45433			10. SPONSORING/MONITORING AGENCY REPORT NUMBER	
11. SUPPLEMENTARY NOTES				
12a. DISTRIBUTION AVAILABILITY STATEMENT Unlimited distribution In Accordance With 35-205/AFIT Sup 1			12b. DISTRIBUTION CODE	
13. ABSTRACT (Maximum 200 words)				
14. SUBJECT TERMS			15. NUMBER OF PAGES 102	
			16. PRICE CODE	
17. SECURITY CLASSIFICATION OF REPORT	18. SECURITY CLASSIFICATION OF THIS PAGE	19. SECURITY CLASSIFICATION OF ABSTRACT	20. LIMITATION OF ABSTRACT	

The Pennsylvania State University

The Graduate School

Department of Meteorology

Development and Evaluation of a New Spectral  
Planetary Boundary-Layer Architecture  
for the MM5

A Thesis in

Meteorology

by

Daniel T. Pawlak

Submitted in Partial Fulfillment  
of the Requirements  
for the Degree of

Master of Science

May 1998

DTIC QUALITY INSPECTED 1

19980811 136


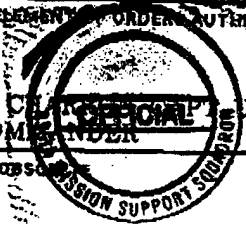
## ABSTRACT

The Otte-Wyngaard spectral PBL architecture, which represents the vertical structure of mean variables in the PBL with a truncated series of Legendre polynomials, is inserted within the framework of the non-hydrostatic, three-dimensional Penn State/National Center for Atmospheric Research Mesoscale Model version 5.2 (MM5). It is important to note that the focus of this work is the new spectral *architecture*, and that the specific closure used within this general framework can easily be changed. Preliminary experiments found that the prognostic equation for PBL height employed by the spectral model is inappropriate during deep convection. Therefore, two algorithms for PBL height *diagnosis* were tested, at gridpoints experiencing deep convection as well as for initialization of the PBL height field for the prognostic equation.

A comparison between the spectral model and two "high-resolution" models, the Blackadar and Gayno-Seaman models, is performed using two cases: an idealized coastal-zone domain with a single-sounding initialization, and a real-data case focused on the U.S. Department of Energy Atmospheric Radiation Measurement Southern Great Plains Cloud and Radiation Testbed (ARM-CART) during an intense observation period from 0000 UTC 12 April 1997 to 0000 UTC 14 April 1997. Special data from the ARM-CART site were used for independent verification.

Experimental results show that the spectral model within MM5 produces realistic vertical structure within the boundary layer, comparable to that of the other two PBL

models, and computationally, the spectral model is several times faster than the other "high-resolution" models.

1. LAST, FIRST, MIDDLE Initial <b>1LT PAWLAK DANIEL T</b>		2. SSN <b>083564099</b>	3. SDAFSC/CAFSC <b>015W1</b>
4. SECURITY CLEARANCE (Include date of last investigation) <b>DCID 1/14 SSBI 950314</b>		5. REPORT TO COMDR. NEW ASSIGNMENT <b>NLT 980630</b>	6. TRAVEL DAYS AUTHORIZED IF TRAVELING BY PRIVATELY OWNED CONVEYANCE
7. TDY ENROUTE			
8. UNIT, MAJOR COMMAND, AND ADDRESS OF UNIT TO WHICH ASSIGNED <b>HQ WEATHER AGENCY (AWS) OFFUTT AFB NE 68113</b>		9. UNIT, MAJOR COMMAND, AND ADDRESS OF UNIT FROM WHICH RELIEVED <b>AF INST OF TECH (AETC) STATE COLLEGE CITY PA 16806</b>	
10. TYPE OF TOUR (Check One)	<input type="checkbox"/> ACCOMPANIED <input type="checkbox"/> UNACCOMPANIED <input type="checkbox"/> UNACCOMPANIED, DEPENDENTS RESTRICTED	11. TOUR LENGTH (Total No. of Months)	12. EXTENDED LONG TOUR VOL <input type="checkbox"/>
13. DEPENDENT TRAVEL <input type="checkbox"/> A. CONCURRENT TRAVEL IS AUTOMATIC <input type="checkbox"/> B. CONCURRENT TRAVEL IS APPROVED <input type="checkbox"/> C. NONCONCURRENT TRAVEL IS AUTHORIZED IN LESS THAN 20 WEEKS <input type="checkbox"/> D. NONCONCURRENT TRAVEL IS AUTHORIZED IN MORE THAN 20 WEEKS <input type="checkbox"/> E. TRAVEL IS AUTHORIZED TO A DESIGNATED PLACE		14. THIS IS A JOIN-SPOUSE ASSIGNMENT (Include spouse's grade, name and SSN) <input type="checkbox"/>	
15. AUTHORITY FOR CCTVL		16. HOMEBASING/FOLLOW-ON ASSIGNMENT (Include AAN, GPAS, and RNLTD)	
17. DEPENDENT(s): (List names, DOB of Children, relationship to member and current address) <b>DEBRA I/SPOUSE RD# 1 BOX 362 FORT MATILDA PA 16870</b>		18. DEPARTURE CERTIFICATION: I certify that to the best of my knowledge I will depart PCS at ____ (hrs) ____ (date)  (Signature)	
19. OVERSEAS TRANSPORTATION DATA			
<input checked="" type="checkbox"/> X	A. Comply with MTA (DD Form 1882)	<input type="checkbox"/> C. TDY station will obtain flight reservations. Member is not authorized to depart TDY station before receipt of validated MTA or GTR (SF1169) from the TMO.	
<input checked="" type="checkbox"/> X	B. Member will comply with reporting date and flight reservations in the MTA or as arranged by the TMO per AFI 24-10, and is not authorized to depart this station before receipt of validated MTA or GTR (SF1169) from the TMO.	<input type="checkbox"/> D. Dependent(s) will comply with reporting date and flight reservations in the MTA.	
20. PCS EXPENSE CHARGEABLE TO <b>5783500 328 5752.0*875825</b> CIC: NONTEMPORARY STORAGE CHARGEABLE TO: <b>5783500 328 5758.ON 875825</b>		(Insert M.D.N.I.G.F.A.S.C.T. or Y) 21. AUTHORITY AND PCS CODE  PCS ID: AFI 36-2110, PCS ID <b>C</b> AAN: <b>0680NB2384</b>	
22. TDY EXPENSE CHARGEABLE TO		23. Excess Baggage Authorized  PIECES LBS	
Pursuant to AFR 32-6001, you will report to the base housing referral office servicing your new duty station before entering into any rental, lease, or purchase agreement for off-base housing.			
24. REMARKS (Submit travel voucher within 5 workdays after completion of travel. If TDY en route is authorized, attach receipts showing cost of all lodgings used. All promotional items incurred with PCS/TDY must be turned in to AFO upon arrival at gaining base.)			
25. DATE <b>6 MAR 98</b>	26. MPF OFFICIAL (Typed Name, and Grade) <b>JAMES L. TEETER, TSGT, USAF NCOIC RELOCATION ELEMENT</b>	27. SIGNATURE OF MPF OFFICIAL 	
28. DESIGNATION AND LOCATION OF HEADQUARTERS DEPARTMENT OF THE AIR FORCE <b>436 MISSION SUPPORT SQ (AMC) DOVER AFB DE 19902-6520</b>		29. SPECIAL ORDER NO. <b>AB-289</b>	30. DATE <b>6 MAR 98</b>
32. DISTRIBUTION  <b>B</b>		31. TON FOR THE COMMANDER	
34. ADDRESS OF GAINING MPF <b>55 MSS OFFUTT AFB NE 68113</b>		33. SIGNATURE ELEMENT OF ORDERS AUTHENTICATING OFFICIAL   <b>PAUL A. CHAPMAN, USAF MPF, COMMISSIONER</b>	

AF FORM 899, MAY 95 (PC-III Computer Generated)

PREVIOUS EDITION IS OBSOLETE

PLEASE MAKE SURE YOU FILL THIS SHEET OUT

MAIL THIS FORM WITH YOUR TRAINING REPORT INPUTS IN A  
SEPARATE ENVELOPE FROM YOUR SURVEY RESPONSES

Daniel T. Pawlak

NAME

PART V - OTHER QUESTIONS

1. What will your rank be on your completion date? 1 Lt

2. What is the address of your follow-on PCS assignment following your AFIT tour? Do not list TDY en route.

<u>806 MMK</u>	<u>HQAFWA/DNXXM</u>
<u>Bellevue AFB 68005</u>	<u>Offutt AFB NE 68113</u>

3. Who is your AFIT Program Manager? (If more than one, list all)

Capt. Ulman

I grant The Pennsylvania State University the nonexclusive right to use this work for the University's own purposes and to make single copies of the work available to the public on a not-for-profit basis if copies are not otherwise available.

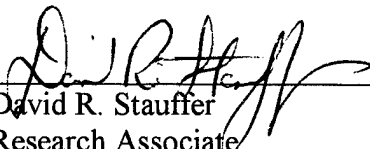
A handwritten signature in black ink, appearing to read 'D. T. Pawlak', written in a cursive style.

---

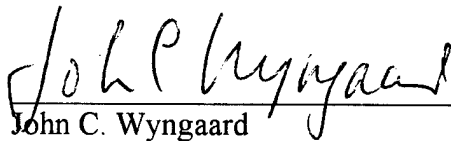
Daniel T. Pawlak

We approve the thesis of Daniel T. Pawlak.

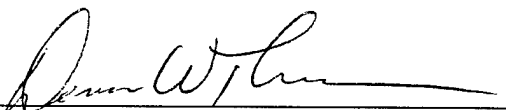
Date of Signature

  
David R. Stauffer  
Research Associate  
Thesis Advisor

23 April 1998

  
John C. Wyngaard  
Professor of Meteorology

23 April 1998

  
Dennis W. Thomson  
Professor of Meteorology  
Head of the Department of Meteorology

23.4.98



## TABLE OF CONTENTS

LIST OF FIGURES.....	vi
LIST OF TABLES .....	x
ACKNOWLEDGMENTS .....	xi
Chapter 1 INTRODUCTION .....	1
1.1 Statement of the Problem.....	1
1.1.1 Modeling the Planetary Boundary Layer .....	1
1.1.2 Modeling the Marine Boundary Layer vs. Land Boundary Layer.....	3
1.2 Motivation and Objectives.....	4
Chapter 2 MODEL DESCRIPTION.....	7
2.1 Non-PBL Model Physics .....	7
2.2 Planetary Boundary-Layer Parameterizations.....	9
2.2.1 Blackadar High-Resolution PBL .....	9
2.2.2 Gayno-Seaman PBL.....	14
2.2.3 Otte-Wyngaard Spectral PBL .....	16
2.3 Spectral PBL - MM5 Coupling Methodology .....	20
Chapter 3 EXPERIMENTAL DESIGN.....	23
3.1 Idealized Case .....	23
3.2 ARM-CART Case .....	30
Chapter 4 ARM-CART CASE DESCRIPTION .....	33
Chapter 5 EXPERIMENTAL RESULTS .....	36
5.1 Idealized Case .....	36
5.2 ARM-CART Case.....	58
Chapter 6 SUMMARY AND CONCLUSIONS .....	95
6.1 Summary.....	95
6.2 Future Work.....	98
REFERENCES.....	100

## LIST OF FIGURES

Figure 2.1.	Model vertical structure including surface energy budget model.....	10
Figure 3.1.	Idealized-case coastal-zone domain, sea surface temperature field (°C) and terrain height (m). Terrain heights (contour interval of 1 m) denote coastline with sea-surface temperatures (contour interval of 1 °C) to the west. Line segment O-L defines a southwest-northeast cross section used to display results in Chapter 5. Points "Ocean" and "Land" indicate the location of atmospheric soundings in Chapter 5.....	26
Figure 3.2.	Temperature and moisture profiles from San Nicolas Island, 0000 UTC (1700 LDT) 30 August 1993, used for single-sounding initialization of MM5. ....	29
Figure 3.3.	ARM-CART case domain and terrain field (m). Contour interval of terrain is 200m. The locations of the ARM-CART central facility (CF) and four boundary facilities (B1, B4, B5, and B6) are also labeled. ....	31
Figure 4.1.	Analysis of 500-mb geopotential height and temperature valid (a) 0000 UTC, 12 April 1997, (b) 0000 UTC, 13 April 1997, and (c) 0000 UTC, 14 April 1997.....	34
Figure 4.2.	Surface analysis valid (a) 0000 UTC, 12 April 1997, (b) 0000 UTC, 13 April 1997, and (c) 0000 UTC, 14 April 1997.....	35
Figure 5.1.	Model-predicted PBL depth (contour interval of 50 m), at 12 h (1200 UTC) for (a) I55-SPB, (b) I55-SPV, (c) I55-BL and (d) I55-GS.....	38
Figure 5.2.	Vertical cross-section of potential temperature (contour interval of 1 K) at 12 h (1200 UTC) along line segment O-L (Fig. 3.1), for (a) I55-SPB, (b) I55-SPV, (c) I55-BL, and (d) I55-GS.....	39
Figure 5.3.	Vertical cross-section of cloud water (contour interval of 0.1 g kg <sup>-1</sup> ) at 12 h (1200 UTC) along line segment O-L (Fig. 3.1), for (a) I55-SPB, (b) I55-SPV, (c) I55-BL, and (d) I55-GS.....	40
Figure 5.4.	Temperature, moisture, and wind profiles for point "Ocean" (Fig. 3.1) at 12 h (1200 UTC) for (a) I55-SPB, (b) I55-SPV, (c) I55-BL, and (d) I55-GS. ....	42

Figure 5.5.	Temperature, moisture, and wind profiles for point "Land" (Fig. 3.1) at 12 h (1200 UTC) for (a) I55-SPB, (b) I55-SPV, (c) I55-BL, and (d) I55-GS. ....	43
Figure 5.6.	Model-predicted PBL depth (contour interval of 50 m), at 24 h (0000 UTC) for (a) I55-SPB, (b) I55-SPV, (c) I55-BL and (d) I55-GS.....	44
Figure 5.7.	Wind speed (contour interval of $0.5 \text{ m s}^{-1}$ ) with wind vectors, at 24 h (0000 UTC) for (a) I55-SPB, (b) I55-SPV, (c) I55-BL and (d) I55-GS. ....	46
Figure 5.8.	Vertical cross-section of potential temperature (contour interval of 1 K) at 24 h (0000 UTC) along line segment O-L (Fig. 3.1), for (a) I55-SPB, (b) I55-SPV, (c) I55-BL, and (d) I55-GS. ....	47
Figure 5.9.	Vertical cross-section of cloud water (contour interval of $0.1 \text{ g kg}^{-1}$ ) at 24 h (0000 UTC) along line segment O-L (Fig. 3.1), for (a) I55-SPB, (b) I55-SPV, (c) I55-BL, and (d) I55-GS. ....	48
Figure 5.10.	Temperature, moisture, and wind profiles for point "Ocean" (Fig. 3.1) at 24 h (0000 UTC) for (a) I55-SPB, (b) I55-SPV, (c) I55-BL, and (d) I55-GS. ....	50
Figure 5.11.	Temperature, moisture, and wind profiles for point "Land" (Fig. 3.1) at 24 h (0000 UTC) for (a) I55-SPB, (b) I55-SPV, (c) I55-BL, and (d) I55-GS. ....	52
Figure 5.12.	Vertical cross-section of potential temperature (contour interval of 1 K) at 24 h (0000 UTC) along line segment O-L (Fig. 3.1), for (a) I32-SPB, (b) I32-SPV, (c) I32-BL, and (d) I32-GS. ....	54
Figure 5.13.	Vertical cross-section of cloud water (contour interval of $0.1 \text{ g kg}^{-1}$ ) at 24 h (0000 UTC) along line segment O-L (Fig. 3.1), for (a) I32-SPB, (b) I32-SPV, (c) I32-BL, and (d) I32-GS. ....	55
Figure 5.14.	Temperature, moisture, and wind profiles for point "Land" (Fig. 3.1) at 24 h (0000 UTC) for (a) I32-SPB, (b) I32-SPV, (c) I32-BL, and (d) I32-GS. ....	57
Figure 5.15.	Normalized total MM5 computation time for idealized-case experiments.....	59

Figure 5.16.	Model-predicted PBL depth at 4 h (0400 UTC 12 April 1997) with contour interval of 200 m, and wind vectors ( $\text{m s}^{-1}$ ) for Exps. (a) SPB, (b) SPV, (c) BL, and (d) GS. ....	62
Figure 5.17.	Time-series analysis valid 0000 UTC 12 April 1997 to 0000 UTC 14 April 1997 comparing hourly observed and model-predicted surface pressure at CF. ....	65
Figure 5.18.	Time-series analysis, valid 0000 UTC 12 April 1997 to 0000 UTC 14 April 1997, comparing hourly observed total column liquid water measured by microwave radiometer, and model-predicted integrated cloud water for the CF. The bottom of the figure shows hourly observed sky condition at Ponca City, OK, 25 miles northeast of the CF. ....	66
Figure 5.19.	Time-series analysis, valid 0000 UTC 12 April 1997 to 0000 UTC 14 April 1997, comparing the five-facility average three-hourly observed and hourly model-predicted surface layer (30 m) wind speed. ....	68
Figure 5.20.	Time series analysis, valid 0000 UTC 12 April 1997 to 0000 UTC 14 April 1997, comparing the five-facility average three-hourly observed and hourly model-predicted surface layer (30 m) temperature. ....	70
Figure 5.21.	Time-series analysis, valid 0000 UTC 12 April 1997 to 0000 UTC 14 April 1997, comparing the five-facility average three-hourly observed and hourly model-predicted temperature at (a) 900 mb, (b) 800 mb, and (c) 700 mb. ....	71
Figure 5.22.	Time-series analysis, valid 0000 UTC 12 April 1997 to 0000 UTC 14 April 1997 of diagnosed PBL depth at the CF. ....	74
Figure 5.23.	Time-series analysis, valid 0000 UTC 12 April 1997 to 0000 UTC 14 April 1997, comparing the five-facility average three-hourly observed and hourly model-predicted PBL depth. ....	75
Figure 5.24.	Time-series analysis, valid 0000 UTC 12 April 1997 to 0000 UTC 14 April 1997, comparing the three-hourly observed and hourly model-predicted PBL depth at facility (a) B1, (b) B5, and (c) CF. ....	77
Figure 5.25.	Time-series analysis, valid 0000 UTC 12 April 1997 to 0000 UTC 14 April 1997, comparing the three-hourly observed and hourly model-predicted surface-layer (30 m) temperature at facility (a) B1, (b) B5, and (c) CF. ....	78

Figure 5.26.	Temperature, moisture, and wind profiles valid at 8 h (0800 UTC, 12 April 1997) at facility B1 for (a) observation (b) SPB, (c) SPV, (d) BL, and (e) GS.....	80
Figure 5.27.	Temperature, moisture, and wind profiles valid at 11 h (1100 UTC, 12 April 1997) at facility B5 for (a) observation (b) SPB, (c) SPV, (d) BL, and (e) GS.....	81
Figure 5.28.	Temperature, moisture, and wind profiles valid at 44 h (2000 UTC, 13 April 1997) at facility B1 for (a) observation (b) SPB, (c) SPV, (d) BL, and (e) GS.....	83
Figure 5.29.	Time-series analysis, valid 0000 UTC 12 April 1997 to 0000 UTC 14 April 1997 comparing hourly observed and model-predicted (a) net radiation, (b) sensible heat flux, and (c) latent heat flux at the CF. ....	85
Figure 5.30.	Time-series analysis, valid 0000 UTC 12 April 1997 to 0000 UTC 14 April 1997 comparing the relative contribution of the spectral model PBL tendency terms of Eq. 2.36 to the total PBL tendency for Exp. SPB at CF. Tendencies are plotted at 15-minute intervals.....	88
Figure 5.31.	Time-series analysis, valid 0004 UTC 12 April 1997 to 0046 UTC 12 April 1997 showing PBL depth during deep convection (diagnosis mode) over southwest Louisiana for Exp. SPB. PBL depths are plotted every time-step (36 s).....	90
Figure 5.32.	Normalized total MM5 computation time for ARM-CART case experiments.....	94

**LIST OF TABLES**

Table 3.1.	Experimental Design. ....	24
Table 3.2.	Sigma-layer distribution below ~ 700 mb for 55-layer idealized experiments. ....	27
Table 3.3.	Sigma-layer distribution below ~ 700 mb for 32-layer idealized and ARM-CART experiments. ....	28
Table 5.1.	ARM-CART case experimental error statistics. ....	69
Table 5.2.	ARM-CART case ordinal ranking of experiments. ....	91

## ACKNOWLEDGMENTS

I thank Dr. David Stauffer for setting a standard of excellence that I will struggle to meet for the rest of my career. I thank Professor John Wyngaard for his practical perspective, and for shifting my focus towards the things that really matter. Martin Otte's help within the spectral code was invaluable. I learned a great deal about debugging complex programs such as the MM5 by observing his technique. I wish to thank Dr. Eugene Clothiaux for his assistance with the retrieval and processing of ARM-CART data. I'm grateful to Dr. George Young for his suggestion to use the Bulk-Richardson technique for diagnosis of boundary-layer depth during convection, and for his insightful remarks such as "when you're walking a tightrope 20 ft. above the ground, don't worry about what color socks you're wearing." I especially appreciate the help of Glenn Hunter and Annette Lario-Gibbs for their endless patience, and for their assistance with the many problems I came across in my work. I thank the Air Force Institute of Technology for allowing me to work with the distinguished mesoscale model development team at Penn State, and the Navy for providing support for this research through the Office of Naval Research Grant N00014-92-1688 and U.S. Navy Contract N00039-92-C-0100. I thank my wife Debbie for reminding me that I, with God's help, am strong enough to weather any storm no matter how severe, and I thank my family for their unwavering support throughout this endeavor.

## Chapter 1 INTRODUCTION

### 1.1 Statement of the Problem

#### 1.1.1 Modeling the Planetary Boundary Layer

The Planetary Boundary Layer (PBL) is the atmospheric layer containing turbulence caused by interactions between the atmosphere and the surface of the earth through viscous and radiative processes. It can be the most critical part of the atmosphere that a mesoscale numerical model must represent to determine the general behavior of the atmosphere as a whole. However, because the turbulent processes that shape the PBL are "sub-gridscale", a parameterization must be used to represent the effect of turbulence on the grid-resolved meteorological fields.

One of the simplest ways to parameterize the PBL is to use a mixed-layer model, which assumes the profiles of mean variables (i.e., wind, temperature, and moisture) are constant with height in the boundary layer. The equations are then integrated over the depth of the PBL, which eliminates the vertical coordinate. This method is very fast computationally, but processes such as baroclinicity, differential advection, changing stability regimes, and entrainment cause deviations from these well-mixed profiles. For example, the physics associated with a cloud-topped marine boundary layer can result in a "decoupling" of the PBL, where two mixed layers separated in the vertical by a stable layer (Nicholls 1984) can lead to thinning of the stratocumulus layer by shunting of the surface moisture source. Thus mixed-layer models have limited applicability.

Other integral models which have been developed assume "unmixed" shapes including linear profiles (Zeman 1979) and non-dimensional vertical gradient functions



based on large eddy simulation (LES) (Wyngaard and Brost 1984). However, these profiles are not generally representative of all conditions. They are instead prescribed for a specific stability regime and the profiles maintain their shape throughout the model run.

Another option is to solve the boundary-layer equations on a relatively high-resolution vertical grid using finite difference techniques. The Blackadar high-resolution (multi-layer) PBL model (Blackadar 1976, 1979, Zhang and Anthes 1982, Grell et al. 1994) used in The Pennsylvania State University/National Center for Atmospheric Research (PSU/NCAR) Mesoscale Model version five (MM5) (Dudhia 1993, Grell et al. 1994), includes a first-order eddy diffusivity closure and a non-local exchange parameterization. The Gayno-Seaman PBL model (Gayno 1994), also used in the PSU/NCAR MM5, uses a 1.5-order closure that carries a prognostic equation for turbulent kinetic energy. Other high-resolution PBL models include full second-order closure models (Mellor and Yamada 1974) that carry prognostic equations for the second-order moments (i.e., Reynolds stresses), and the transilient turbulence model (Stull 1984). These high-resolution PBL models allow the vertical profiles to vary in time, thus producing more realistic structure than the mixed-layer model. However, these PBL models are much more computationally demanding, requiring 25 percent or more of the total mesoscale model computation time (Stauffer et al. 1997).

Otte and Wyngaard (1996) have designed an "Unmixed Layer" model with spatially and temporally varying PBL structure, similar to that achieved by high-resolution PBL models, while remaining nearly as computationally simple and efficient as the mixed-layer model. This model represents vertical profiles of the spatially averaged mean

model variables with a truncated series of shifted Legendre polynomials, where the zeroth Legendre mode, the PBL layer average, is identically a mixed-layer model. Additional terms in the Legendre series add structure to the vertical profiles. This thesis will introduce the design strategy for implementation of this spectral PBL model in the MM5, and evaluate its performance using both idealized and real-data MM5 simulations.

Although the selection of a closure is necessary for the operation of the spectral PBL model and inevitably affects the model results, the primary focus of this work must be evaluation of the spectral boundary-layer architecture rather than the specific closure.

#### 1.1.2 Modeling the Marine Boundary Layer vs. Land Boundary Layer

It is important that a PBL model also be general enough to accurately simulate the boundary layer in both marine and land environments because the physical processes that determine the boundary-layer structure and evolution over water and land may be quite different. For example, over land it is often the surface heat or buoyancy flux that determines the stability of the PBL, while the surface fluxes over water vary far less on a diurnal timescale. In a marine environment where the surface water temperature is cool, the stability of the boundary layer may be determined largely by cooling of cloud-topped layers by radiation and evaporation. Thus the role of non-PBL physics can also be very important.

Another major consideration governing the ability of a model to represent the PBL is the availability of data for use in initial conditions. Over land there are generally more observations of many types with higher spatial and temporal resolution than those over

water. Regardless of the PBL model chosen to represent the structure of the boundary layer, poor initial conditions can seriously degrade the quality of the PBL forecasts in coastal zones (Leidner 1995). Because there are fewer direct observations of atmospheric properties over the ocean, mesoscale models rely heavily on global models to provide their initial conditions in a marine environment. Since global models have much coarser vertical resolution than mesoscale models, and again because of sparse observations, the marine boundary layer (MBL) is generally not represented very well in model initial conditions. It is crucial that the MBL be represented accurately because of its impact on the general state of the atmosphere, especially in coastal zones.

MBL clouds may significantly affect the earth's radiative balance, reducing the amount of solar radiation that reaches the surface of the earth, and redistributing longwave radiation in the lower troposphere. Leidner and Stauffer (1996) developed and tested a method of dynamically initializing the MBL that combines current observations and climatological data during the 12 hours prior to the model forecast period. They found that this method significantly improved the accuracy of PBL depth and inversion strength in the initial conditions and subsequent forecasts over static initialization in the California coastal zone. Therefore, it is important that the spectral PBL be evaluated in both land and marine environments, with special attention given to initialization of the PBL in the data-sparse offshore regions.

## 1.2 Motivation and Objectives

One example of an application that requires accurate representation of the three-dimensional structure and evolution of boundary-layer properties is forecasting the

propagation of electromagnetic waves through the atmosphere. Meteorological fields which vary both spatially and temporally modify the atmosphere's refractive index field, and this in turn changes the path and intensity of electromagnetic (EM) waves propagating through the atmosphere. Atmospheric refraction affects military, civilian, and scientific systems that rely on the transmission and reception of EM energy. Environmental profiles that determine the structure of the refractive index field include vapor pressure, temperature, and atmospheric pressure. The EM propagation models are used to predict the behavior of radio waves and microwaves as they move through the atmosphere. Because of the spatial and temporal variability of these fields, however, it is critical to the determination of EM wave propagation that a PBL model accurately represents the vertical profiles and evolution of these variables. Williams et al. (1997) showed that the MM5 with appropriate model physics and sufficient vertical resolution can accurately represent the three-dimensional refractive index off the coast of California.

This thesis will first perform a "reality check" and test the spectral PBL in an idealized coastal-zone environment where the spectral model results will be compared to the model output of the Blackadar high-resolution PBL model and the Gayno-Seaman PBL model. A second test will evaluate the three PBL models using real data over the southern Great Plains Atmospheric Radiation Measurement (ARM) Cloud and Radiation Testbed (CART) site.

Thus, the specific objectives of this thesis are:

- Determine how to best link a vertical spectral PBL scheme and a three-dimensional grid-point mesoscale model and ensure proper interaction between the PBL model and non-PBL physics and dynamics modules.
- Benchmark the spectral model's performance (accuracy and efficiency) against that of the Blackadar high resolution PBL model and the Gayno-Seaman PBL model in an idealized coastal-zone environment and examine the impact of gridspace vertical resolution on the PBL model solutions.
- Determine how accurately and efficiently the three PBL models predict the general features and evolution of the PBL using a real-data case and the special ARM-CART data.

Chapter 2 is an overview of the numerical weather prediction model and the three PBL models used in the course of this evaluation. Chapter 3 outlines the details for each of the model tests described above, as well as the observational data that are used for quantitative analysis of the model's performance. Chapter 4 will discuss the meteorological conditions present during the real-data case. The results of the evaluations will be presented in Chapter 5, and Chapter 6 will summarize the work presented here and will suggest topics for future research.

## Chapter 2 MODEL DESCRIPTION

This study uses the fifth generation Pennsylvania State University/National Center for Atmospheric Research (PSU/NCAR) Mesoscale Model version 2 (MM5) for all simulations. The MM5 (Dudhia 1993, Grell et al. 1994) is based on the nonhydrostatic, fully compressible equations of motion in a rotating reference frame. It uses a terrain-following non-dimensionalized pressure vertical coordinate, sigma, defined as

$$\sigma = \frac{p_0 - p_t}{p_s - p_t} \quad (2.1)$$

where  $p_0$  is a constant reference pressure which varies only in the vertical, and  $p_s$  and  $p_t$  are the surface and top pressures of the model reference state. Therefore, the heights of the model sigma levels are determined entirely by the reference-state thermodynamic structure and are independent of time.

The prognostic model variables are pressure perturbation  $p'$ , the three momentum components ( $u$ ,  $v$ ,  $w$ ), the temperature  $T$ , specific humidity  $q_v$ , and cloud- and rainwater variables. The spatial derivatives within MM5 are computed by second-order finite differencing on an Arakawa-Lamb B grid. The temporal differencing consists of leapfrog and forward steps, and a semi-implicit scheme is used for terms involving sound waves.

### 2.1 Non-PBL Model Physics

The atmospheric radiation module (Dudhia 1989) used for these simulations allows both longwave and shortwave radiation to interact with the clear atmosphere, cloud and

precipitation fields, and with the surface. Absorption and emission of longwave radiation by water vapor, and emission of longwave radiation by stratospheric carbon dioxide is parameterized by the broadband emissivity method (Stephens 1984). The shortwave radiation is determined by accounting for the effects of 1) solar zenith angle on path length, 2) scattering and absorption by clouds, 3) scattering by clear air, and 4) absorption by water vapor. Leidner and Stauffer (1996) found that the absorption of shortwave radiation by marine stratus calculated by the Dudhia radiation scheme causes unrealistic excess heating that completely dissipates the marine stratus during daytime. As discussed in Leidner (1995), researchers have found that shortwave heating in stratus clouds is typically one sixth to one third that of the longwave cooling. Slingo (1989) showed that simpler broadband radiation schemes tend to overestimate shortwave absorption by cloud as compared to more realistic schemes with four or more wavelength bands. Leidner and Stauffer (1996) conducted sensitivity tests that limited the shortwave heating within clouds to one third of the longwave cooling and found that MBL clouds behaved more realistically. Therefore, absorption of shortwave radiation in cloud layers is limited to one third of that of the longwave tendency in these simulations.

In this study the MM5 calculates moisture processes using both explicit (Dudhia 1989) and parameterized (Kain and Fritsch 1993) precipitation modules. The explicit, or grid-resolved, moisture scheme computes tendencies for water vapor mixing ratio, cloud water, and rain water, taking into account condensation of water vapor into cloud at water saturation, accretion of cloud by rain, conversion of cloud to rain, and evaporation of

rain. The subgrid-scale convective parameterization accounts for deep precipitating convection and includes the effects of moist downdrafts.

Ground temperature is computed via a force-restore method where the surface energy budget consists of a substrate (a deep soil layer) with invariant temperature, beneath a slab that represents a thin layer of soil. This module uses an energy budget to compute the ground potential temperature  $\theta_g$ ,

$$C_g \frac{\partial \theta_g}{\partial t} = R_n - H_m - H_g - E_g \quad (2.2)$$

where  $C_g$  is the thermal capacity of the slab per unit area,  $R_n$  is the net radiative heat flux,  $H_m$  is the heat flow into the substrate,  $H_g$  is the heat flux into the atmosphere, and  $E_g$  is the latent heat flux (Fig. 2.1). All of the prognostic variables except the vertical motion  $w$  are defined at the "half layers"; vertical motion and all of the diagnostic quantities such as Richardson number, eddy diffusivity, and turbulent fluxes are defined at the "full layers" (see Fig. 2.1). The subscript "a" is used to represent the lowest model half layer which represents the surface layer, the subscript "g" refers to the ground, and the subscript "i" refers to the  $i^{\text{th}}$  model layer.

## 2.2 Planetary Boundary-Layer Parameterizations

### 2.2.1 Blackadar High-Resolution PBL

The Blackadar high resolution PBL model (Blackadar 1976, 1979, Zhang and Anthes 1982, Grell et al. 1994), forecasts vertical mixing of heat, moisture, and momentum for four different stability regimes: nocturnal, damped mechanical turbulence, forced



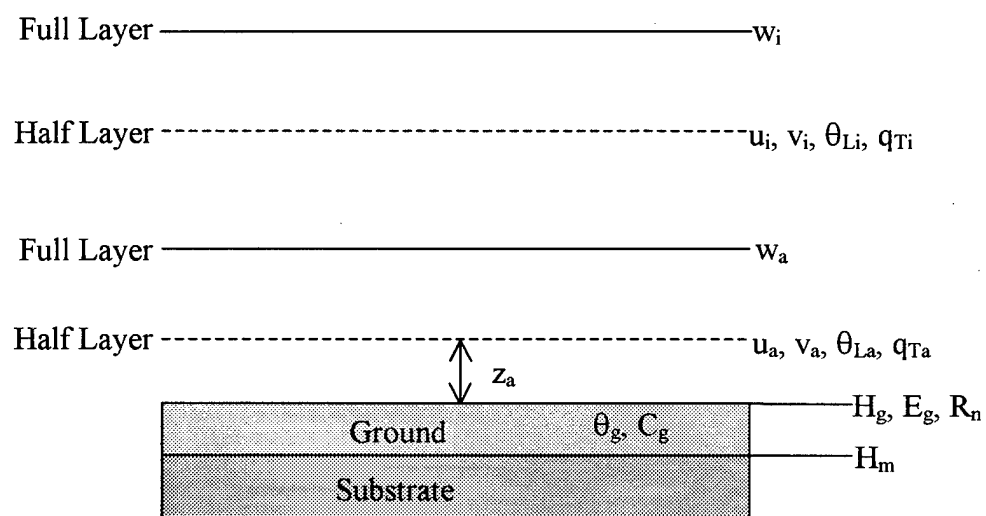


Figure 2.1. Model vertical structure including surface energy budget model.

convection, and free convection. A first-order (K-theory) approach is used for all regimes except free convection, which uses a non-local closure.

To close the model, the turbulent fluxes must be parameterized at the surface, throughout the depth of the PBL, and the top of the PBL (entrainment fluxes). The ground stress,  $\tau_g$ , can be calculated using drag laws derived from Monin-Obukhov (M-O) similarity as

$$\tau_g = \rho u_*^2, \quad (2.3)$$

where  $\rho$  is density and  $u_*$ , the friction velocity, is given by

$$u_* = \text{MAX} \left( \frac{k V_a}{\ln \left( \frac{z_a}{z_0} \right) - \psi_m}, u_{*0} \right), \quad (2.4)$$

where  $k$  is Von Karman's constant,  $V_a$  is the scalar wind speed in the lowest model layer,  $z_a$  is the height of the lowest model layer,  $z_0$  is roughness length,  $\psi_m$  is a non-dimensional stability parameter that is a function of the bulk Richardson number, and  $u_{*0}$  is a background value of  $0.1 \text{ m s}^{-1}$ . The fluxes of sensible and latent heat are also calculated using similarity (Grell et al. 1994).

The flux calculations are dependent on the stability regime. Regime classification depends on the sign and magnitude of the bulk Richardson number

$$Rb = \frac{g z_a (\theta_{va} - \theta_{vg})}{\theta_a (V_a)^2}. \quad (2.5)$$

Again, the subscripts "a" and "g" refer to the lowest computational model layer and the ground, respectively, the subscript "v" indicates virtual, as in virtual potential temperature,  $g$  is acceleration due to gravity, and  $V$  is the wind speed.

In regime one (nocturnal),  $Rb \geq 0.2$  represents a surface layer so stable that no turbulence can exist. The PBL depth is zero and

$$\psi_h = \psi_m = -2 \ln \frac{z_a}{z_0}, \text{ and} \quad (2.6)$$

$$u_* = u_{*0}. \quad (2.7)$$

The second regime is damped mechanical turbulence where  $0.2 > Rb > 0$ . Here the scaling parameters are,

$$\frac{z_a}{L} = \frac{Rb}{1.1 - 5Rb} \ln \frac{z_a}{z_0} \quad (2.8)$$

where  $L$  is the Monin-Obukhov length, and

$$\psi_h = \psi_m = -5z_a / L. \quad (2.9)$$

Again the PBL depth is zero.

The third regime represents a marginally unstable condition, forced convection, with  $Rb \leq 0$  and  $|h/L| \leq 1.5$ , where  $h$  is the diagnosed PBL depth,

$$z_a / L = Rb \ln \frac{z_a}{z_0}, \text{ and} \quad (2.10)$$

$$\psi_h = \psi_m = 0. \quad (2.11)$$

In these K-theory regimes, the eddy diffusivities for momentum, heat and moisture,  $K_m=K_h=K_q$ , are determined by the Richardson number,

$$K_m = K_0 + S_i (kl)^2 (Ri_c - Ri) / Ri_c, \quad (2.12)$$

where  $K_0$  is a background value,  $Ri_c$  is the critical Richardson number,  $l$  is the length scale of the energy containing eddies,  $S_i$  is the vertical wind shear, and  $Ri$  is the Richardson number,

$$Ri = \frac{\frac{g}{\theta_a} \frac{\partial \theta}{\partial z}}{S_i^2}. \quad (2.13)$$

In the "free convection" regime four, vertical mixing is not determined by local gradients, but by the thermal structure of the entire mixed layer and the surface heat flux. In this regime,  $Rb < 0$  and  $|h/L| > 1.5$ , and "non-local" mixing takes place between the lowest layer and every other layer in the mixed layer. In this regime the PBL depth,  $h$ , is calculated by determining the level at which negative buoyancy area equals 20 percent of the positive buoyancy area in underlying layers. The stability parameters are approximated by the polynomials,

$$\psi_m = 0.0954 - 1.86 \left( \frac{z_a}{L} \right) - 1.07 \left( \frac{z_a}{L} \right)^2 - 0.249 \left( \frac{z_a}{L} \right)^3, \text{ and} \quad (2.14)$$

$$\psi_h = 0.201 - 3.23 \left( \frac{z_a}{L} \right) - 1.99 \left( \frac{z_a}{L} \right)^2 - 0.474 \left( \frac{z_a}{L} \right)^3. \quad (2.15)$$

The prognostic equations for convective mixing are

$$\frac{\partial \theta_i}{\partial t} = \bar{m}(\theta_a - \theta_i), \quad (2.16)$$

$$\frac{\partial q_i}{\partial t} = \bar{m}(q_a - q_i), \quad (2.17)$$

$$\frac{\partial u_i}{\partial t} = \bar{m}(u_a - u_i), \text{ and} \quad (2.18)$$

$$\frac{\partial v_i}{\partial t} = \bar{m}(v_a - v_i), \quad (2.19)$$

where  $q_i$  is vapor or cloud water mixing ratio,  $\bar{m}$  is the mass fraction per unit time exchanged between the surface layer and the  $i^{th}$  layer of the PBL.

### 2.2.2 Gayno-Seaman PBL

The Gayno-Seaman PBL model (Gayno, 1994, Gayno et al. 1994) includes a prognostic equation for the turbulent kinetic energy (TKE) but uses the same regimes as the Blackadar model to determine stability parameters. This model diagnoses the height of the PBL from the TKE profiles. If the maximum TKE in the profile is less than  $0.1 \text{ m}^2 \text{ s}^{-2}$ , the PBL depth is set to zero and the Blackadar scheme is used. Otherwise, the scheme determines the top of the PBL to be the first level at which the TKE decreases to  $0.1 \text{ m}^2 \text{ s}^{-2}$ . In order to incorporate cloud water into the turbulent mixing code, this model substitutes liquid potential temperature,  $\theta_L$ , for potential temperature and total water mixing ratio,  $q_T$ , for water vapor and cloud water mixing ratios  $q$  and  $q_L$ , where

$$\theta_L = \theta - \frac{\theta}{T} \frac{L}{C_p} q_L, \text{ and} \quad (2.20)$$

$$q_T = q + q_L, \quad (2.21)$$

where  $L$  is the latent heat of vaporization,  $C_p$  is the specific heat of moist air at constant pressure,  $\theta/T$  is the ratio of potential to absolute temperature or the Exner pressure function. These variables are approximately conserved during phase changes (Betts, 1973).

The ground fluxes are calculated as in the Blackadar model using M-O similarity theory. The fluxes within the PBL and entrainment fluxes are calculated using a K-theory closure,

$$\overline{w'\theta'_L} = -K_h \left[ \frac{\partial \theta_L}{\partial z} - \gamma_g \right], \quad (2.22)$$

$$\overline{w'q'_T} = -K_h \frac{\partial q_T}{\partial z}, \text{ and} \quad (2.23)$$

$$\overline{w'\tilde{v}'_H} = -K_m \frac{\partial \tilde{v}_H}{\partial z}, \quad (2.24)$$

where a counter-gradient heat flux term  $\gamma_g$  is used to modify the vertical gradient of  $\theta_L$  in convective conditions. However, the eddy diffusivities are functions of the TKE and mixing length scales ( $l_h$ ,  $l_m$ ):

$$K_h = l_h (TKE)^{1/2}, \quad (2.25)$$

$$K_m = l_m (TKE)^{1/2}. \quad (2.26)$$

The length scales are functions of a characteristic length scale of the energy-containing eddies, buoyancy, shear, and TKE.

The grid-resolved TKE is given by the prognostic equation

$$\frac{d(TKE)}{dt} = -\overline{w'\tilde{v}_H'} \frac{\partial \tilde{v}_H}{\partial z} + \frac{g}{\theta_v} \overline{w'\theta_v'} - \frac{\partial}{\partial z} (\overline{w'(TKE)'}) - \frac{(TKE)}{\tau_0} \quad (2.27)$$

where  $\theta_v'$  is the perturbation virtual potential temperature and  $\tau_0$  is a dissipation time scale. The first term on the right side of Eq. 2.27 is mechanical shear production of TKE, the second is buoyant production/destruction of TKE, the third is turbulent transport of TKE, and the last term is viscous dissipation of TKE. This model ignores horizontal advection and the pressure flux divergence term.

### 2.2.3 Otte-Wyngaard Spectral PBL

In the Otte-Wyngaard PBL (Otte and Wyngaard 1996), the vertical profiles of model variables have structure similar to the high-resolution models. The model variables  $u$ ,  $v$ ,  $\theta_L$  and  $q_T$  are decomposed into five shifted Legendre modes (orthogonal polynomials), and thus there is no direct dependence of the model variables on the vertical coordinate. Prognostic equations for the spectral coefficients are integrated forward in time. This model also requires parameterization of surface and entrainment fluxes, in addition to parameterization of the fluxes within the PBL as in the high-resolution models, since these must be integrated over the depth of the PBL.

The surface fluxes are computed as in the Blackadar model, using drag laws derived from M-O similarity theory. The fluxes within the PBL are parameterized with an eddy diffusivity closure as in the Blackadar and Gayno-Seaman models,

$$\overline{u'w'} = -\frac{K_m}{h} \frac{\partial u}{\partial \eta} \quad (2.28)$$

$$\overline{v'w'} = -\frac{K_m}{h} \frac{\partial v}{\partial \eta} \quad (2.29)$$

$$\overline{\theta_L'w'} = -\frac{K_h}{h} \frac{\partial \theta_L}{\partial \eta}, \text{ and} \quad (2.30)$$

$$\overline{q_T'w'} = -\frac{K_h}{h} \frac{\partial q_T}{\partial \eta}, \text{ where} \quad (2.31)$$

$$\eta \approx \frac{z}{h(t)} \quad (2.32)$$

is the normalized vertical coordinate in the PBL and  $h$  is the PBL height. The eddy diffusivities are given by

$$K_m = kw_m h \eta (1 - \eta)^2, \text{ and} \quad (2.33)$$

$$K_h = kw_h h \eta (1 - \eta)^2. \quad (2.34)$$

The velocity scales  $w_m$  and  $w_h$  are derived through M-O similarity, and vary based on the stability. The PBL height is computed via a prognostic equation. Equations 2.30, 2.31, and 2.34 are used only in the stable regime. When the buoyancy flux is non-negative, the



non-local closure of Fiedler and Moeng (1985), similar to the transilient approach of Stull (1984), is used for turbulent mass fluxes.

The entrainment fluxes are computed through the jump formula derived by Lilly (1968),

$$\overline{w'\theta_{L1}'} = -\left[\frac{dh}{dt} - w_1\right]\Delta\theta_L \equiv -w_e\Delta\theta_L, \quad (2.35)$$

where  $\theta_{L1}'$  is perturbation liquid potential temperature at the top of the boundary layer and  $w_1$  and  $\Delta\theta_L$ , the mean vertical velocity at the top of the PBL and the jump of the mean liquid potential temperature across the capping inversion, respectively, are given as boundary conditions by the external model. The entrainment velocity,  $w_e$ , is defined as the difference between the material derivative of  $h$ ,  $dh/dt$ , and the mean vertical velocity at the top of the boundary layer,  $w_1$ . This leaves as the final unknown, the height tendency of the top of the PBL

$$\frac{dh}{dt} = \frac{\partial h}{\partial t} + A_h = D_h + w_1 + w_e, \quad (2.36)$$

where  $\partial h/\partial t$  is the local derivative,  $A_h$  is horizontal advection, and  $D_h$  is horizontal diffusion. This model differs from the Blackadar and Gayno-Seaman models in that it has a prognostic equation for the PBL height, which is determined in two ways, based on the stability regime. In the nocturnal regime,

$$\frac{dh}{dt} = \frac{\partial h}{\partial t} + A_h = \frac{(h_e - h)}{\tau} + D_h, \text{ where} \quad (2.37)$$

$$\tau = -\frac{3}{4} \left[ \frac{\theta_1 - \theta_g}{\frac{d\theta_g}{dt}} \right], \text{ and} \quad (2.38)$$

$$h_e = \frac{2b^2 u_*}{a|f|} \left[ 1 + \left( 1 + \frac{4b^2 u_*}{\alpha^2 L|f|} \right)^{1/2} \right]^{-1}. \quad (2.39)$$

Here,  $\alpha=0.53$  and  $b=0.4$  (Otte and Wyngaard 1996), and following Nieuwstadt and Tennekes (1981)  $\tau$  is the timescale over which the nocturnal inversion relaxes towards the equilibrium height  $h_e$ .

In the neutral and convective boundary layers, the buoyancy entrainment flux (Moeng and Sullivan 1994) is based on the surface buoyancy flux, where

$$\overline{\theta_v' w_1'} = -0.2 \overline{\theta_v' w_0'} - 0.42 \frac{u_*^3 \theta_a}{gh} \quad (2.40)$$

is substituted into Lilly's jump model for entrainment fluxes, and given  $\Delta\theta_v$  we can solve for the entrainment velocity  $w_e$  allowing computation of all entrainment fluxes given jumps of the mean fields across the inversion. It has been found that the prognostic equation becomes unreliable during deep convection; thus, in the case of deep convection,

$$\frac{dh}{dt} = \frac{h_d - h}{\tau} \quad (2.41)$$

where  $h_d$  is a diagnosed PBL height, and  $\tau = 100$  s. The method of diagnosis is described later in this section. It must be emphasized that the closure used here is of secondary importance to the spectral architecture itself.

The mean variables  $F$  in this spectral model are represented by a truncated series of shifted Legendre polynomials

$$F(\eta) = \sum_{n=0}^{\infty} \hat{F}_n P_n^*(\eta) \quad (2.42)$$

on the interval  $0 \leq \eta \leq 1$ , where the  $n^{\text{th}}$  polynomial is defined by a variation of Rodriguez's formula

$$P_n^*(\eta) = \frac{(-1)^n}{n!} \frac{d^n [\eta(1-\eta)]^n}{d\eta^n} \quad (2.43)$$

(Abramowitz and Stegun 1970). The first mode ( $n = 0$ ) is the layer average of the function, and is identically a mixed-layer model. Additional modes add structure to the vertical profiles. Otte and Wyngaard (1996) showed that only five modes ( $n = 0, 1, 2, 3, 4$ ) are necessary to produce vertical structure of the mean variables similar to that demonstrated by high-resolution models.

### 2.3 Spectral PBL - MM5 Coupling Methodology

The spectral PBL model had to be integrated into the framework of MM5. The PBL subroutine is called at every advection time step. The surface fluxes are calculated, and the spectral coefficients  $\hat{F}_n$  are computed. The coefficients are then integrated forward in time and the spectral modes resolved by MM5 are converted back to physical space. The

change of the variable between the previous and current time steps is used to calculate a tendency that is added to the other tendency terms (e.g., advection, diffusion, etc.).

The first step towards converting the grid-space fields into spectral space is to interpolate the values of the grid-space vertical profiles to levels represented by the five zeroes of the fifth-degree Legendre polynomial. Shifted Legendre Polynomials have the property that they are orthogonal on the interval  $0 \leq \eta \leq 1$ . This means that all of the zeros of  $P_n(\eta)$  are real and distinct and lie in the open interval  $0 < \eta < 1$  (Stroud 1974). These zeros are constant known values (Burden et al. 1981) that need not be re-calculated during the model run. This method of evaluating the functions at zeros of the  $n^{\text{th}}$  degree orthogonal polynomial is known as Gaussian Quadrature. Using this method significantly improves the accuracy of the conversion from grid-point to spectral space, and clearly increases the efficiency as well.

Use of a prognostic equation for PBL depth requires both initial conditions and lateral boundary conditions. Therefore, the PBL height is diagnosed from model mass or mass and wind fields at the initial time as well as at later times for regions with deep convection and in relaxation lateral boundary conditions.

Preliminary tests indicated sensitivity to initial conditions. Two methods are tested for initial and convective diagnosis of PBL depth. The first method is essentially that used by the Blackadar model in the forced-convection regime. The base of a capping inversion is found to be where the virtual potential temperature exceeds the surface-layer value. The second method (Vogelezang and Holtslag 1996) is based on determining the

level at which the Bulk-Richardson number ( $Rib$ ), evaluated over successively deeper layers, exceeds the critical value, 0.25. The Bulk-Richardson number is given by

$$Rib = \frac{(g / \theta_{vs})(\theta_{vh} - \theta_{vs} - \theta_{vsc})(h - z_s)}{(u_h - u_s)^2 + (v_h - v_s)^2 + 100u_*^2} \quad (2.44)$$

where the subscript "s" refers to the surface or reference-level value of the variable and  $\theta_{vsc}$  is zero for stable and neutral boundary layers, and

$$\theta_{vsc} = 8.5 \frac{\overline{w' \theta'_{v0}}}{w_m}, \quad (2.45)$$

for unstable conditions, where  $w_m$  is a turbulent velocity scale.

In both methods, the initial PBL depth is set to the diagnosed PBL depth. At those grid points experiencing deep convection, the PBL is nudged towards the diagnosed PBL depth with  $\tau = 100$  s. This is the only PBL tendency term used during convection.

In order to complete the prognostic equation for PBL depth in MM5, both advection and diffusion schemes are added. The PBL depth is advected by the wind at the PBL height. Very weak horizontal diffusion of PBL depth is used to eliminate noise due to aliasing from the advection scheme. Both the advection and diffusion PBL tendency terms are ignored during deep convection.

## Chapter 3 EXPERIMENTAL DESIGN

Evaluation of the spectral PBL scheme is conducted using two cases: an idealized coastal-zone case and a real-data case over the ARM-CART site. Experiments using each of the three PBL schemes described in Chapter 2 are conducted for both of these cases. Sensitivity of the model results to vertical resolution is addressed in the idealized-case experiments by using either 55 or 32 vertical model layers. Two versions of the spectral PBL model are investigated: one uses the virtual potential temperature method (see Section 2.3 for the details) for initial and convective diagnosis of PBL height and the other uses the Bulk-Richardson method. A description of the experimental design is outlined in Table 3.1.

### 3.1 Idealized Case

An idealized case is used to test the coupling of the spectral PBL with the MM5 and determine whether or not it interacts properly with non-PBL physics and dynamics in a coastal-zone environment. The impact of grid-space vertical resolution on the results is also investigated. Since the "correct" solution to this idealized case is unknown, the comparison between the spectral model and the Blackadar and Gayno-Seaman models serves as a benchmark or "reality check" to demonstrate that the spectral model produces physically realistic results comparable to other high-resolution boundary-layer parameterizations.

Case	Vertical Resolution (layers)	PBL Model	Experiment Name
<b>Idealized</b>	<b>55</b>	<b>Spectral - Bulk</b>	I55-SPB
<b>Idealized</b>	<b>55</b>	<b>Spectral - Virtual</b>	I55-SPV
<b>Idealized</b>	<b>55</b>	<b>Blackadar</b>	I55-BL
<b>Idealized</b>	<b>55</b>	<b>Gayno-Seaman</b>	I55-GS
<b>Idealized</b>	<b>32</b>	<b>Spectral - Bulk</b>	I32-SPB
<b>Idealized</b>	<b>32</b>	<b>Spectral - Virtual</b>	I32-SPV
<b>Idealized</b>	<b>32</b>	<b>Blackadar</b>	I32-BL
<b>Idealized</b>	<b>32</b>	<b>Gayno-Seaman</b>	I32-GS
ARM CART	32	<b>Spectral - Bulk</b>	SPB
ARM CART	32	<b>Spectral - Virtual</b>	SPV
ARM CART	32	<b>Blackadar</b>	BL
ARM CART	32	<b>Gayno-Seaman</b>	GS

Table 3.1. Experimental Design.

The domain for the idealized experiments is designed to simulate a coastal-zone environment similar to that of southern California (Fig. 3.1). For this test, a 31 X 31 grid-point domain with 27-km horizontal resolution is used. An idealized coastline runs diagonally from the northwest corner to the southeast corner of the domain. The northeast half of the domain is uniformly flat grassland with elevation of one meter, while the southwest half is water.

In order to evaluate the impact of grid-space vertical resolution on the results of the spectral scheme, all idealized tests are run with both 55 vertical layers (21 in the lowest kilometer) and 32 vertical layers (12 in the lowest kilometer). The vertical distributions of sigma layers used in this set of experiments are summarized in Tables 3.2 and 3.3.

The initial conditions are computed using a calm-wind single-sounding initialization based on the temperature and moisture profiles at San Nicolas Island at 0000 UTC (1700 LDT), 30 August 1993 (Fig. 3.2). Mass fields are specified to be in thermal-wind balance with the wind field. In this case with calm initial winds, mass fields are initially constant in space on pressure surfaces. Initial sea surface temperatures vary realistically from cooler temperatures in the northern part of the domain to warmer temperatures in the southern part (Fig. 3.1). Sea surface temperatures remain constant throughout the simulations.



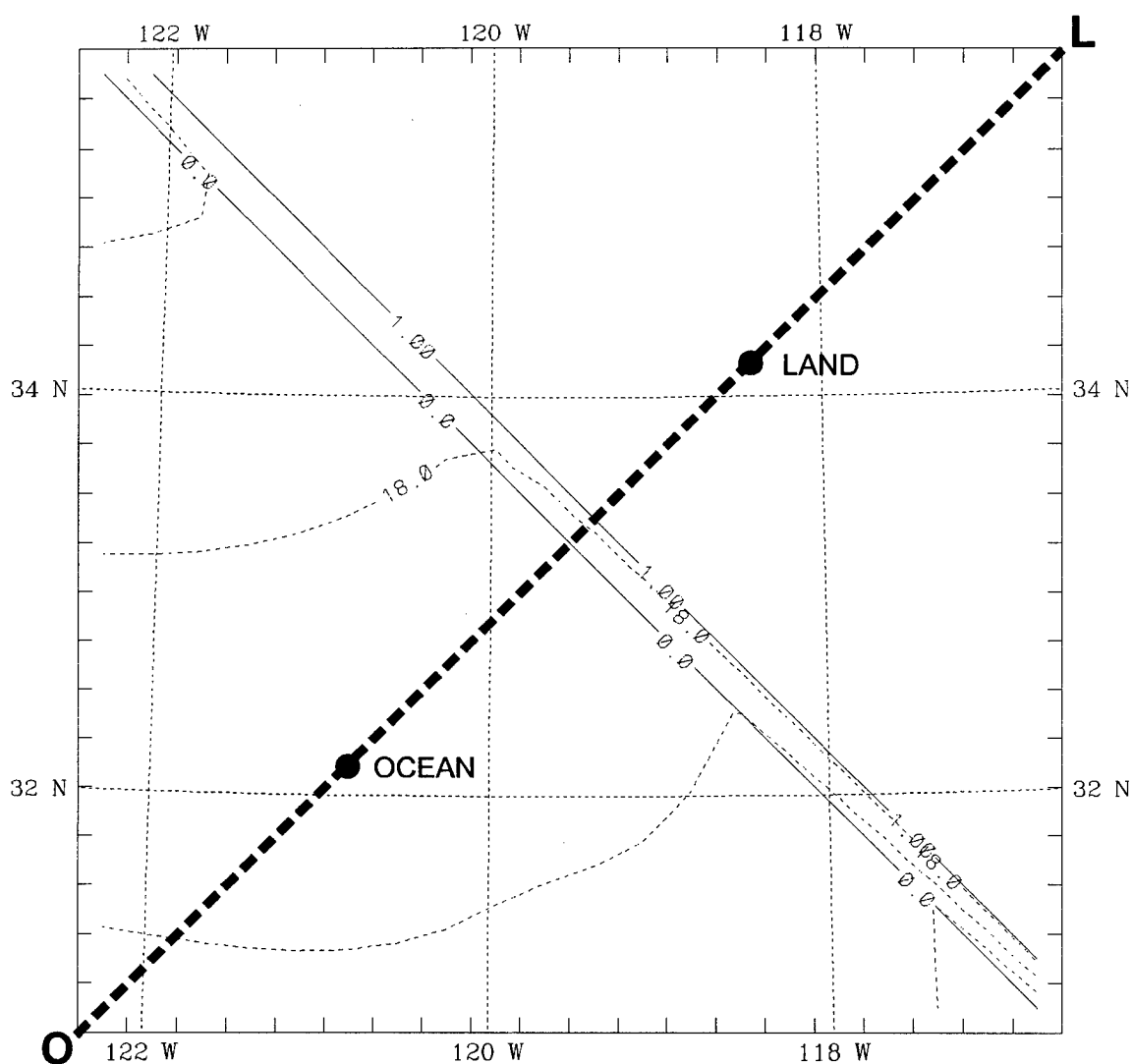


Figure 3.1. Idealized-case coastal-zone domain, sea surface temperature field ( $^{\circ}\text{C}$ ) and terrain height (m). Terrain heights (contour interval of 1 m) denote coastline with sea-surface temperatures (contour interval of  $1^{\circ}\text{C}$ ) to the west. Line segment O-L defines a southwest-northeast cross section used to display results in Chapter 5. Points "Ocean" and "Land" indicate the location of atmospheric soundings in Chapter 5.

Layer	Half Layer Sigma	Reference Pressure (mb)	Height (m AGL)
16	0.6550	689.5	3255
17	0.6860	717.4	2898
18	0.7170	745.3	2557
19	0.7380	764.2	2335
20	0.7600	784.0	2108
21	0.7724	795.2	1983
22	0.7847	806.2	1861
23	0.7970	817.3	1741
24	0.8048	824.3	1666
25	0.8125	831.3	1593
26	0.8202	838.2	1520
27	0.8280	845.2	1448
28	0.8345	851.1	1387
29	0.8410	856.9	1328
30	0.8475	862.8	1268
31	0.8540	868.6	1210
32	0.8613	875.2	1144
33	0.8687	881.8	1079
34	0.8760	888.4	1014
35	0.8820	893.8	962
36	0.8880	899.2	910
37	0.8940	904.6	858
38	0.8993	909.4	813
39	0.9047	914.2	767
40	0.9100	919.0	722
41	0.9153	923.8	677
42	0.9207	928.6	632
43	0.9260	933.4	588
44	0.9313	938.2	544
45	0.9367	943.0	500
46	0.9420	947.8	457
47	0.9473	952.6	414
48	0.9527	957.4	370
49	0.9580	962.2	328
50	0.9655	969.0	268
51	0.9730	975.7	209
52	0.9795	981.6	158
53	0.9860	987.4	108
54	0.9910	991.9	69
55	0.9960	996.4	31

Table 3.2. Sigma-layer distribution below ~ 700 mb for 55-layer idealized experiments.

Layer	Half Layer Sigma	Reference Pressure (mb)	Height (m AGL)
12	0.6500	685.0	3315
13	0.6900	721.0	2854
14	0.7300	757.0	2419
15	0.7600	784.0	2108
16	0.7800	802.0	1908
17	0.8000	820.0	1713
18	0.8200	838.0	1522
19	0.8400	856.0	1337
20	0.8600	874.0	1156
21	0.8800	892.0	979
22	0.9000	910.0	807
23	0.9150	923.5	680
24	0.9250	932.5	597
25	0.9350	941.5	514
26	0.9450	950.5	433
27	0.9550	959.5	352
28	0.9640	967.6	280
29	0.9720	974.8	217
30	0.9800	982.0	154
31	0.9880	989.2	92
32	0.9960	996.4	31

Table 3.3. Sigma-layer distribution below ~ 700 mb for 32-layer idealized and ARM-CART experiments.

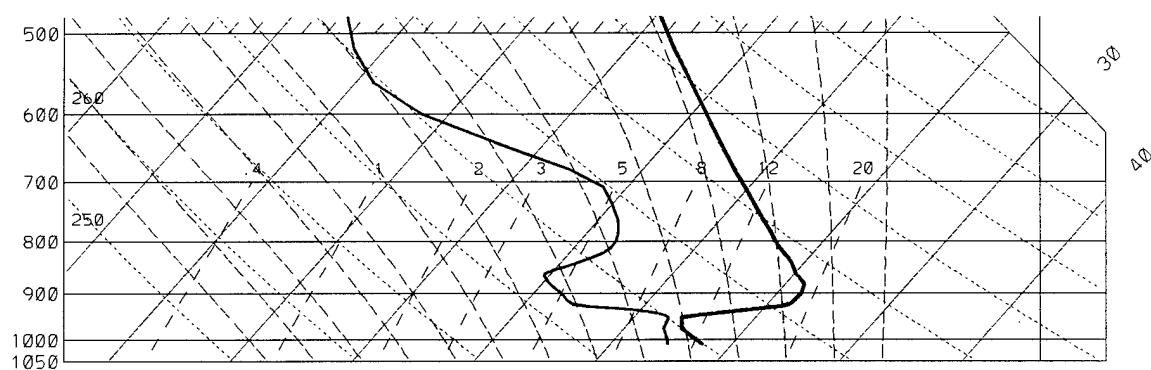


Figure 3.2. Temperature and moisture profiles from San Nicolas Island, 0000 UTC (1700 LDT) 30 August 1993, used for single-sounding initialization of MM5.

### 3.2 ARM-CART Case

The U.S. Department of Energy's Southern Great Plains (SGP) Atmospheric Radiation Measurement (ARM) Cloud and Radiation Testbed (CART) site provides a unique opportunity to verify model results using independent special data sets with higher spatial and temporal resolution than that routinely available. The SGP ARM-CART site offers relatively homogeneous geography, and the case chosen for this research is during an intense observation period (IOP) with dry, building high-pressure conditions, behind a cold front. No synoptic weather systems move through the ARM-CART region during the 48-h simulation period.

This case is also simulated using all three PBL schemes (Table 3.1) and a typical, 32-layer model vertical resolution with 12 layers in the lowest kilometer (Table 3.3). The set of experiments over the SGP site is conducted using a 36-km 100 X 100 grid-point mesh centered over the SGP central facility (Fig. 3.3). As shown by the terrain outside of the SGP site in Fig. 3.3, this case also introduces the effects of complex topography on the spectral-gridpoint coupling methodology used in the spectral PBL scheme within MM5. Therefore, the ARM-CART experiments, although focussed on the Kansas-Oklahoma region, also test the robustness of the new spectral PBL scheme in MM5 in a wide variety of land-use, terrain, and atmospheric stability conditions.

The SGP ARM-CART site (U.S. DOE ARM Fact sheet 1997) contains a series of in-situ and remote-sensing instrument clusters arrayed across approximately 55,000 square miles of north central Oklahoma and south central Kansas. The heart of the SGP site is

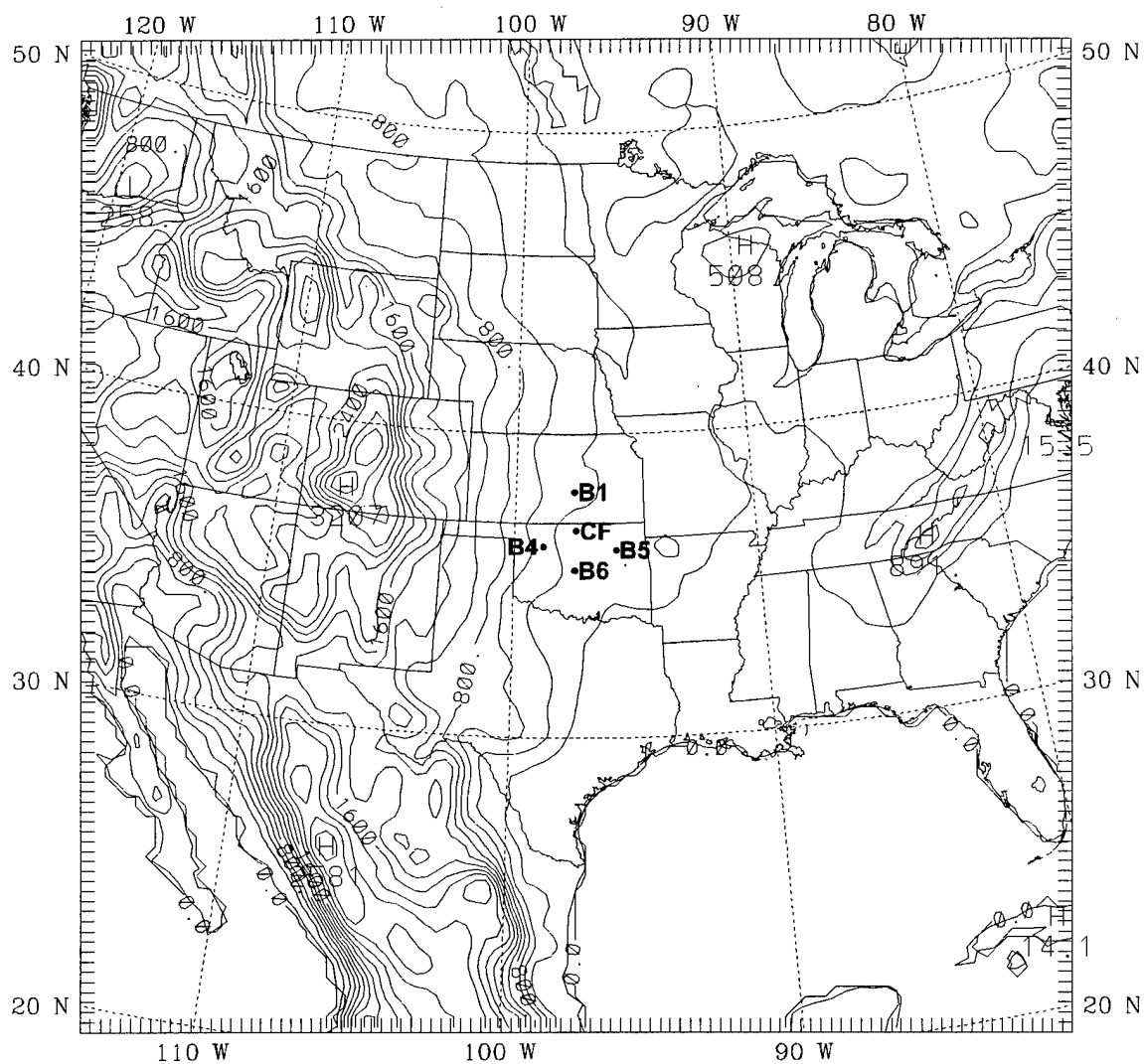


Figure 3.3. ARM-CART case domain and terrain field (m). Contour interval of terrain is 200m. The locations of the ARM-CART central facility (CF) and four boundary facilities (B1, B4, B5, and B6) are also labeled.

the heavily instrumented Central Facility located on 160 acres of cattle pasture and wheat field southeast of Lamont, Oklahoma. Data are collected from the Central Facility instruments and from 27 smaller, unmanned instrument arrays throughout the site. Instrumentation includes radiosondes, released up to eight times per day, energy balance Bowen ratio (EBBR) stations that measure soil temperature, net radiation, and fluxes of heat and moisture at the surface, a microwave radiometer that measures total column liquid water, and standard surface observations with high spatial and temporal density.

The 48-h real-data experiment conducted over the SGP ARM-CART site is initialized at 0000 UTC on 12 April 1997. The initial and boundary conditions are derived from the European Center for Medium-Range Weather Forecasts Tropical Ocean and Global Atmosphere program (ECMWF/TOGA) global analysis, and standard rawinsonde and surface data. The special data sets from the ARM-CART site are not used for MM5 model input and thus represent independent data for verification. Sea surface temperatures are specified from National Meteorological Center (NMC) analysis. Lateral boundary conditions are updated every 12 hours.

## Chapter 4 ARM-CART CASE DESCRIPTION

The case selected for this research is chosen because of its uniform forcing over the ARM-CART (AC) special data site during the IOP from 0000 UTC, 12 April 1997 to 0000 UTC, 14 April 1997. During this dry, post-frontal time period, evolution of PBL depth was determined primarily by local forcing and some advection. In addition, this time period allows the use of special data with high temporal and spatial density for independent verification of model output.

The 500-mb height analysis for 0000 UTC, 12 April 1997 (Fig. 4.1a) shows a broad area of low heights in the southern branch of the 500-mb flow, and centered to the northwest of the AC site. Through the 48-h period simulated here, the trough in the northern branch deepens slightly as the southern trough lifts out and merges with the northern trough. The trough system then continues to move eastward towards New England (Fig 4.1b-c). At the surface, low pressure is centered over St. Louis at the initial time with a cold front extending southwestward to the coast of Texas and a warm front extending eastward to the Atlantic (Fig. 4.2a). High pressure is pushing southeastward from Montana producing northwesterly winds, cold advection, and extensive cloudiness that dominate the AC site through the first day. The low-pressure center moves northeastward off the New England coast and the cold front moves across the Gulf of Mexico, and the clouds over Kansas and Oklahoma dissipate through the second day (Fig. 4.2b-c).



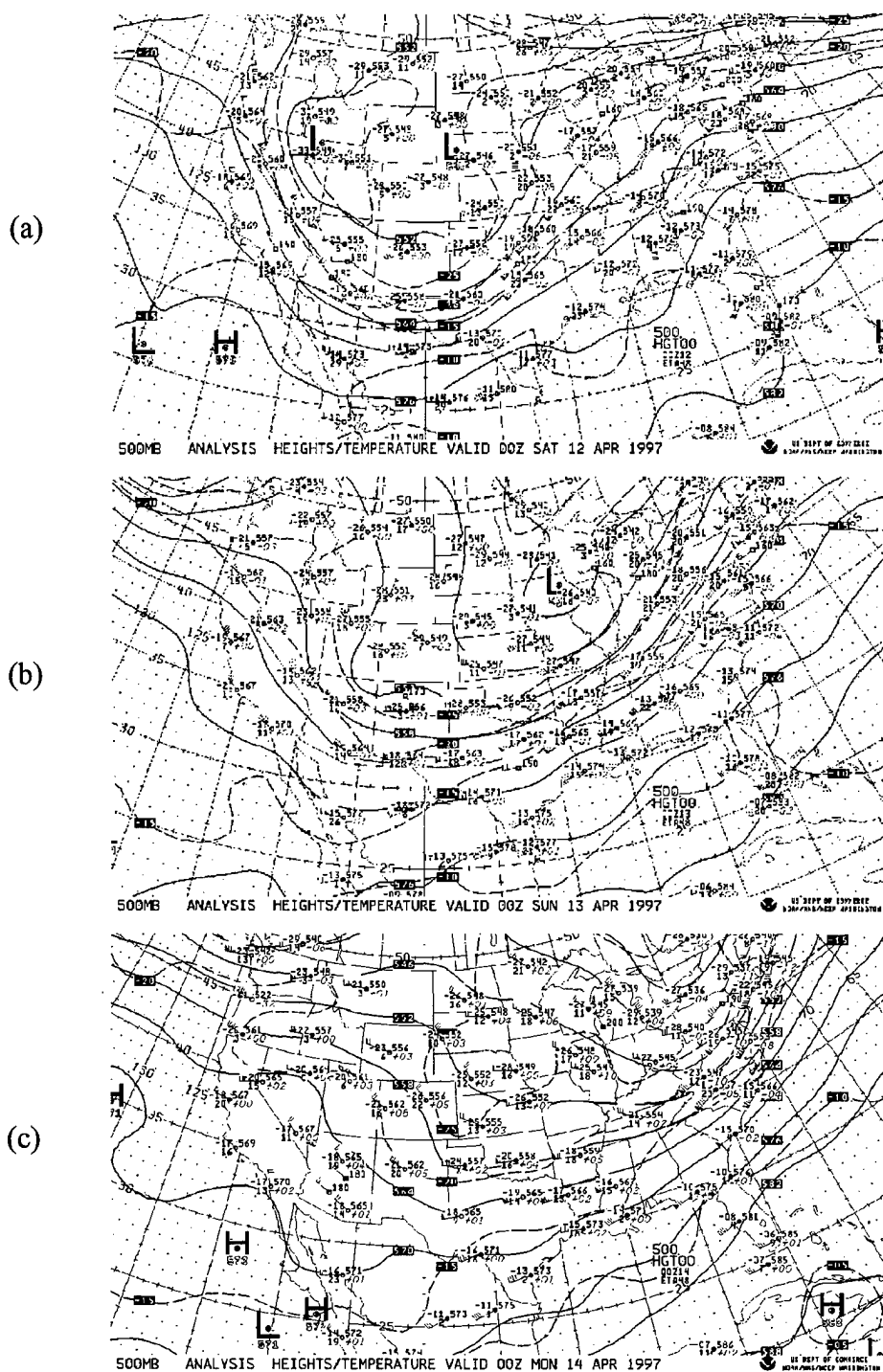


Figure 4.1. Analysis of 500-mb geopotential height and temperature valid (a) 0000 UTC, 12 April 1997, (b) 0000 UTC, 13 April 1997, and (c) 0000 UTC, 14 April 1997.

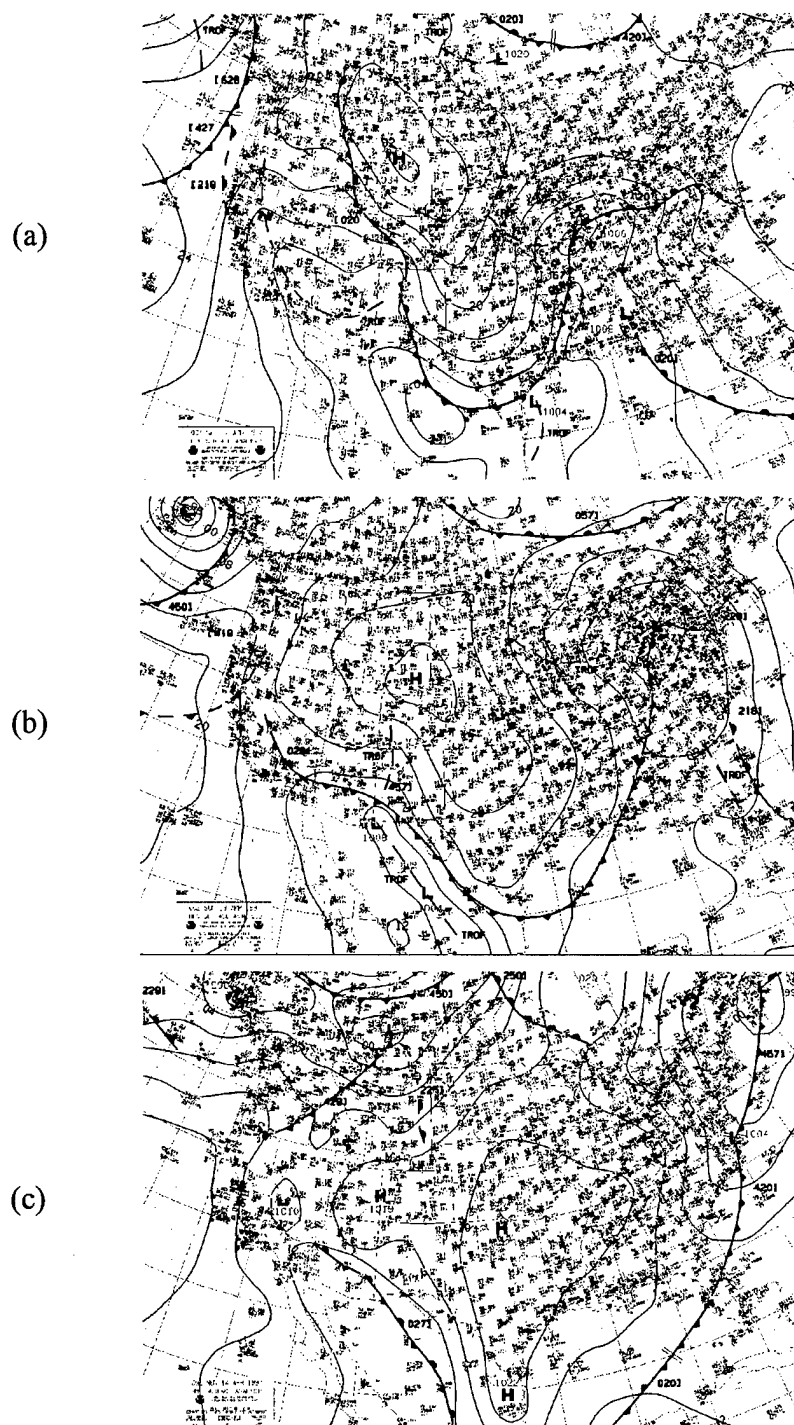


Figure 4.2. Surface analysis valid (a) 0000 UTC, 12 April 1997, (b) 0000 UTC, 13 April 1997, and (c) 0000 UTC, 14 April 1997.

## Chapter 5 EXPERIMENTAL RESULTS

In this chapter, the results of the experiments outlined in Chapter 3 are discussed. The first section presents the results of the idealized tests and examines the effects of vertical resolution and non-PBL physics on model results, and benchmarks the spectral model against the Blackadar and Gayno-Seaman models. The second section compares the results of the spectral model with independent special data from the ARM-CART site, as well as with the results of the other two PBL models. A comparison of model computational costs is included at the end of each section.

### 5.1 Idealized Case

Because of the idealized nature of this model intercomparison, results in this section are presented more qualitatively than quantitatively. Although the "correct" solution is not known, what constitutes a reasonable or realistic solution is known, based on climatology and experience with somewhat similar real-data cases. Initial testing of the PBL schemes is focused on the 55-layer experiments (Table 3.1) representing relatively high vertical resolution and that necessary to adequately resolve the structure of the MBL. This will allow a determination of whether or not the spectral scheme interacts properly with the non-PBL physics and dynamics modules. The 32-layer experiments are discussed later in this section to examine the impact of reduced and more typical vertical grid-space resolution (Mass and Kuo 1998) on each boundary-layer model.

Each of the model solutions examined here is integrated forward from the same initial conditions and lateral boundary conditions. However, horizontal plots of PBL depth (Fig. 5.1) at the 12-h forecast time, 1200 UTC (0500 LDT), show differences between the spectral model (Exps. I55-SPB and I55-SPV) and the Blackadar and Gayno-Seaman models (Exps. I55-BL and I55-GS respectively). Because no deep convection occurs during this case, any differences between Exps. I55-SPB and I55-SPV are entirely due to differences in the initial diagnosis of PBL depth. Experiments I55-SPB and I55-SPV both develop a marine PBL surface with greater spatial coherence than that of the other two experiments. These spectral-model results reflect the technique used to diagnose the initial PBL depth and the use of a prognostic equation with horizontal advection and diffusion to determine PBL depth. All four experiments show a general offshore pattern of deeper PBL depths from north to south, consistent with summertime climatology for this region (Neiburger et al. 1961). The values of the maximum PBL depths over the ocean are also comparable in all four experiments. It should also be noted that over land both Exps. I55-BL and I55-GS diagnose the PBL height to be zero during this stable nocturnal regime, while the spectral experiments are constrained to produce a depth no less than that of the lowest model full-level (60 m).

Figures 5.2 and 5.3 show vertical cross sections of potential temperature and cloud water at the 12-h forecast time along cross-section O-L (Fig.3.1). Temperatures over land are very similar in all four experiments, while the boundary layers over the water in Exps. I55-SPB and I55-SPV are more stably stratified and about 1 °C cooler than I55-BL

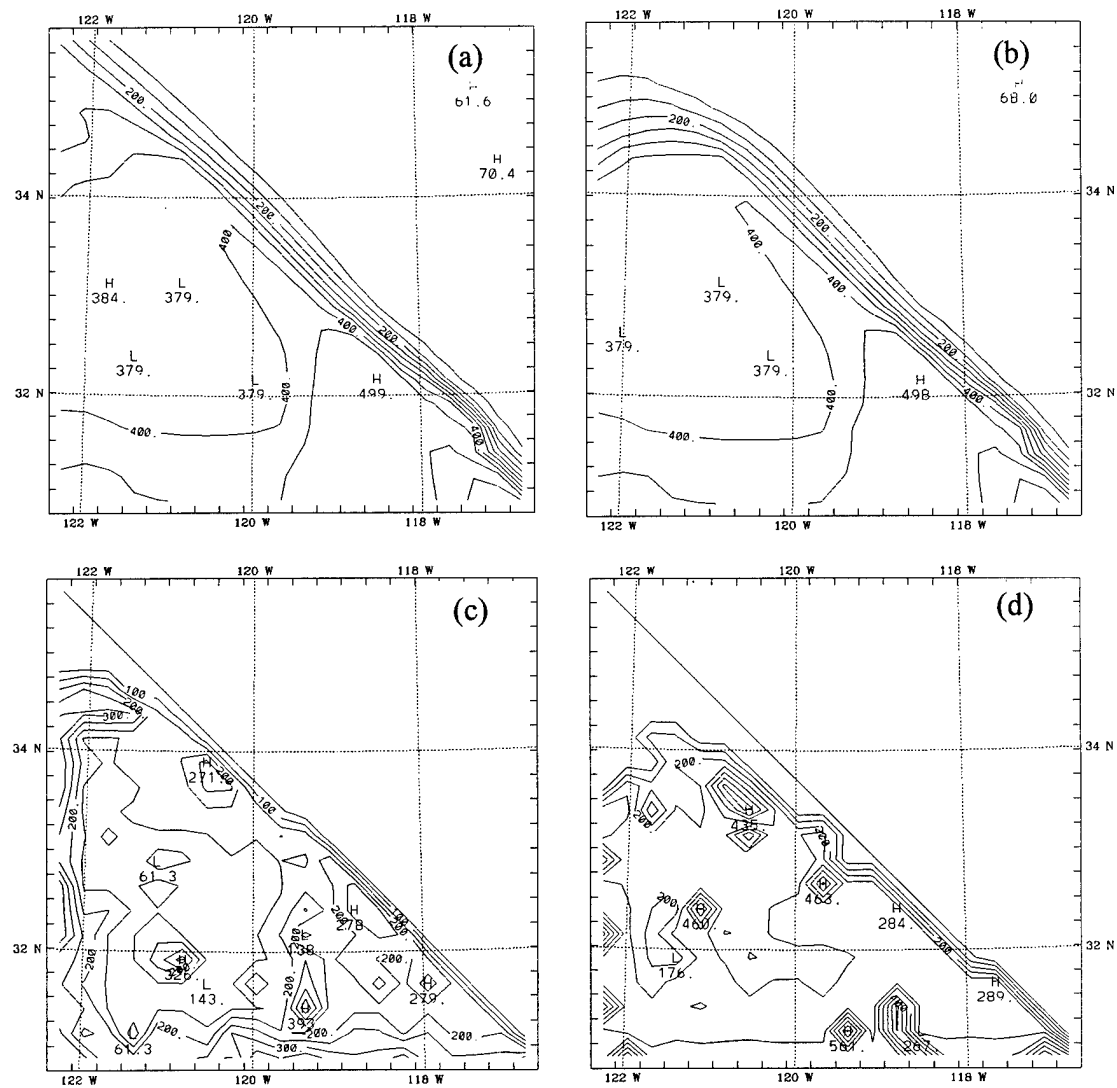


Figure 5.1. Model-predicted PBL depth (contour interval of 50 m), at 12 h (1200 UTC) for (a) I55-SPB, (b) I55-SPV, (c) I55-BL and (d) I55-GS.

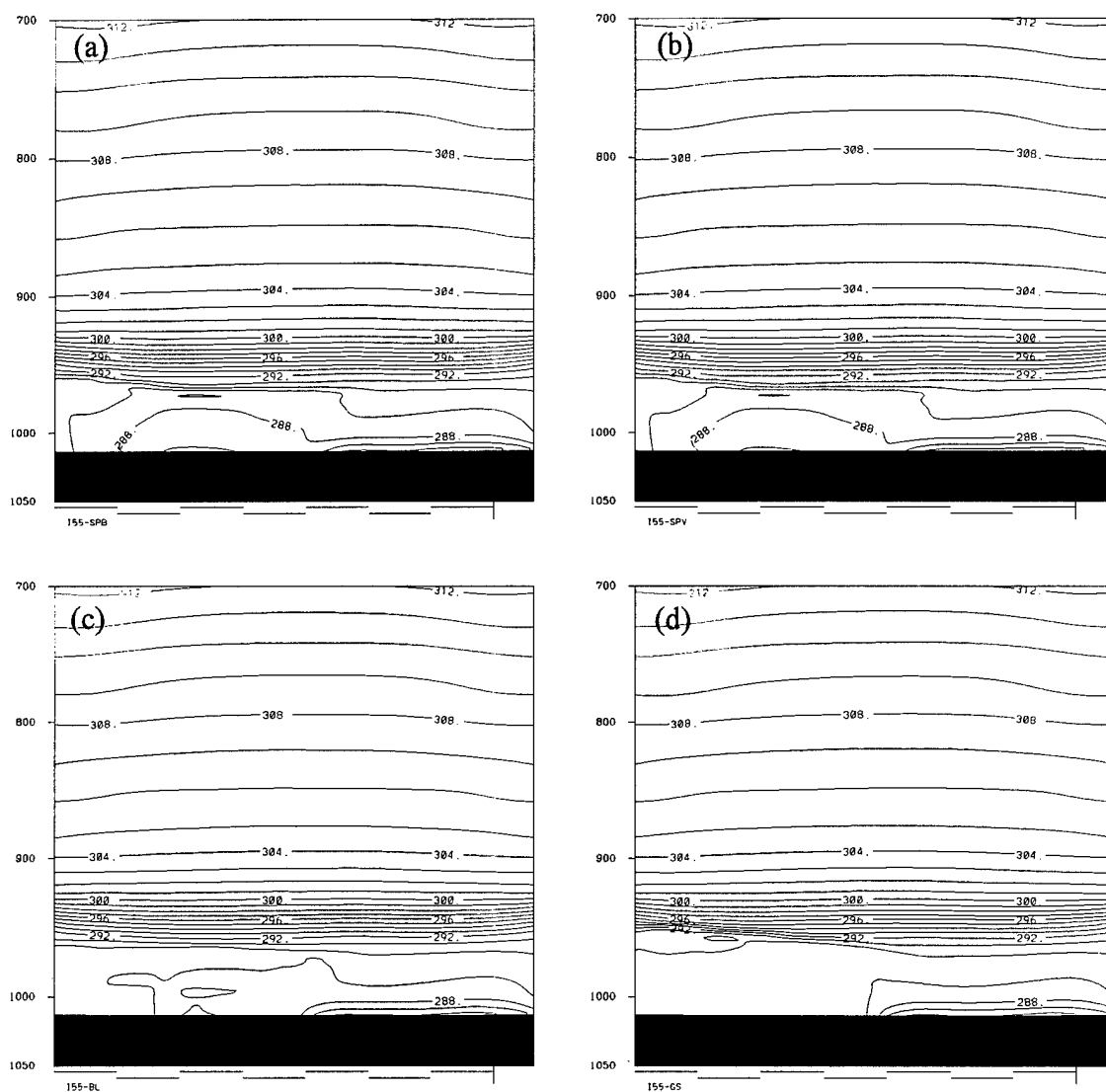


Figure 5.2. Vertical cross-section of potential temperature (contour interval of 1 K) at 12 h (1200 UTC) along line segment O-L (Fig. 3.1), for (a) I55-SPB, (b) I55-SPV, (c) I55-BL, and (d) I55-GS.

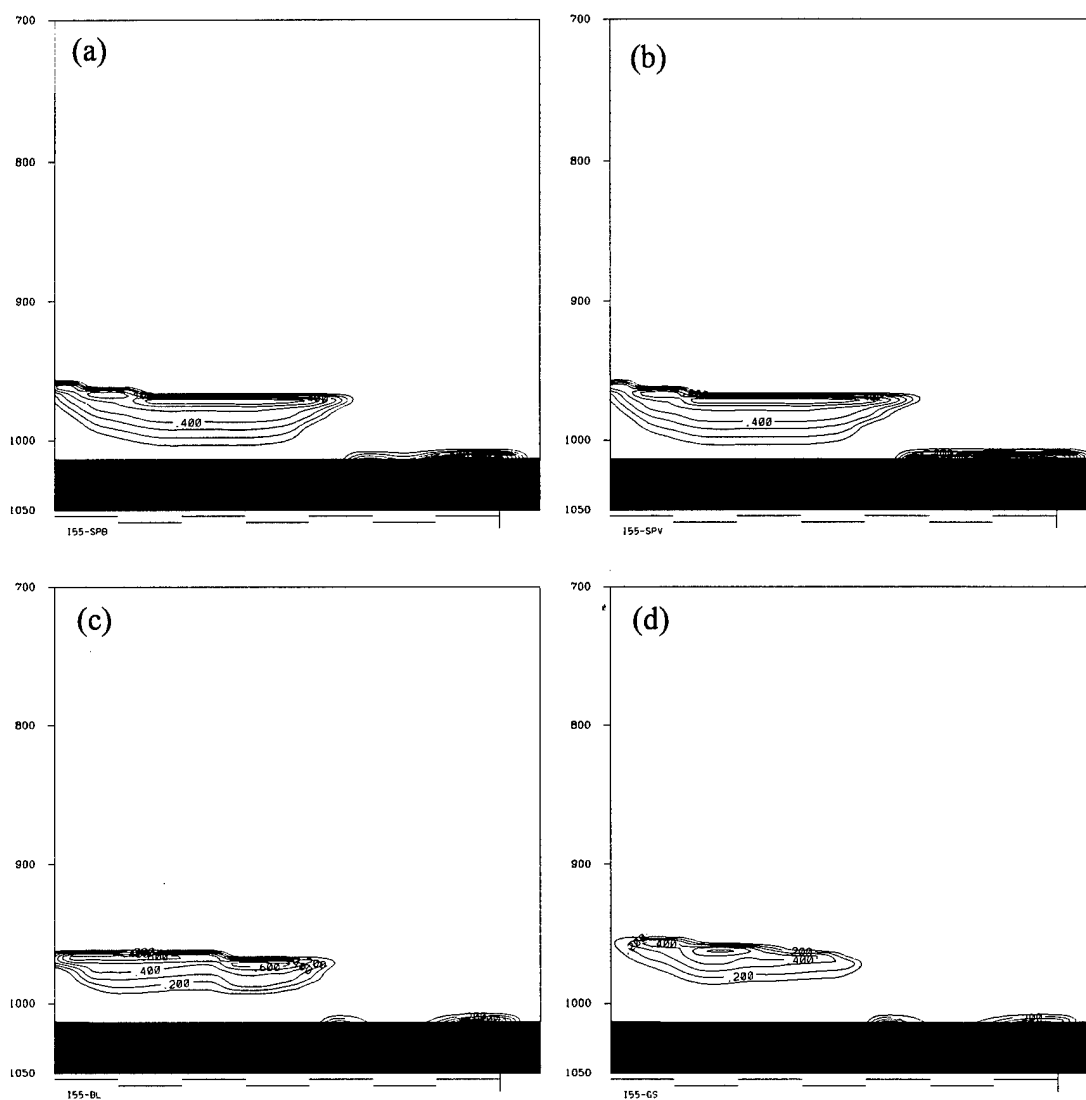


Figure 5.3. Vertical cross-section of cloud water (contour interval of  $0.1 \text{ g kg}^{-1}$ ) at 12 h (1200 UTC) along line segment O-L (Fig. 3.1), for (a) I55-SPB, (b) I55-SPV, (c) I55-BL, and (d) I55-GS.

and I55-GS along this cross-section (Fig. 5.2). Figure 5.3 shows that all four experiments have produced marine stratus of similar depth and extent, with reasonable values of cloud water concentration ( $\sim 0.5 \text{ g kg}^{-1}$ ). Each experiment shows a gradual downward slope of the marine stratus top towards the coast, consistent with climatology. This slope is most pronounced in Exp. I55-GS, and is also apparent in the corresponding gradients of potential temperature in Fig. 5.2. Over land, all four experiments develop some fog by this time.

Atmospheric soundings over water (Fig. 5.4) at this time show a typical shallow MBL, with its inversion base at about 400 m AGL. All four experiments produce moist adiabatic lapse rates in the cloud layers, with Exps. I55-BL and I55-GS producing shallow dry-adiabatic layers near the surface. Over land (Fig. 5.5) at the 12-h forecast time all four experiments develop very similar radiation inversions at the surface, with fog. Winds at this time are still very weak at both locations and for all experiments.

At 24 h (0000 UTC or 1700 LDT), each of the experiments has a well-developed boundary layer over land due to the daytime heating (Fig. 5.6). The general pattern is similar among the four experiments, with maximum values over land ranging from 1222 m in Exp. I55-GS to 1178 m in Exp. I55-BL, while minimum depths over land away from the coastline range from  $\sim 1025$  m in I55-GS to 818 m in I55-SPV. Over water, the two spectral experiments again develop more smooth, gradually sloping surfaces of PBL depth, while the PBL depth forecasted in I55-BL is somewhat noisier, and that in I55-GS ( $\sim 70$  m) is much shallower than the other experiments.



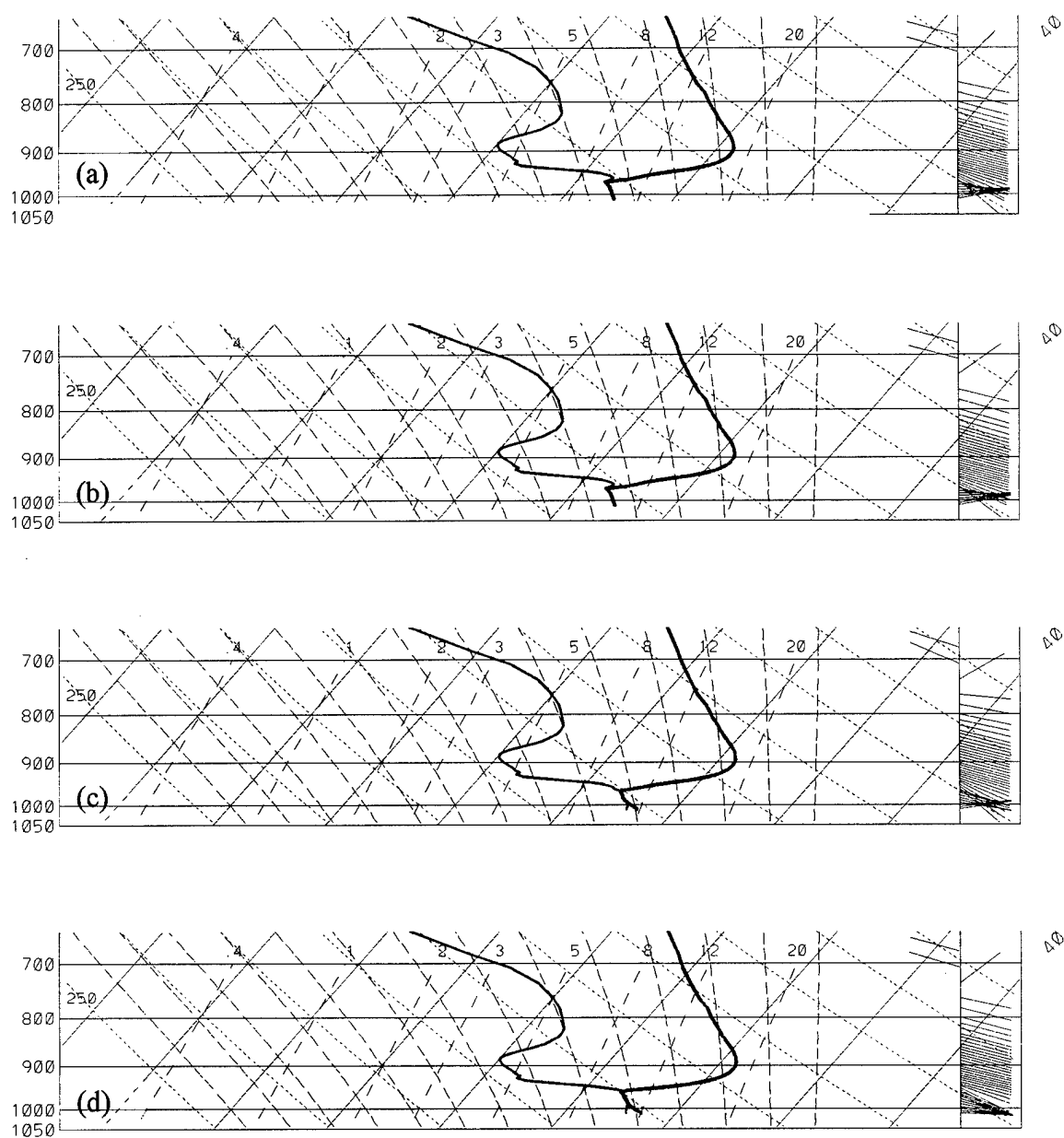


Figure 5.4. Temperature, moisture, and wind profiles for point "Ocean" (Fig. 3.1) at 12 h (1200 UTC) for (a) I55-SPB, (b) I55-SPV, (c) I55-BL, and (d) I55-GS.

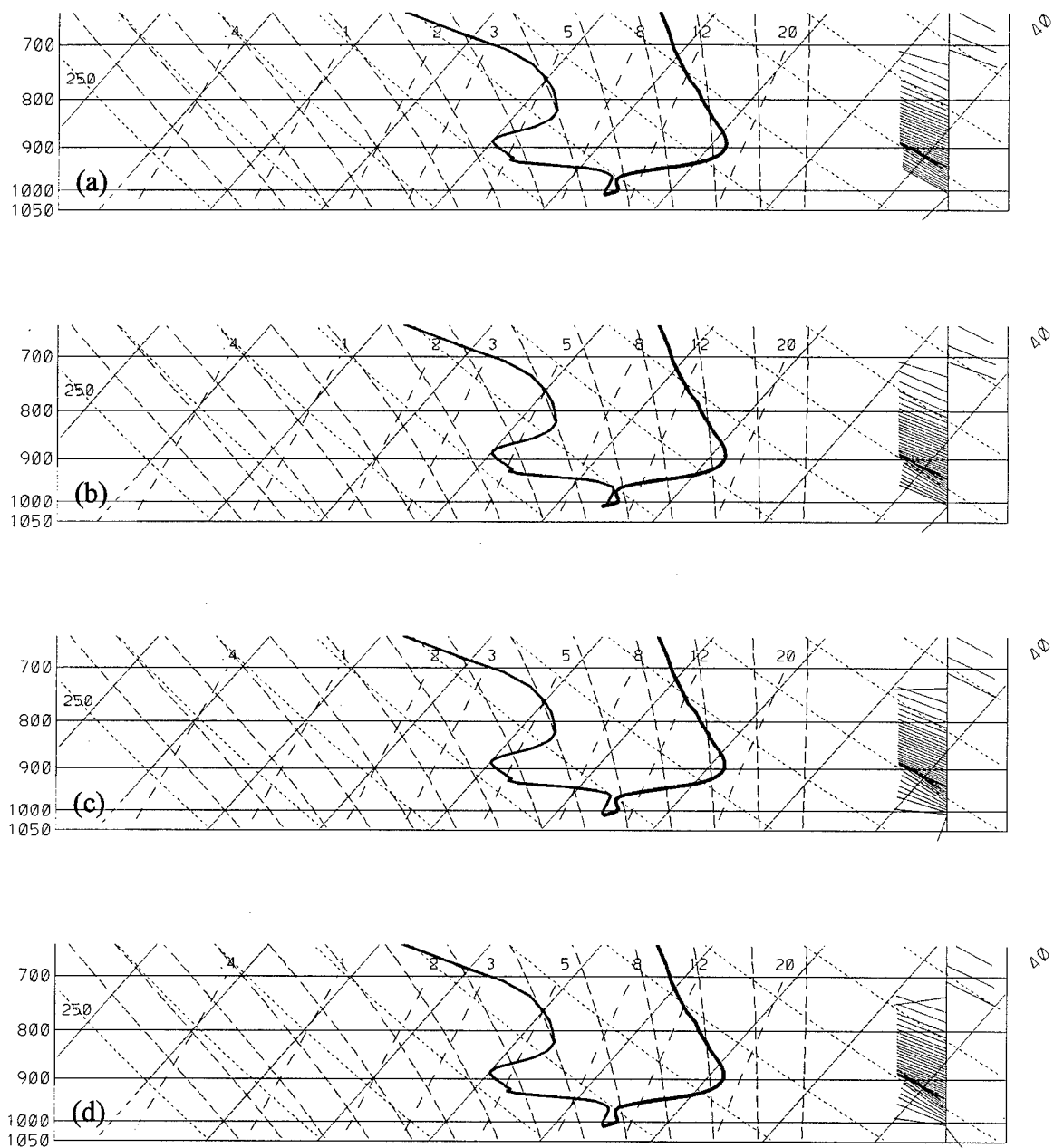


Figure 5.5. Temperature, moisture, and wind profiles for point "Land" (Fig. 3.1) at 12 h (1200 UTC) for (a) I55-SPB, (b) I55-SPV, (c) I55-BL, and (d) I55-GS.

Figure 5.6. Model-predicted PBL depth (contour interval of 50 m), at 24 h (0000 UTC) for (a) I55-SPB, (b) I55-SPV, (c) I55-BL and (d) I55-GS.

Daytime heating of the landmass has produced a sea-breeze circulation of around  $5 \text{ m s}^{-1}$  at the surface (Fig. 5.7), and extending to around 1 km depth (not shown) in all four experiments. Maximum surface wind speeds along the coastline are realistic (Banta, 1995) and range from  $5.61 \text{ m s}^{-1}$  in I55-GS to  $4.58 \text{ m s}^{-1}$  in I55-SPV. All four experiments develop very similar wind patterns with maximum values near the coast and in the northwest and southeast regions of the grid.

Figures 5.8 and 5.9 show vertical cross sections (along line O-L, Fig. 3.1) of potential temperature and cloud water at 24 h (0000 UTC). An examination of potential temperature in Fig. 5.8 shows a shallow MBL structure with deeper PBL depths sloping upward over land in response to the daytime heating. The difference in boundary-layer temperature over the water between the two spectral experiments and Exps. I55-BL and I55-GS has decreased to  $1^\circ\text{C}$  or less along this cross-section. Over land, Exp. I55-GS is warmer than the other experiments by  $1\text{-}3^\circ\text{C}$ . Of note are the sharp gradients of potential temperature coincident with the top of the marine stratus layer (Fig. 5.9) and likely due to evaporative and radiative cooling. These vertical gradients are nearly identical among Exps. I55-SPB, I55-SPV, and I55-BL, while that in Exp. I55-GS is about 50 percent weaker.

The weaker vertical gradients in I55-GS are apparently due to less mixing and weaker TKE profiles over the water compared to the strongly heated land. Vertical profiles of TKE (not shown) indicate that within the marine boundary layer a sharp vertical gradient

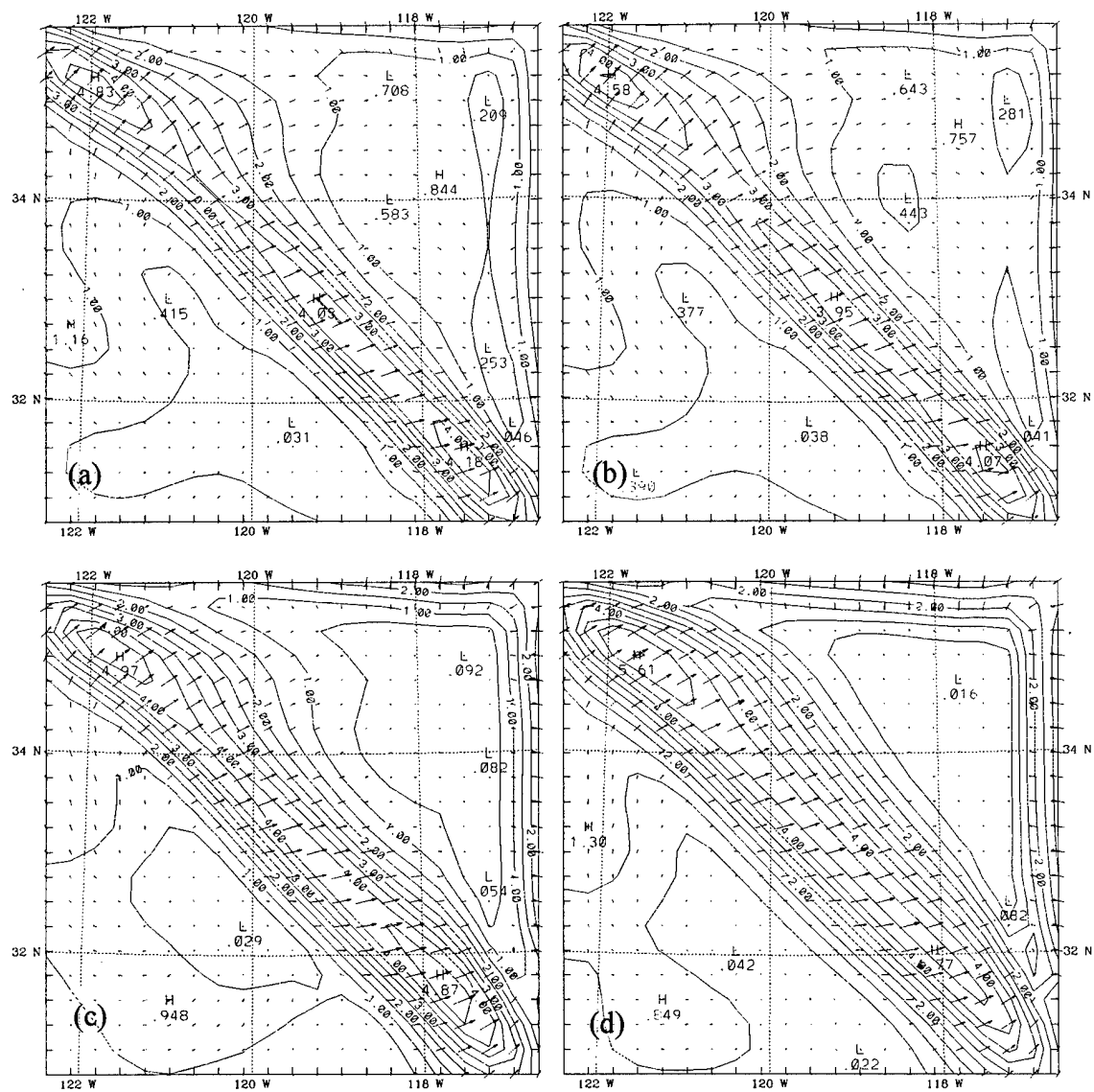


Figure 5.7. Wind speed (contour interval of  $0.5 \text{ m s}^{-1}$ ) with wind vectors, at 24 h (0000 UTC) for (a) I55-SPB, (b) I55-SPV, (c) I55-BL and (d) I55-GS.

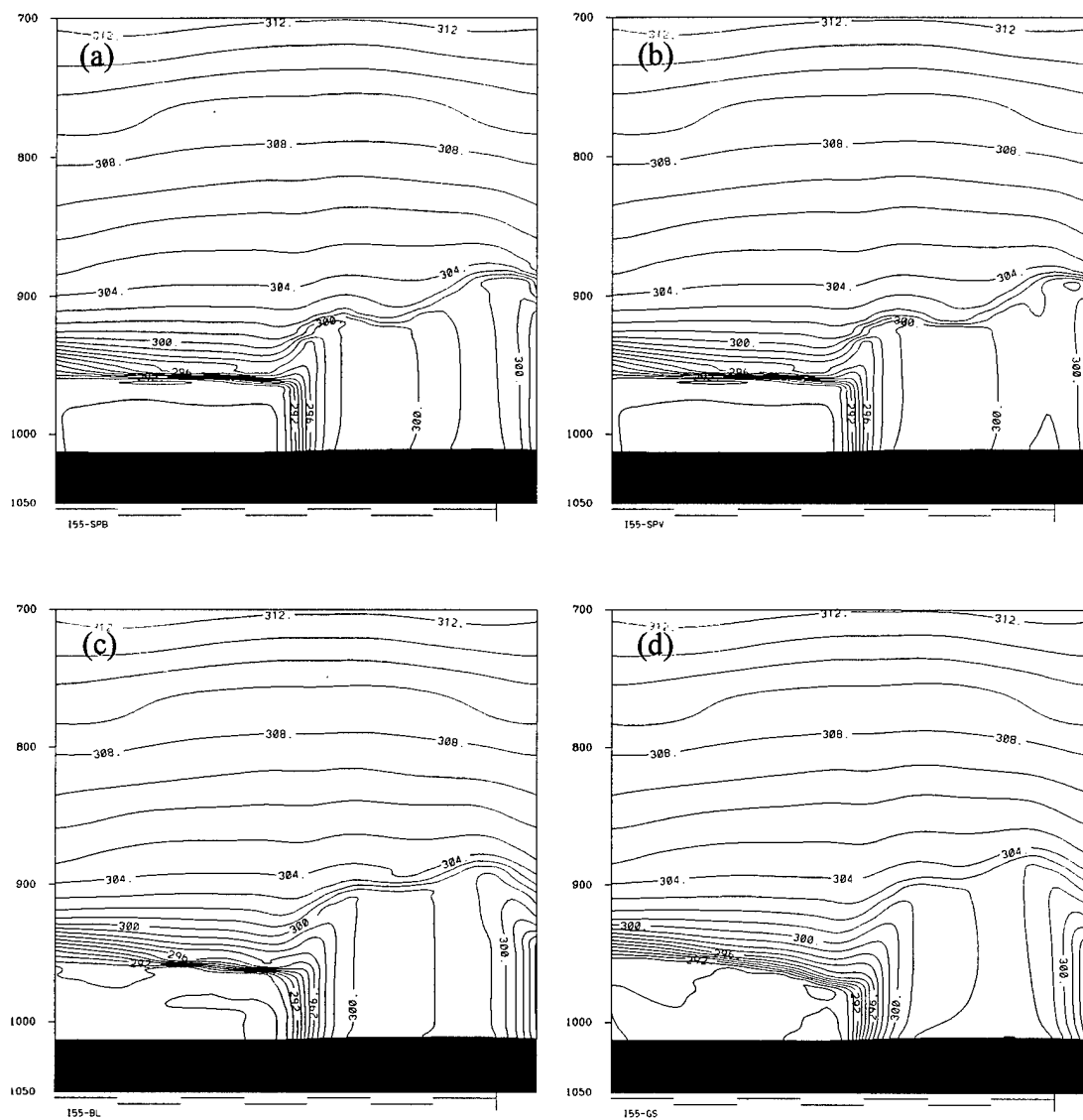


Figure 5.8. Vertical cross-section of potential temperature (contour interval of 1 K) at 24 h (0000 UTC) along line segment O-L (Fig. 3.1), for (a) I55-SPB, (b) I55-SPV, (c) I55-BL, and (d) I55-GS.

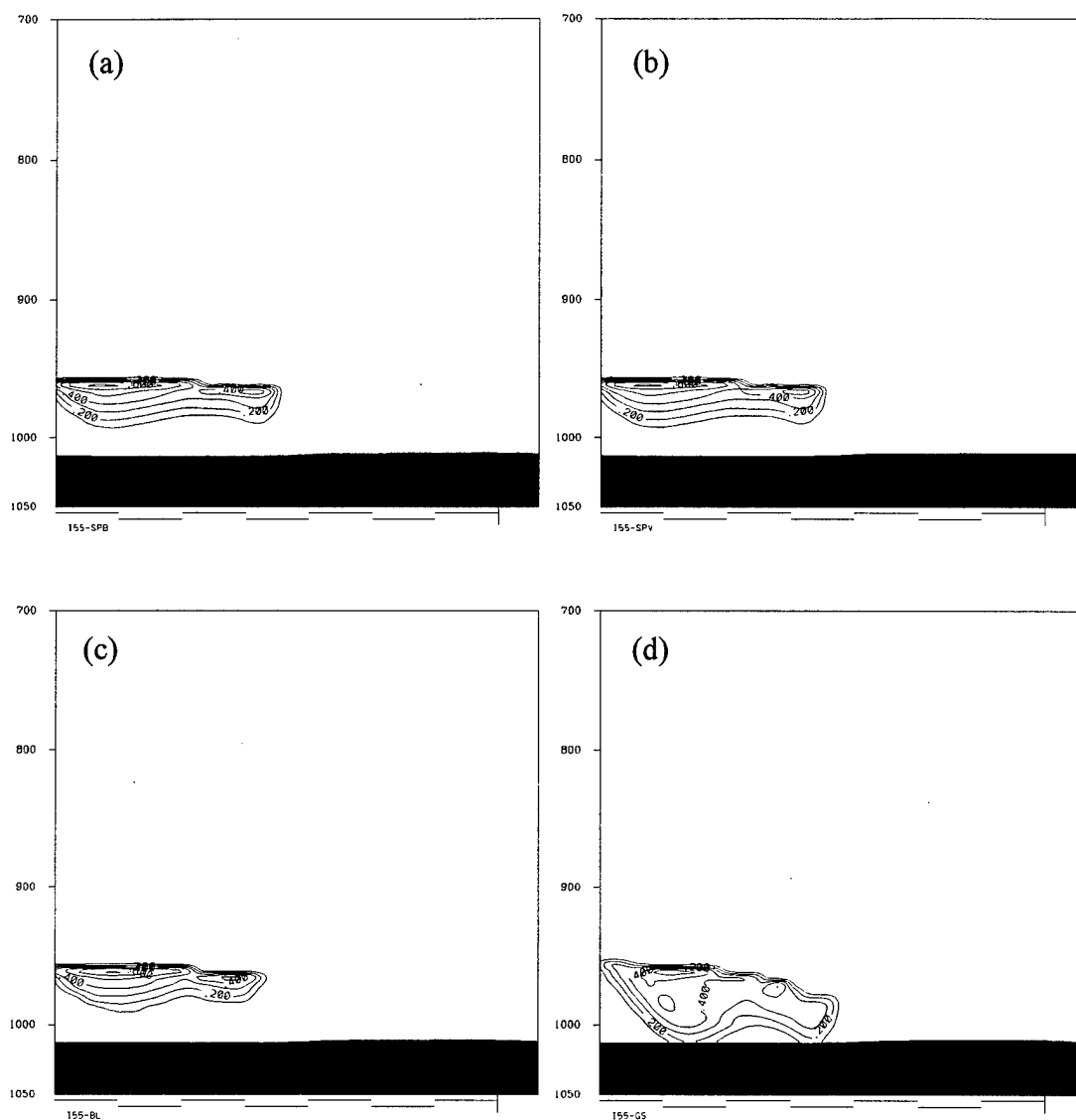


Figure 5.9. Vertical cross-section of cloud water (contour interval of  $0.1 \text{ g kg}^{-1}$ ) at 24 h (0000 UTC) along line segment O-L (Fig. 3.1), for (a) I55-SPB, (b) I55-SPV, (c) I55-BL, and (d) I55-GS.

coincides with the base of the inversion, but the magnitude of TKE is less than  $0.1 \text{ m}^2 \text{ s}^{-2}$ , the value used here to determine the depth of the boundary layer (see Section 2.2.2 for details). It appears that a smaller threshold value of TKE should be used to determine PBL depth over water as compared to land. Investigation of the best algorithm for determination of PBL depth over water is currently underway.

In addition, the marine stratus in I55-GS is much thicker than the other experiments, and extends down to the surface (Fig. 5.9). The top of the marine stratus still displays a slight downward slope in all four experiments, most notably in I55-GS.

It was shown in Fig. 5.6 that the boundary layer over water in Exp. I55-GS was very shallow compared to the other three experiments, yet in Fig. 5.8 the inversion base over water is approximately the same height as that in the other experiments. Therefore, the PBL depth and inversion base height are not necessarily the same.

Atmospheric soundings over the water at 24 h (Fig. 5.10) show that Exps. I55-SPB and I55-SPV develop shallow mixed layers below a moist-adiabatic saturated layer, while Exp. I55-BL develops a super-adiabatic saturated layer above a very shallow mixed layer. Experiment I55-GS forecasts an unstable saturated layer that reaches the surface. Again we see that Exps. I55-SPB and I55-SPV are within  $1^\circ\text{C}$  of the other two experiments at the surface at this time. In general, the more realistic moist-adiabatic saturated layers of I55-SPB and I55-SPV compared to I55-BL can most likely be attributed to the use of liquid potential temperature and total water as model variables, since these are approximately conserved for phase change processes (Betts, 1973).



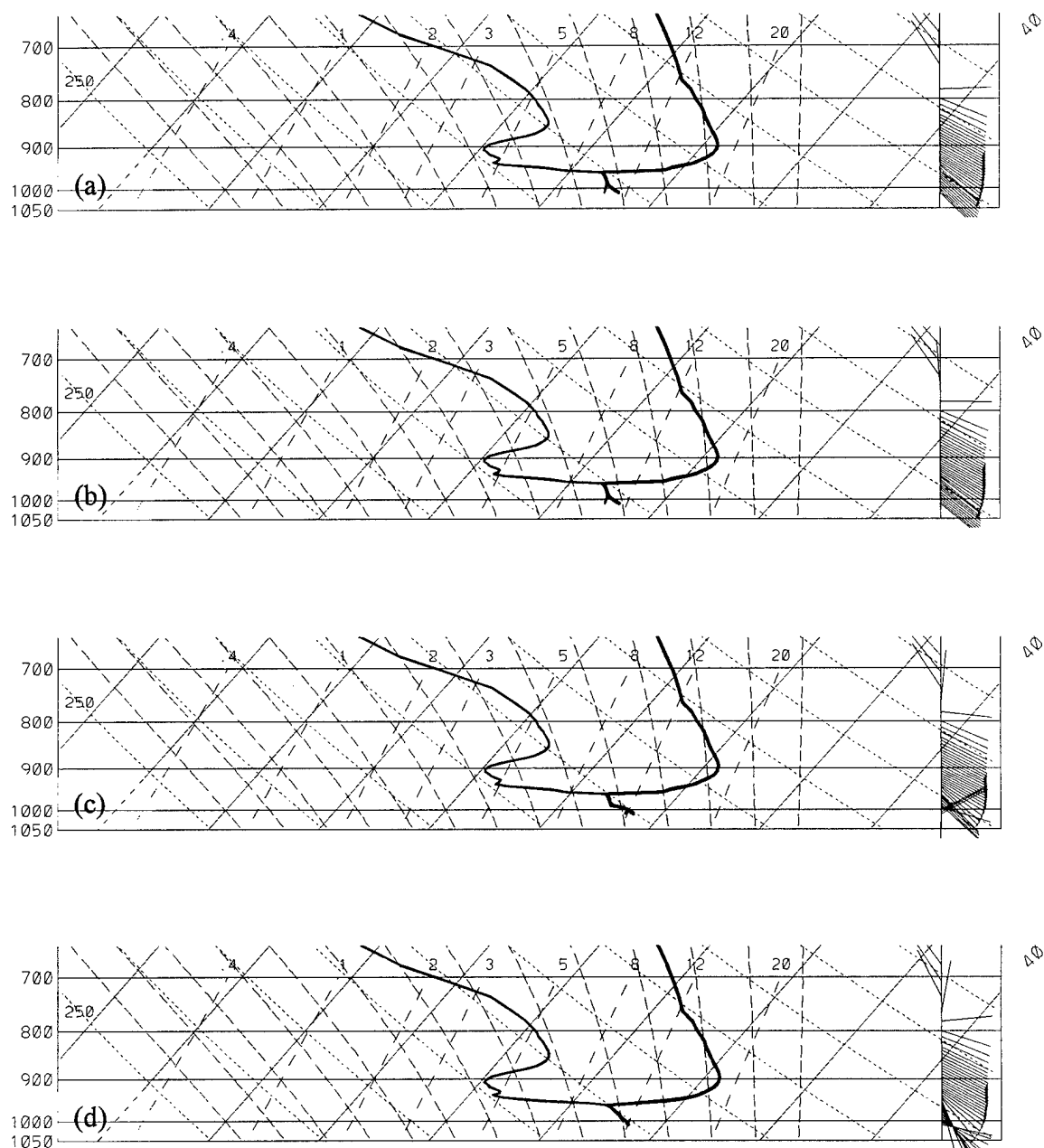


Figure 5.10. Temperature, moisture, and wind profiles for point "Ocean" (Fig. 3.1) at 24 h (0000 UTC) for (a) I55-SPB, (b) I55-SPV, (c) I55-BL, and (d) I55-GS.

Over land, all four experiments have soundings with well-developed mixed layers of about 1-km depth (Fig. 5.11). Experiment I55-GS has the weakest inversion, but has produced a shallow super-adiabatic layer at the surface that is not evident in the other experiments. It also has the warmest boundary layer of the four experiments, while I55-SPV is the coolest, 3 °C cooler than I55-GS at this location. The temperature difference between the spectral experiments and the "high-resolution" experiments may be the result of the amount of fog over land during the previous nocturnal period. Both spectral experiments produced somewhat more fog over land than the "high-resolution" experiments, thus delaying daytime radiative heating of the boundary layer. Experiment I55-GS has the greatest land-sea temperature difference, and produces the strongest sea breeze (Fig. 5.7). Note the similarity in the wind profiles after 24 h among the experiments in both Fig. 5.10 and Fig. 5.11, for water and land locations, respectively.

The production of marine stratus and stronger marine PBL-top inversions, the formation and dissipation of fog over land, and the development of a sea-breeze circulation indicate that the spectral model is interacting properly with the non-PBL physics and dynamics modules within MM5. Physically realistic interaction between the spectral scheme and the MM5 is indicated by its reasonable solutions and the degree of similarity in the MM5 results among the three PBL models.

A comparison between the 55-layer and 32-layer experiments is examined next to determine the impact of reduced vertical grid-space resolution on the PBL model results.

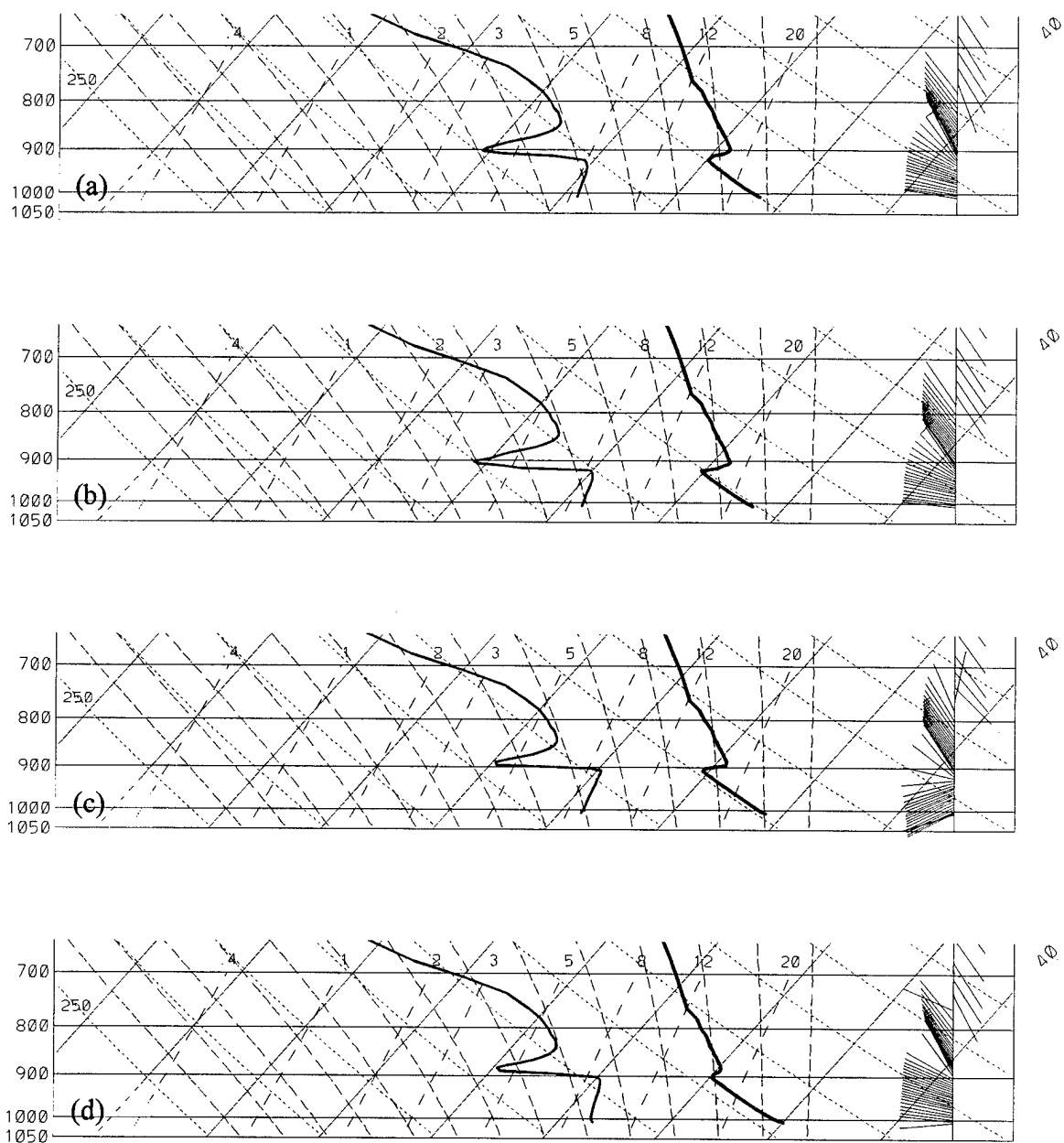


Figure 5.11. Temperature, moisture, and wind profiles for point "Land" (Fig. 3.1) at 24 h (0000 UTC) for (a) I55-SPB, (b) I55-SPV, (c) I55-BL, and (d) I55-GS.

At 24 h (0000 UTC), the horizontal patterns of PBL depths (not shown) predicted in Exps. I32-SPB, I32-SPV, I32-BL, and I32-GS are very similar to those shown in the 55-layer experiments (Fig. 5.6), although the magnitudes of maxima and minima have changed. The PBL depths over land in I32-SPB and I32-SPV are 130 - 140 m shallower than those of I55-SPB and I55-SPV, while the depths over water are approximately 80 m shallower than the 55-layer experiments. Experiments I32-BL and I32-GS show the opposite trend. The PBL depths over land in the 32-layer experiments (not shown) are approximately 80 m higher than those in Exps. I55-BL and I55-GS, while over water the PBL depths forecasted by Exps. I32-BL and I32-GS are 25 - 30 m higher than those of the 55-layer experiments.

Surface winds produced by the 32-layer experiments (not shown) at 24 h respond to decreased vertical resolution similarly to the PBL depths. Experiments I32-SPB and I32-SPV decrease the maximum predicted wind speed within the sea breeze by  $0.3 - 0.7 \text{ m s}^{-1}$  as compared to the 55-layer experiments (Fig. 5.7), while Exps. I32-BL and I32-GS increase the maximum wind speeds by  $0.2 - 0.25 \text{ m s}^{-1}$  over I55-BL and I55-GS.

A comparison of Figs. 5.8 and 5.9 with Figs. 5.12 and 5.13 shows gradients in both potential temperature and cloud water near the top of the stratus are as much as 50 percent weaker in the 32-layer experiments than in the 55-layer experiments. Also, while boundary-layer temperatures over water remain similar between the 32-layer and 55-layer experiments, temperatures in Exps. I32-SPB and I32-SPV over land are  $2^\circ\text{C}$  degrees cooler than in the 55-layer experiments. The most likely reason for this cooling is that

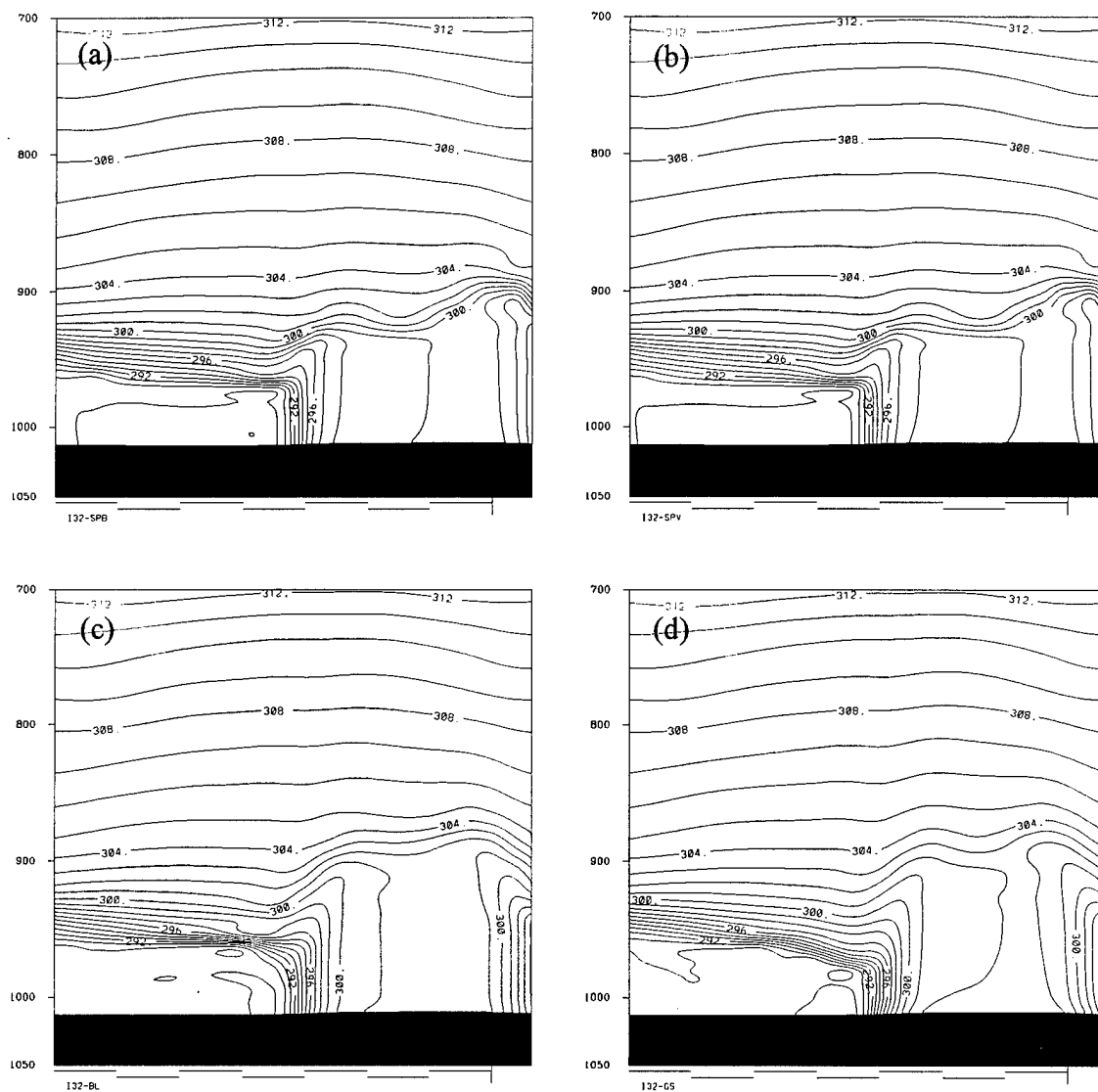


Figure 5.12. Vertical cross-section of potential temperature (contour interval of 1 K) at 24 h (0000 UTC) along line segment O-L (Fig. 3.1), for (a) I32-SPB, (b) I32-SPV, (c) I32-BL, and (d) I32-GS.

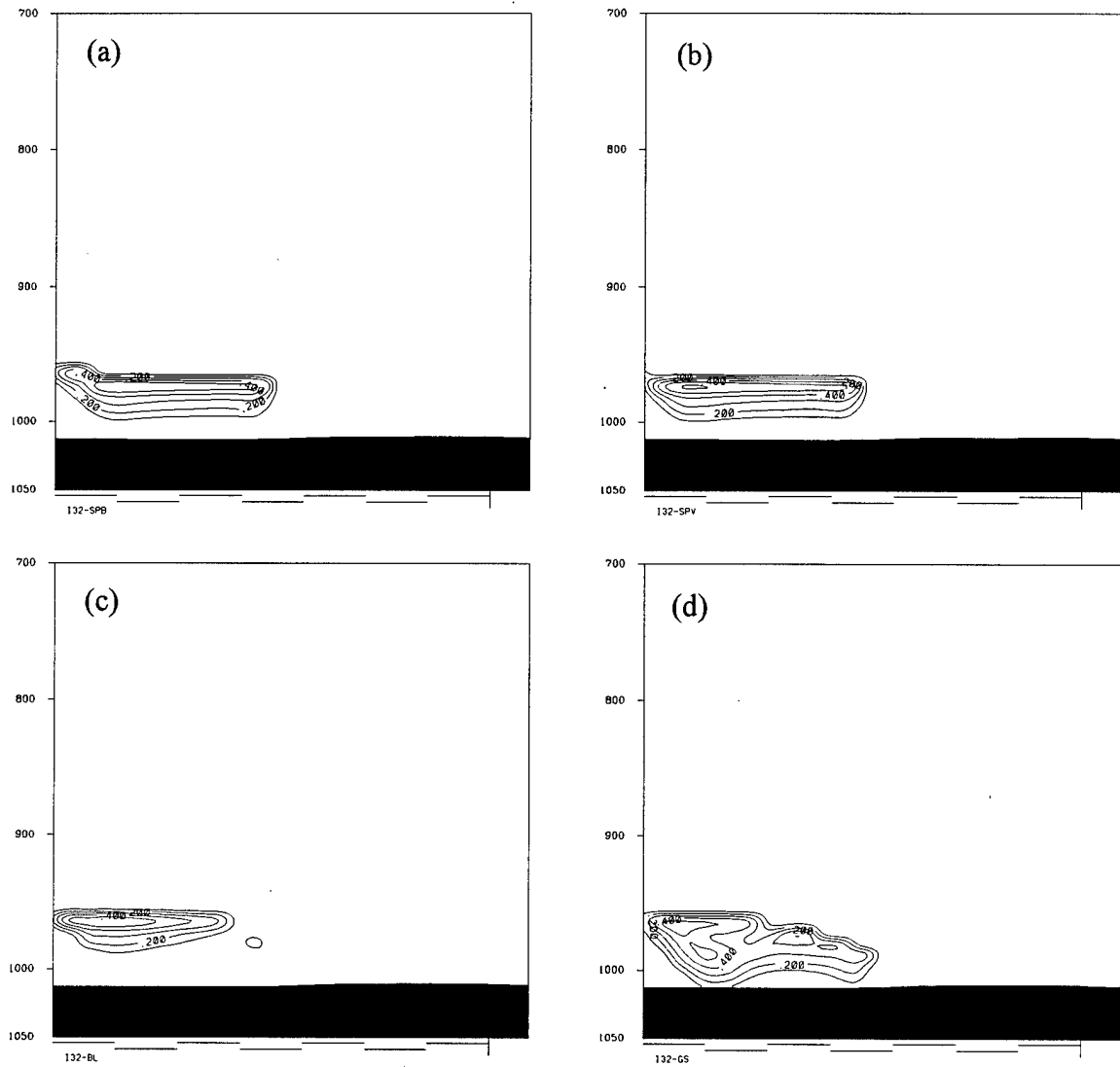


Figure 5.13. Vertical cross-section of cloud water (contour interval of  $0.1 \text{ g kg}^{-1}$ ) at 24 h (0000 UTC) along line segment O-L (Fig. 3.1), for (a) I32-SPB, (b) I32-SPV, (c) I32-BL, and (d) I32-GS.

the entrainment flux within the spectral model is a function of the jump of the model variable across the top of the boundary layer (i.e., the difference between the model variable within and above the PBL). As vertical resolution decreases, the depth over which the jump is computed increases, thus reducing the gradient. This results in reduced mixing down of warm, dry air from above the PBL, creating cooler PBL temperatures. Ayotte et al. (1996) found a similar difficulty among six prototypical PBL models after evaluation against large-eddy simulation results.

Soundings over water produced by the four 32-layer experiments at 24 h (not shown) show very little difference from the 55-layer experiments (Fig. 5.10). However, soundings over land (Fig. 5.14) produced by Exps. I32-SPB and I32-SPV at 24 h have mixed layers that are 1-2 °C cooler than those produced by the spectral model using 55 layers (Fig. 5.11). Experiments I32-SPB and I32-SPV also produce significantly more moisture within the boundary layer, by as much as  $1.5 \text{ g kg}^{-1}$ , compared to I55-SPB and I55-SPV. Experiment I32-BL has a boundary layer that is nearly 1 °C warmer than that of I55-BL, while the land-based sounding produced by I32-GS shows little impact of the reduced resolution, and still produces the super-adiabatic surface layer seen in the 55-layer experiment.

The most notable impact of reduced vertical resolution is seen in the cross sections of all four 32-layer experiments, however. The vertical gradients at the inversion base are smaller in the 32-layer experiments than the 55-layer experiments. Again, in the spectral

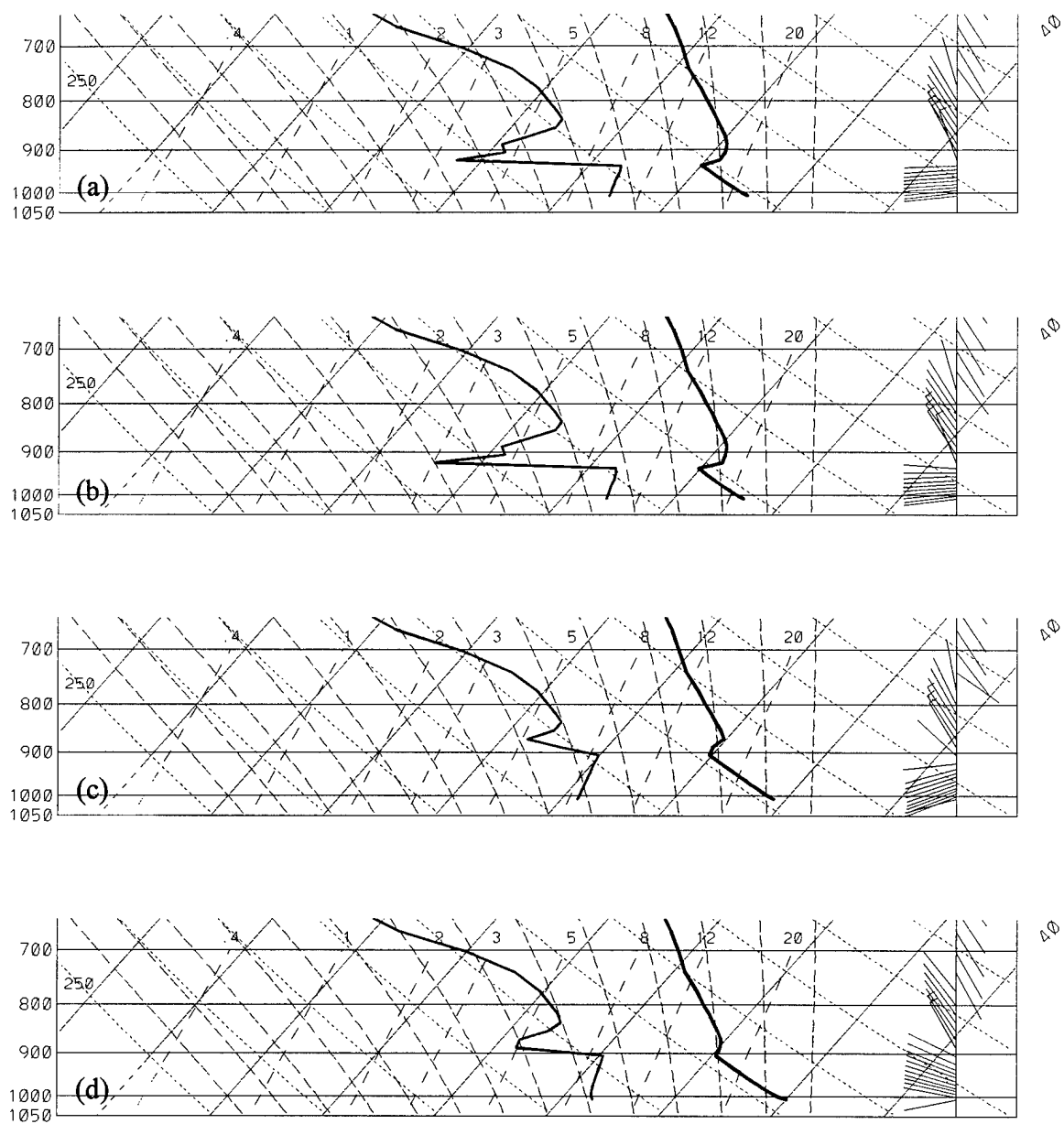


Figure 5.14. Temperature, moisture, and wind profiles for point "Land" (Fig. 3.1) at 24 h (0000 UTC) for (a) I32-SPB, (b) I32-SPV, (c) I32-BL, and (d) I32-GS.



model, weaker gradients and a smaller jump generate a weaker entrainment flux of warmer, dryer air into the boundary layer. Also, higher vertical resolution results in smaller grid volumes that are easier to saturate, more readily allowing the development of cloud or fog, which then has an impact on both longwave and shortwave radiation. This affects the temperature and moisture profiles and fluxes, which, in turn, have an impact on the depth of the PBL, and therefore, the depth over which the PBL scheme operates. Thus, it is clear that the effect of gridspace resolution on non-PBL physics still exists regardless of the choice of PBL scheme and this most certainly influences the results of the PBL scheme. It is not clear whether the differences between the spectral experiments and the "high-resolution" experiments are due to the choice of closure, or are the result of the spectral architecture.

Because "high-resolution" PBL schemes can account for 30 or 40 percent of total model computation time, efficiency of these parameterizations is of critical concern. Figure 5.15 compares the total MM5 computation time for each experiment normalized by the model run with the greatest total computation time. Since I55-SPB and I55-SPV reduce *total* computation time by about 25 percent as compared to I55-BL, the spectral model is *several times* faster than the Blackadar or Gayno-Seaman PBL models in MM5.

## 5.2 ARM-CART Case

It is clear from the results of the idealized coastal-zone case that reducing vertical grid-space resolution enhances the differences among the PBL models. Additionally,

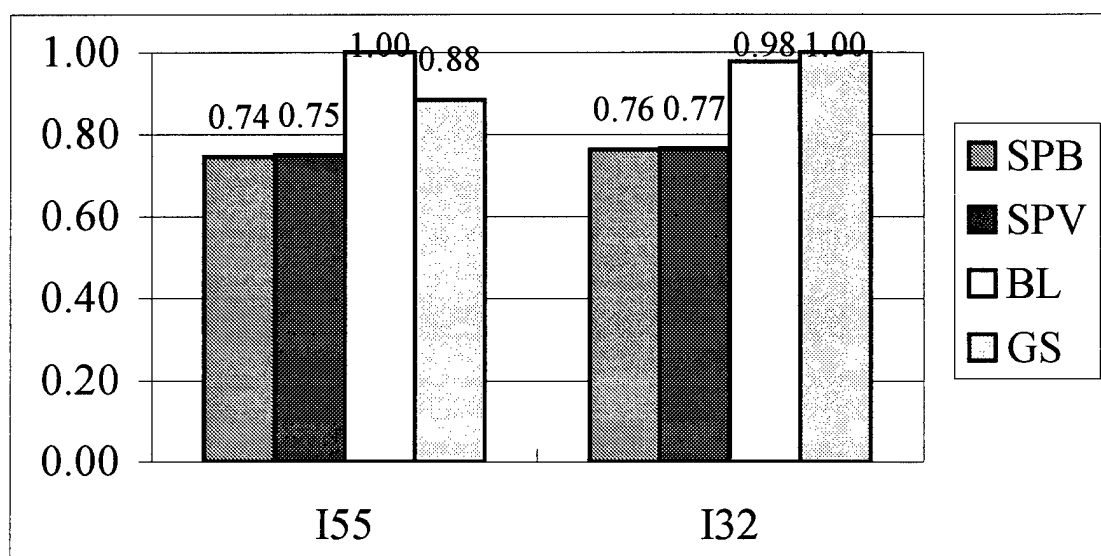


Figure 5.15. Normalized total MM5 computation time for idealized-case experiments.

although each of the idealized-case experiments produced reasonable results, it cannot be determined which is most accurate. Therefore, to better understand the differences among the PBL models, this investigation uses a real-data case and proceeds with 32 vertical model layers (Table 3.1). The choice of 32 vertical layers is somewhat more typical than 55 layers for current operational mesoscale models (e.g., Mass and Kuo 1998), and is certainly more practical for large domains. In this section the results of the MM5 with the spectral PBL model (Exps. SPB and SPV) are compared to the MM5 simulations using the Blackadar (Exp. BL) and Gayno-Seaman PBL (Exp. GS) models. In order to determine which of the models produces the most realistic results, the model output of all four experiments is verified against the special data from the ARM-CART (AC) site central facility CF and four boundary facilities B1, B4, B5, and B6 (see Fig. 3.3).

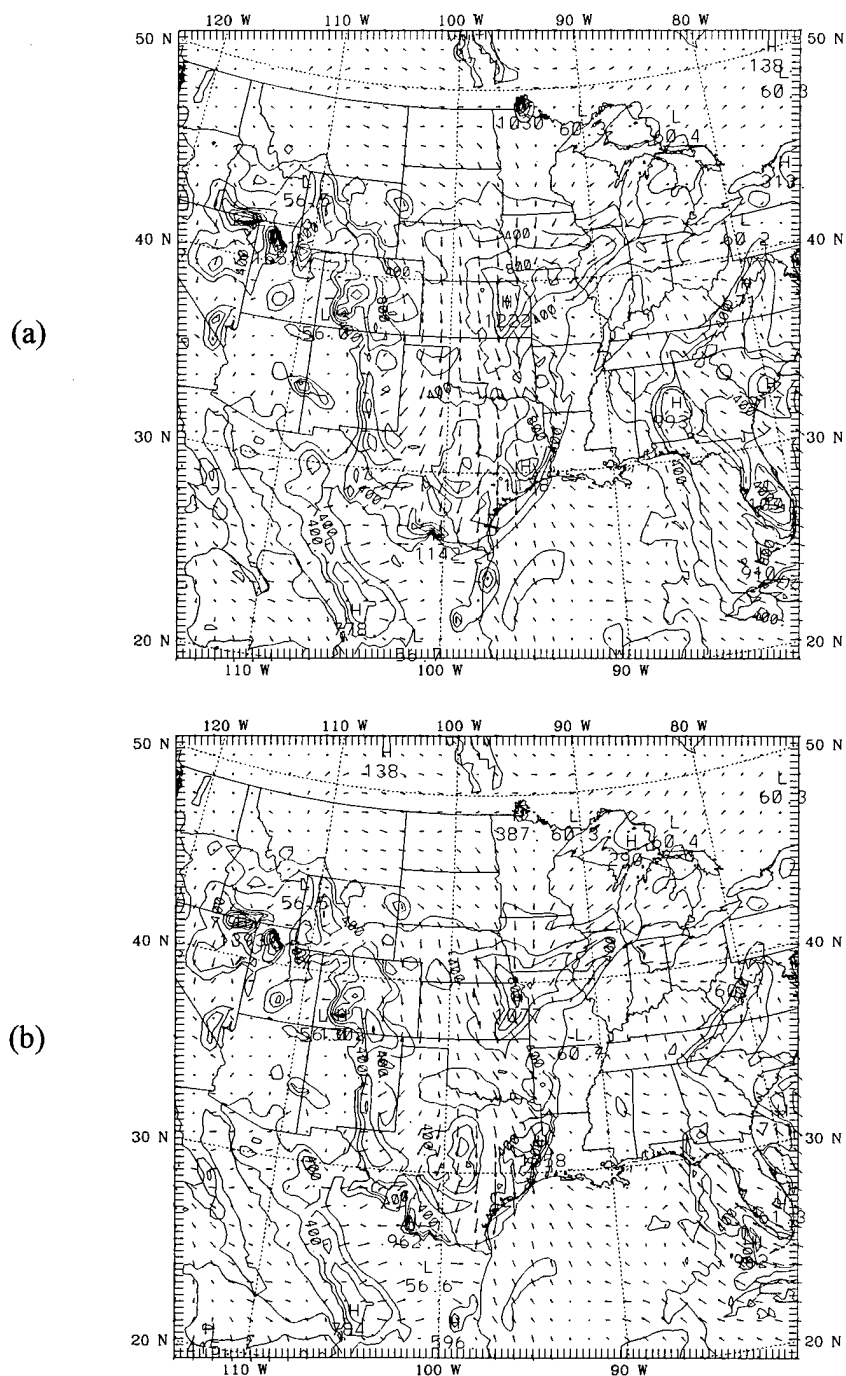
It should be emphasized that the two spectral experiments differ only by the technique used to diagnose the depth of the PBL at all grid-points at the initial time and at those grid-points experiencing deep moist convection during the simulation. The spectral model uses a prognostic equation for PBL depth at all other times. Since there is no deep convection within the AC site during this case, all differences between SPB and SPV results are attributed to sensitivity to the initial conditions for PBL depth, and some smaller effect of horizontal advection from grid-points which have experienced convection.

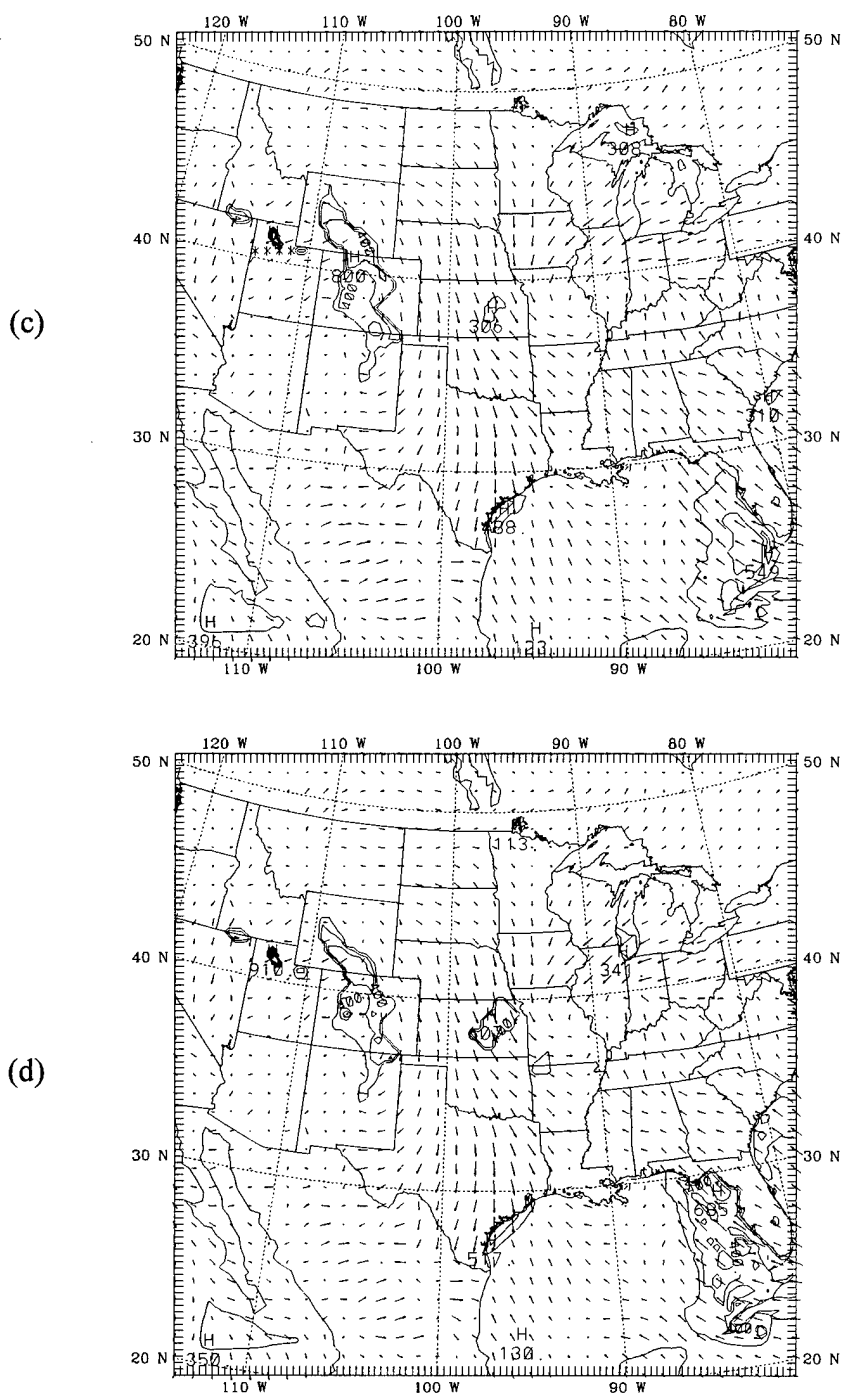
This section begins by demonstrating that each model experiment produces a reasonable synoptic-scale setting for this boundary-layer study. An intercomparison and

verification of various model variables is presented for the 48-h period described in Chapter 4. Some of these time series are shown exclusively at the AC CF, because it is more heavily instrumented than other facilities in the AC site. When possible, the model-simulated and observed trends are averaged over all five facilities to better represent the *mean* mesoscale signal for the verification. In addition, some model fields are examined in further detail by studying the trends at the individual facilities using vertical profiles, time-series of other atmospheric variables affecting model results, and budgets showing individual terms in the surface energy balance (Eq. 2.2) and the spectral models' prognostic equation for PBL depth (Eq. 2.36). The experimental results are summarized using verification statistics and an ordinal ranking based on the 48-h mean statistics. However, the statistical significance of the differences among the experiments is not well known. Finally, a comparison of model computational efficiency is presented.

At the initial time, 0000 UTC, 12 April 1997, the AC site is dominated by northwesterly flow at the surface with overcast skies behind a cold front that extends from southeastern Missouri to southern Texas (Fig 4.2 a). High pressure moves into the AC site and skies clear through the night on the second day.

This synoptic pattern is evident in Fig. 5.16, model-predicted PBL depth at 4 h (0400 UTC, 12 April 1997), for all four experiments. The post-frontal northwesterly flow is evident in all four experiments, with Exps. SPB and SPV producing deeper PBL depths and stronger horizontal gradients than Exps. BL and GS in the vicinity of the cold front near the Texas coast. Shallower PBL depths in regions ahead of the front are associated





with the frontal precipitation (not shown). Experiments BL and GS diagnose PBL depths to be at the surface over much of the domain during this stable nocturnal period. All four experiments produce an area of elevated PBL depths (300-1200 m) within the AC site behind the cold front.

Figure 5.17 compares the trend of surface pressure at the AC central facility (CF) (Fig. 3.3) to the pressure trends produced in each experiment at that location. As expected, both observed and simulated surface pressures increase over the 48-h period in all experiments. All of the models compare well to the observed surface pressure until the last 6 h of the forecast period when model surface pressures are 2-5 mb higher than observed. These pressure errors will be shown to be related to under-predicted afternoon temperatures on the second day.

Surface observations at Ponca City, OK, 25 miles northeast of the CF, indicate low ceilings (1600-4300 feet AGL) lasting through the first 24 h, with skies clearing by 0400 UTC, 13 April 1997 (Fig. 5.18). Scattered cumulus and cirrus re-appear by 1500 UTC, 13 April 1997 and persist through 0000 UTC, 14 April 1997. A comparison of model column-integrated cloud water with hourly averaged values measured at the CF (Fig. 5.18) shows that only the spectral experiments (SPB and SPV) produce more cloud on the first day than the second, as observed. Furthermore, the SPB experiment correctly produces two periods of enhanced cloudiness on the first day although it is 3 hours late in the forecast of the first maximum. All four models indicate the development of clouds

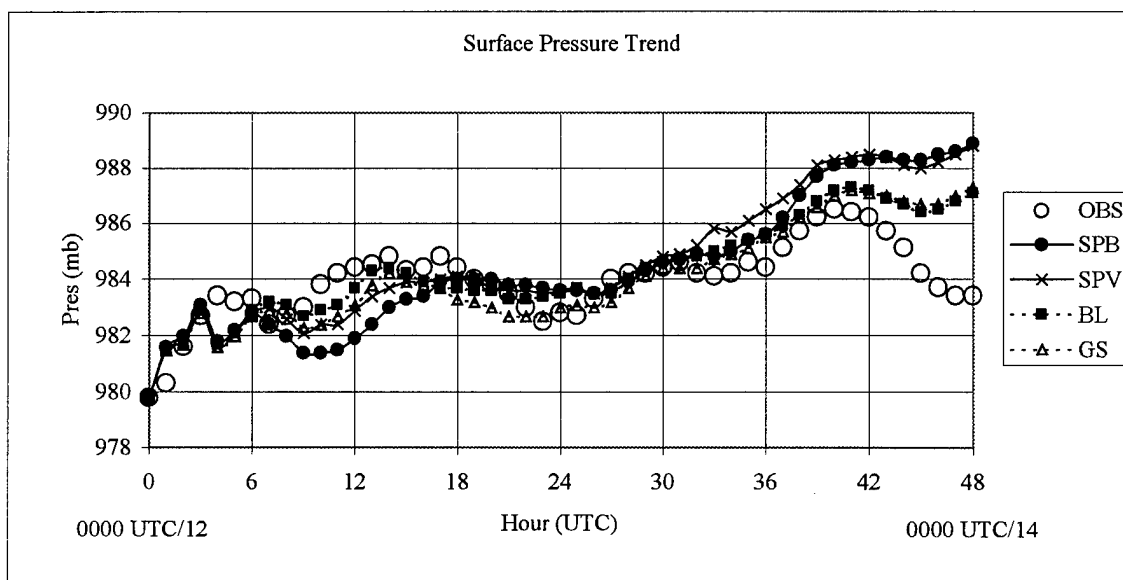


Figure 5.17. Time-series analysis valid 0000 UTC 12 April 1997 to 0000 UTC 14 April 1997 comparing hourly observed and model-predicted surface pressure at CF.



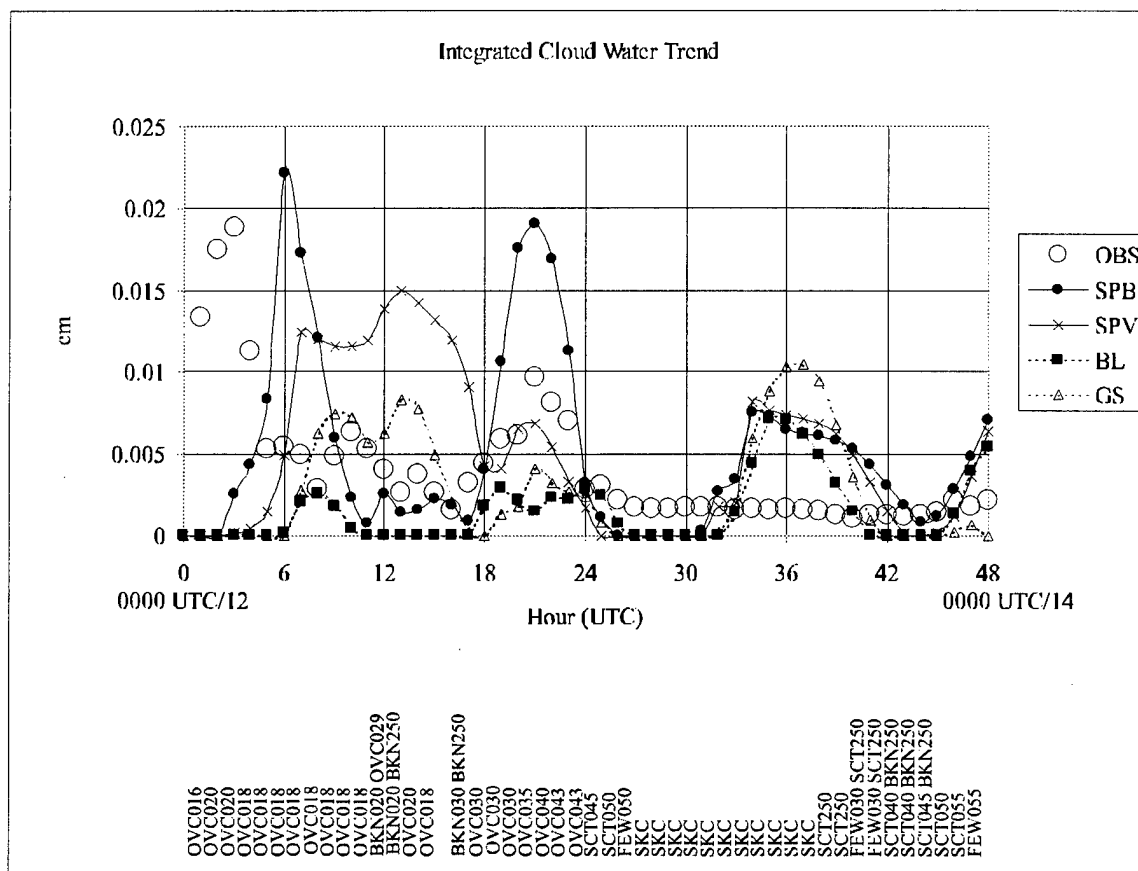


Figure 5.18. Time-series analysis, valid 0000 UTC 12 April 1997 to 0000 UTC 14 April 1997, comparing hourly observed total column liquid water measured by microwave radiometer, and model-predicted integrated cloud water for the CF. The bottom of the figure shows hourly observed sky condition at Ponca City, OK, 25 miles northeast of the CF.

too early, between 0900 and 1500 UTC, on 13 April 1997, when none is observed. Cloud is observed after 1500 UTC (Fig 5.18) but it is under-predicted by all experiments except perhaps SPB.

Low-level observed and predicted winds behind the cold front on the first day are fairly strong, averaging  $8\text{--}10\text{ m s}^{-1}$  over the five facilities (Fig. 5.19). As high pressure moves in on day two, however, the winds diminish considerably, to average around  $4\text{--}5\text{ m s}^{-1}$ . All experiments demonstrate this trend, and over-predict wind speeds for the 48-h period by  $0.3\text{--}1.7\text{ m s}^{-1}$  (Table 5.1).

Figure 5.20 displays the five-facility average temperature at the lowest model layer (approx. 30 m) through the 48-h period. The BL and GS simulations compare favorably with the observed 30-m temperature through the diurnal minimum of the second day (36-h forecast, valid 1200 UTC, 13 April 1997), but lag daytime temperatures on 13 April 1997 by  $2\text{--}5\text{ }^{\circ}\text{C}$ . The SPB and SPV experiments, on the other hand, have weaker diurnal cycles: both experiments begin warming several hours before the observed minimum temperature is reached on the first night (11-h forecast, valid 1400 UTC, 12 April 1997), are  $2\text{ }^{\circ}\text{C}$  too cool at the first diurnal maximum, (23-h forecast, valid 23 UTC, 12 April 1997), and more than  $7\text{ }^{\circ}\text{C}$  too cool at 44 h (2000 UTC, 13 April 1997). For the 2-day period, mean errors range from  $-1.0\text{ }^{\circ}$  to  $-1.7\text{ }^{\circ}\text{C}$  (Table 5.1) for the four experiments.

At the 900-mb level (Fig. 5.21a), similar results are found. All experiments verify well through the first night, but are too cool later in the forecast period, with the SPB and

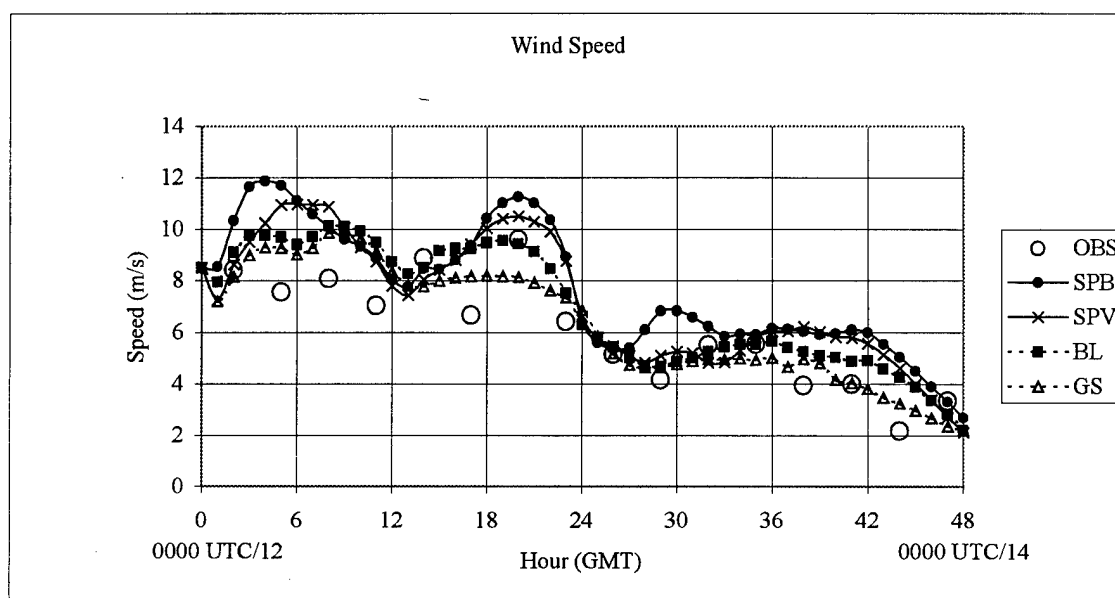


Figure 5.19. Time-series analysis, valid 0000 UTC 12 April 1997 to 0000 UTC 14 April 1997, comparing the five-facility average three-hourly observed and hourly model-predicted surface layer (30 m) wind speed.

Five-Facility Average	MEAN ERROR				MEAN ABS ERROR				RMS ERROR			
	SPB	SPV	BL	GS	SPB	SPV	BL	GS	SPB	SPV	BL	GS
Sfc Layer Wnd Spd	1.7	1.2	0.9	0.3	2.7	2.4	2.1	1.8	3.2	2.9	2.6	2.4
Sfc Layer Wnd Dir	7	5	4	4	22	22	22	23	32	31	32	33
Sfc Layer Temp.	-1.6	-1.7	-1.1	-1.0	2.3	2.3	1.8	1.9	3.2	3.2	2.6	2.6
Sfc Layer Spec. Hum.	-0.1	-0.1	-0.1	0.0	0.3	0.3	0.3	0.3	0.5	0.5	0.4	0.4

Five-Facility Average	MEAN ERROR				MEAN ABS ERROR				RMS ERROR			
	SPB	SPV	BL	GS	SPB	SPV	BL	GS	SPB	SPV	BL	GS
900mb Temperature	-1.4	-1.5	-0.5	-0.3	2.0	2.0	1.2	1.2	2.5	2.4	1.6	1.6
800mb Temperature	-1.0	-1.0	-0.8	-0.6	1.9	1.8	1.6	1.6	2.2	2.2	2.0	2.0
700mb Temperature	-2.2	-2.1	-1.8	-1.7	2.3	2.2	1.9	1.9	2.7	2.7	2.4	2.3
900mb Spec. Humidity	0.1	0.1	0.1	0.0	0.4	0.3	0.3	0.4	0.5	0.5	0.4	0.5
800mb Spec. Humidity	0.0	0.0	0.1	0.1	0.4	0.4	0.4	0.4	0.5	0.5	0.5	0.5
700mb Spec. Humidity	-0.1	-0.1	-0.1	0.0	0.4	0.4	0.4	0.5	0.6	0.6	0.6	0.6

Central Facility Rank	MEAN ERROR				MEAN ABS ERROR				RMS ERROR			
	SPB	SPV	BL	GS	SPB	SPV	BL	GS	SPB	SPV	BL	GS
Surface Pressure	0.5	0.7	0.4	0.2	1.4	1.3	0.8	0.9	1.9	1.8	1.1	1.2
Surface Rel. Hum.	0.09	0.10	0.05	0.08	0.11	0.11	0.06	0.08	0.12	0.12	0.07	0.10
Net Radiation	-55	-50	3	-9	71	64	67	59	109	97	88	92
Sensible Heat Flux	-32	-26	-9	-12	43	41	37	40	61	59	51	61
Latent Heat Flux	-20	-18	-1	-7	26	22	16	19	39	35	25	31
Int. Cloud Water	0.001	0.001	-0.003	-0.001	0.005	0.005	0.004	0.004	0.006	0.007	0.006	0.006

Five-Facility Average	MEAN ERROR				MEAN ABS ERROR				RMS ERROR			
	SPB	SPV	BL	GS	SPB	SPV	BL	GS	SPB	SPV	BL	GS
0 to 48-h PBL Depth	-78	-118	-392	-376	361	365	458	444	443	456	612	578
Nighttime PBL	29	11	-169	-205	135	162	198	205	226	269	352	371
Daytime PBL	-68	-100	-142	-147	133	173	204	202	239	305	383	368

Table 5.1. ARM-CART case experimental error statistics.

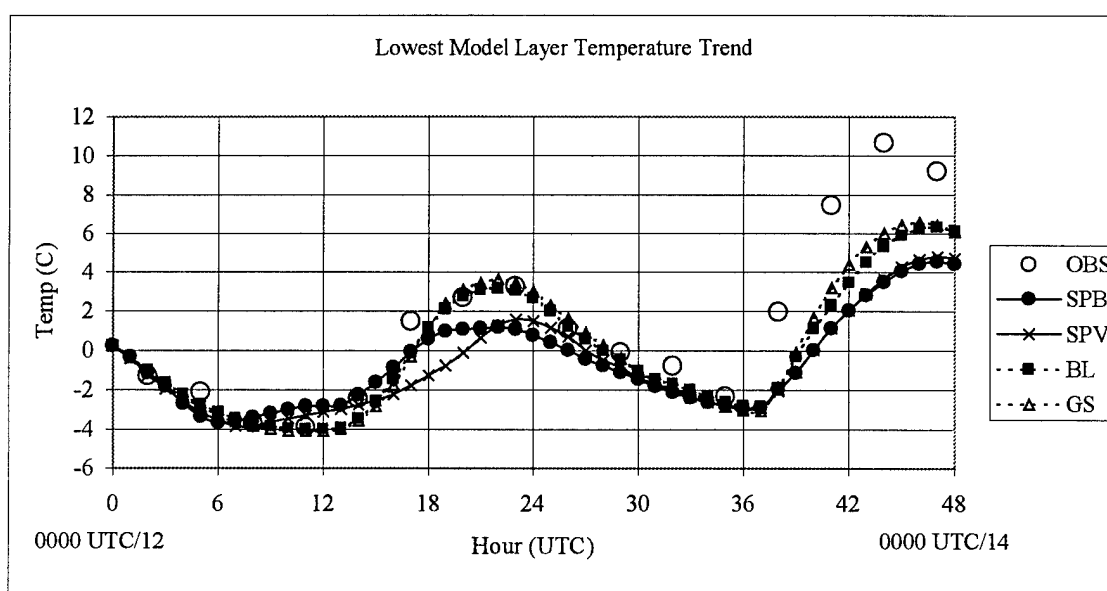


Figure 5.20. Time series analysis, valid 0000 UTC 12 April 1997 to 0000 UTC 14 April 1997, comparing the five-facility average three-hourly observed and hourly model-predicted surface layer (30 m) temperature.

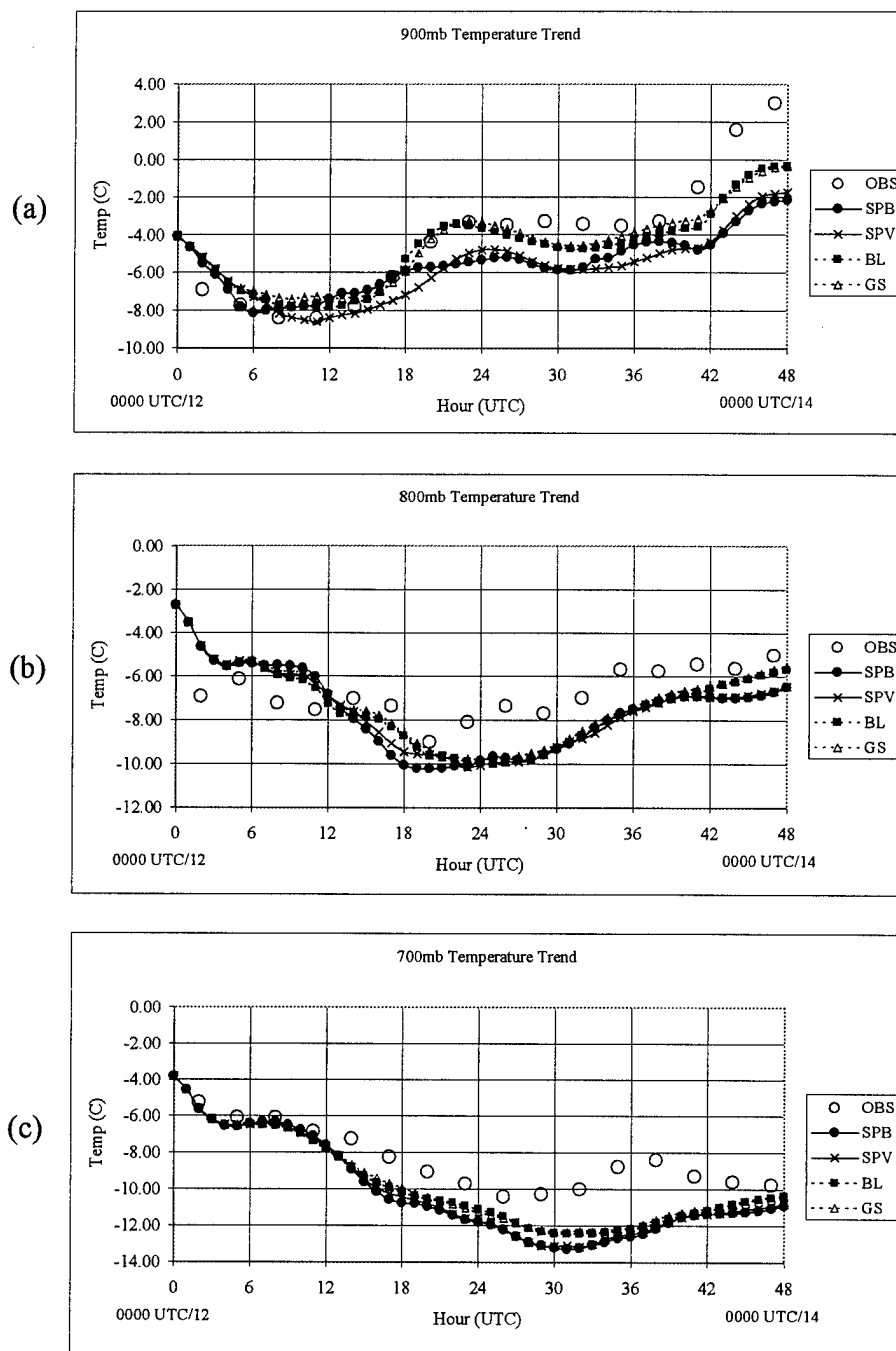


Figure 5.21. Time-series analysis, valid 0000 UTC 12 April 1997 to 0000 UTC 14 April 1997, comparing the five-facility average three-hourly observed and hourly model-predicted temperature at (a) 900 mb, (b) 800 mb, and (c) 700 mb.

SPV experiments almost 3 °C cooler than the diurnal maximum the first afternoon, and all experiments too cool through the second 24 hours. The 800-mb and 700-mb (Fig. 5.21b-c) temperature trends show very good agreement among the experiments, as expected, demonstrating that the choice of PBL scheme has little effect above the boundary layer, which remained below 2000 m. However, during the second day, all of the 800-mb temperature trend-lines show a 1-2 °C cool bias. A cool bias of 1-3 °C is also present at 700 mb between 12 and 48 h. Examination of observed and forecast trends of specific humidity (not shown) indicates very strong agreement among all experiments at the surface, 900, 800, and 700 mb. These experiments also verify well against the observed values at each level, as shown in Table 5.1.

The errors in the aforementioned time-series analyses will of course impact the depth of the boundary layer. For example, if model-generated surface-layer temperatures are cooler than observed one might expect the model boundary layer to be shallower than observed due to reduced surface heating. If the air *above the PBL* (e.g., 800, 700 mb) is cooler than observed, entrainment effects would produce cooler mean temperatures through a deeper PBL. If low-level winds are forecasted to be stronger than observed, the model PBL may be too deep at night as a result of increased mechanical mixing. Wind errors also affect the depth of the PBL through horizontal advection (Eq. 2.36). Therefore, all of these factors can contribute to the errors within the model PBL in this real-data case.

Another issue to be resolved involves how to best define the PBL height. Several techniques are tested here to diagnose the depth of the observed PBL using the standard

atmospheric sounding data at the CF. The first technique applied is purely subjective, based on experience using lapse rates and wind shear to determine the PBL depth. These values are shown as open circles in Fig. 5.22 and are labeled as subjective. The objective diagnosis techniques include the Bulk-Richardson (B-R) technique and the virtual potential temperature techniques described in Section 2.3, and an algorithm identical to the virtual potential temperature method, but instead using potential temperature. Figure 5.22 shows that, of the three objective diagnosis algorithms, the B-R method of Vogelezang and Holtslag (1996) appears to agree best with the subjective analysis. It must be noted, however, that the B-R method cannot produce a PBL depth lower than that of the reference level, which is chosen to be 30 m in this case. In addition, of the objective techniques, the B-R method is perhaps the most meteorologically sound, since it takes into account both the thermal and wind profiles. Therefore, in the following figures which show observed PBL depth, the B-R method is used.

Figure 5.23 shows the five-facility mean PBL depth over the 48-h forecast period. The observed boundary layer maintains a depth of at least 600 m through the first nocturnal period, 0000-1200 UTC, 12 April 1997, which is more than 50 percent of the maximum depth the following afternoon. This relatively deep nocturnal boundary layer is also apparent in the solutions of SPB and SPV. Experiments SPB and SPV produce a boundary layer that is 200 m deeper than observed at 0800 UTC, 12 April 1997, while BL and GS produce, on average, a PBL depth that is more than 400 m shallower than observed. Each of the experiments produces reasonable values of PBL depth through



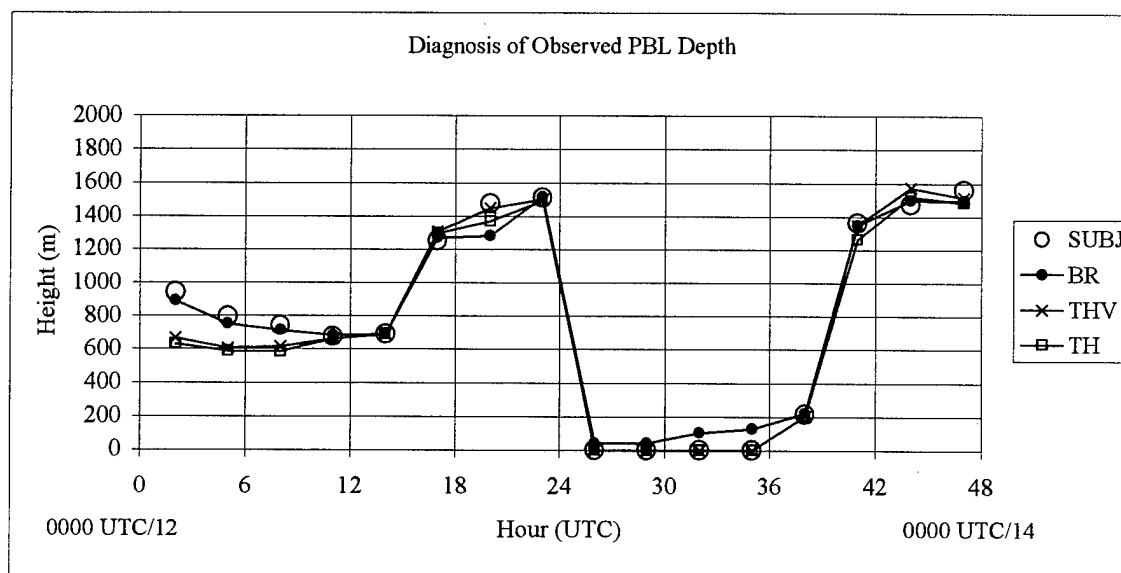


Figure 5.22. Time-series analysis, valid 0000 UTC 12 April 1997 to 0000 UTC 14 April 1997 of diagnosed PBL depth at the CF.

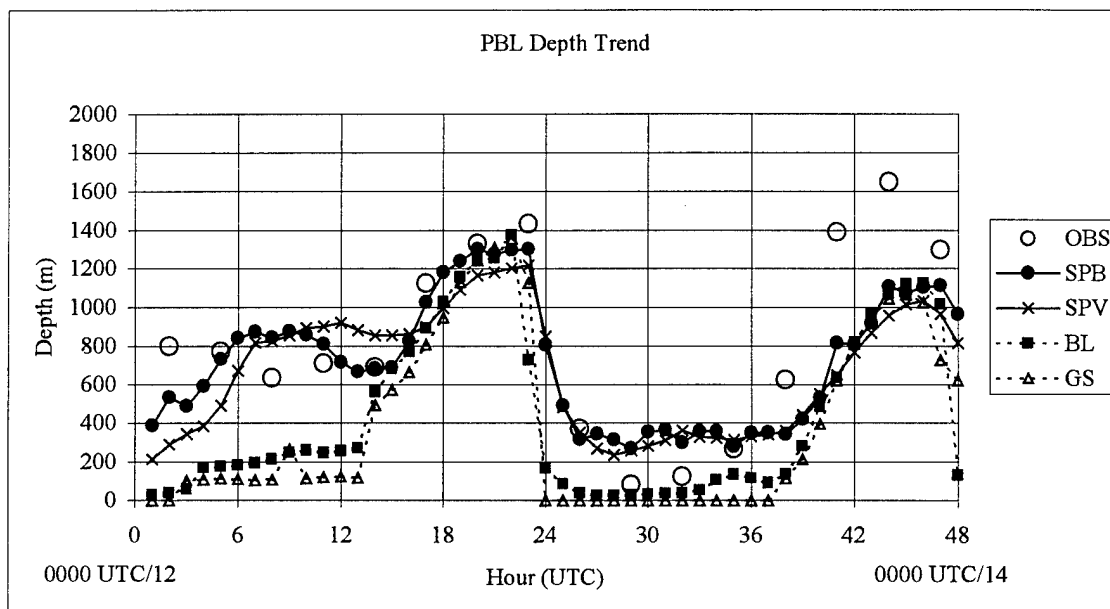


Figure 5.23. Time-series analysis, valid 0000 UTC 12 April 1997 to 0000 UTC 14 April 1997, comparing the five-facility average three-hourly observed and hourly model-predicted PBL depth.

the maximum at 2300 UTC, 12 April 1997. Experiments BL and GS reach their maximum values an hour earlier than SPB and SPV and the 3-hourly observation, and maximum depths are all within about 200 m of the observed depth. This is impressive, since the model vertical resolution near 1400 m is around 180 m (Table 3.3).

Through the second night, 0200 UTC 13 April 1997 to 1300 UTC 13 April 1997, the observed PBL depth decreases to around 100 m and begins rising gradually to more than 300 m by 1100 UTC 13 April 1997. Through this period, Exps. SPB and SPV maintain PBL depths between 300-400 m, while the five-facility average depths produced by BL and GS are less than 100 m and zero, respectively. All experiments underestimate the PBL growth through the final 12-h period of the model run, when mean surface-layer temperatures are under-predicted (Fig. 5.20).

In order to better understand some of the interesting features of the mean PBL depth trend described above, the next series of figures shows the 48-h time-series of PBL depth (Fig. 5.24) and lowest model layer temperature (Fig. 5.25) at facilities B1, B5, and CF. The first feature to be investigated is the simulated maximum in the nocturnal PBL depth in Fig. 5.23 for Exps. SPB and SPV between 0600-1200 UTC, 12 April 1997. This forecasted trend is most apparent at B1 (Fig. 5.24a), where this feature is also forecasted to a lesser degree by Exps. BL and GS, but it is not that apparent in the observed trend at B1. Note the variability in low-level temperature from site to site through this nocturnal period (Fig. 5.25) and the correlation between over- and under-prediction of temperature,

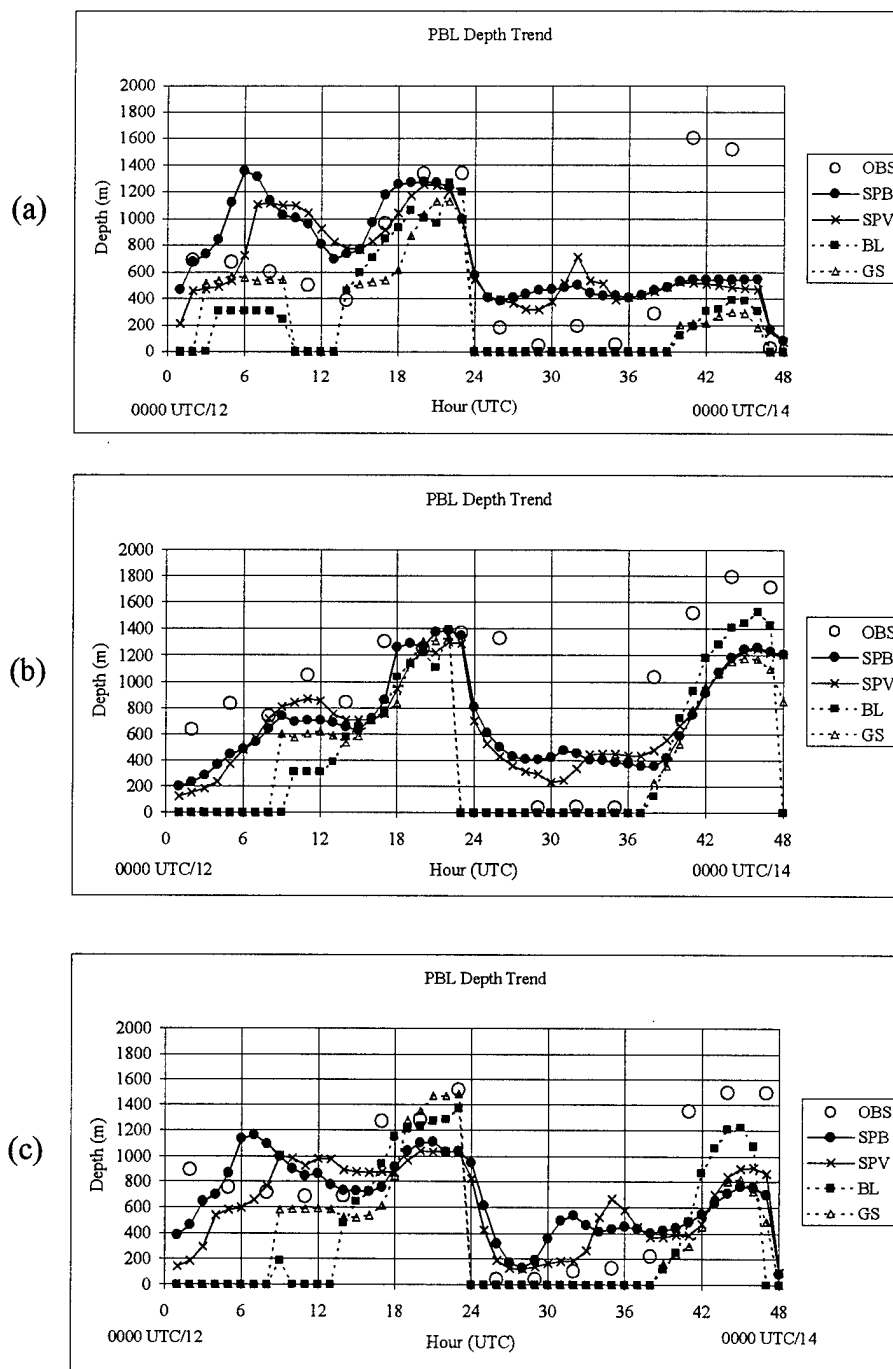


Figure 5.24. Time-series analysis, valid 0000 UTC 12 April 1997 to 0000 UTC 14 April 1997, comparing the three-hourly observed and hourly model-predicted PBL depth at facility (a) B1, (b) B5, and (c) CF.

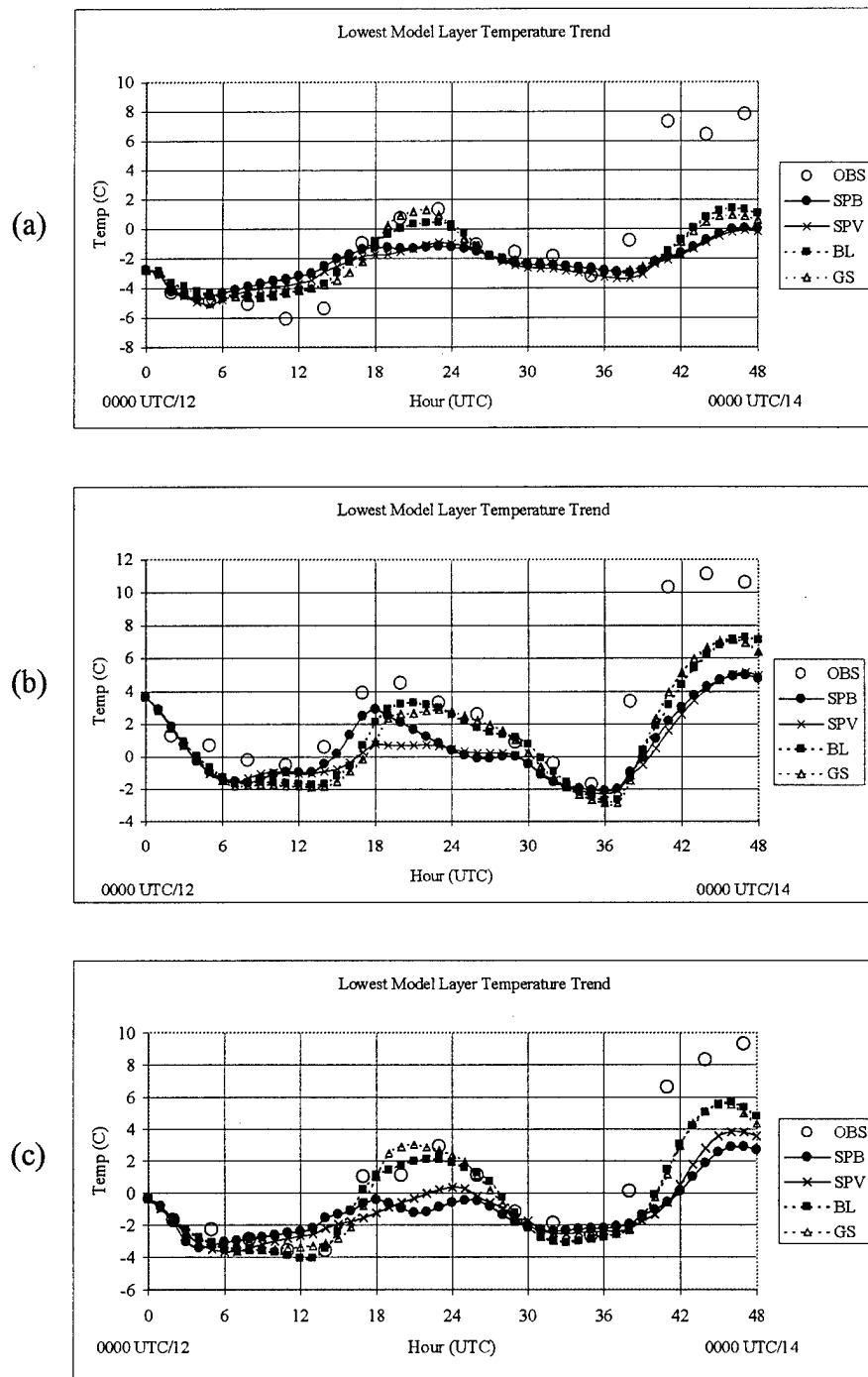


Figure 5.25. Time-series analysis, valid 0000 UTC 12 April 1997 to 0000 UTC 14 April 1997, comparing the three-hourly observed and hourly model-predicted surface-layer (30 m) temperature at facility (a) B1, (b) B5, and (c) CF.

and over- and under-prediction of PBL depth (Fig. 5.24).

Figure 5.26 shows skew-T diagrams at B1, valid at 0800 UTC, 12 April 1997, for the observed conditions and all four experiments. The observed sounding in Fig. 5.26a has a well-mixed temperature profile capped by an inversion at 600 m AGL that defines the PBL depth. This type of profile is produced by all the experiments with somewhat different stabilities below the inversion. As shown in Fig. 5.24a, the GS experiment most accurately determines the PBL depth at this time. Experiment BL diagnoses a depth 300 m lower than observed, because its boundary-layer thermal profile is slightly stable above the surface. Experiments SPB and SPV differ the most from the observed depth and those forecasted by the other two experiments, with depths 500 m greater than the actual depth.

Figures 5.26b and 5.26c show that both spectral experiments produce more stably stratified thermal profiles, yet still develop boundary layers far deeper than observed during this nocturnal period. It must be recalled that the spectral PBL scheme is not diagnosing the depth of the PBL; rather, it uses a prognostic equation to determine PBL height, which may deviate from a diagnosis based on the model mass and wind fields at a given time. In this case, however, the prognosis is apparently representing a real meteorological feature. Although the nocturnal PBL depth maximum is not seen in the observation at B1, it is present to the southeast at facility B5 (Fig. 5.24b) with a maximum depth of over 1000 m at 1100 UTC 12 April 1997. Figure 5.27a shows that the observed thermal profile at this time is dry adiabatic to 920 mb and approximately

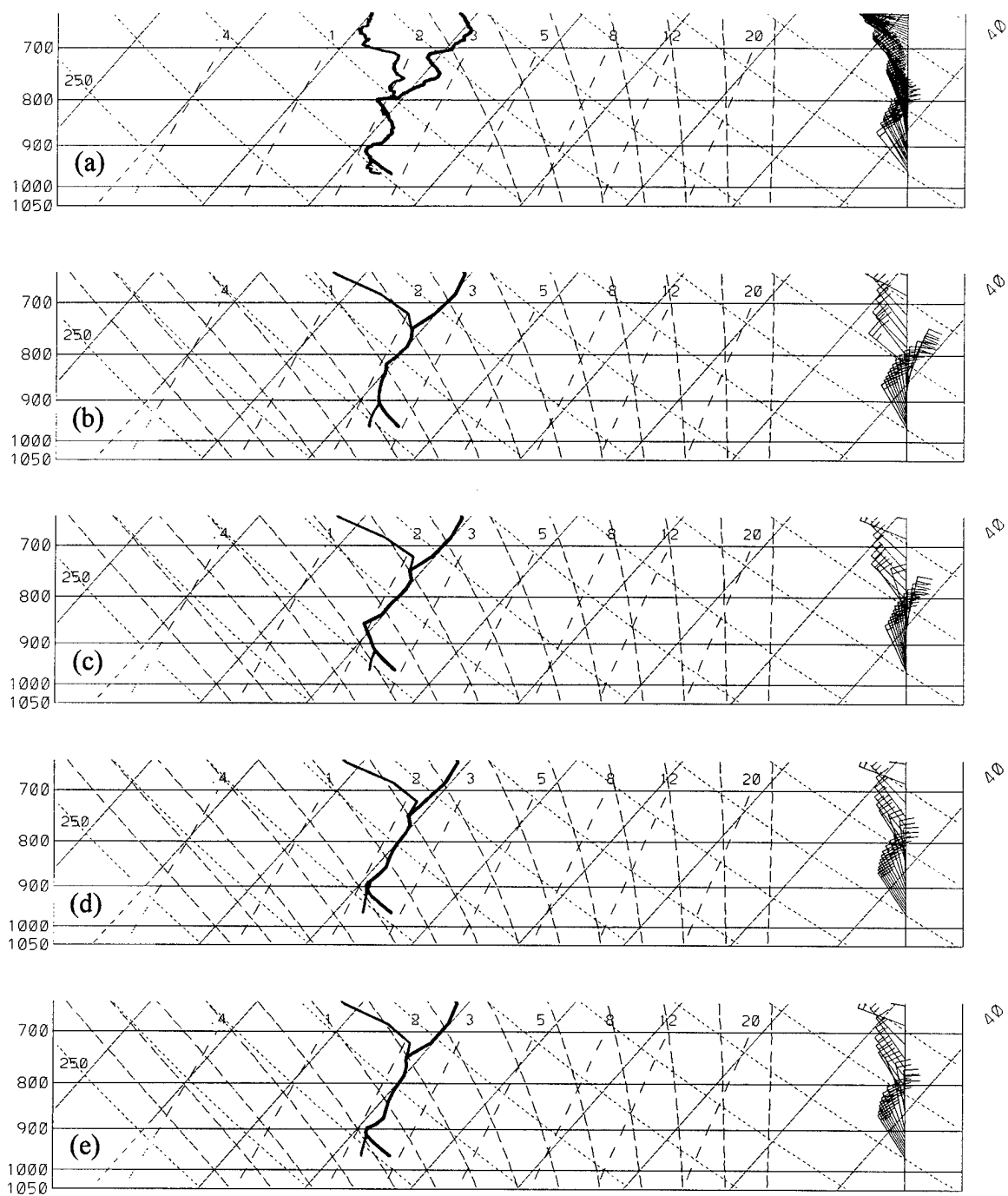


Figure 5.26. Temperature, moisture, and wind profiles valid at 8 h (0800 UTC, 12 April 1997) at facility B1 for (a) observation (b) SPB, (c) SPV, (d) BL, and (e) GS.

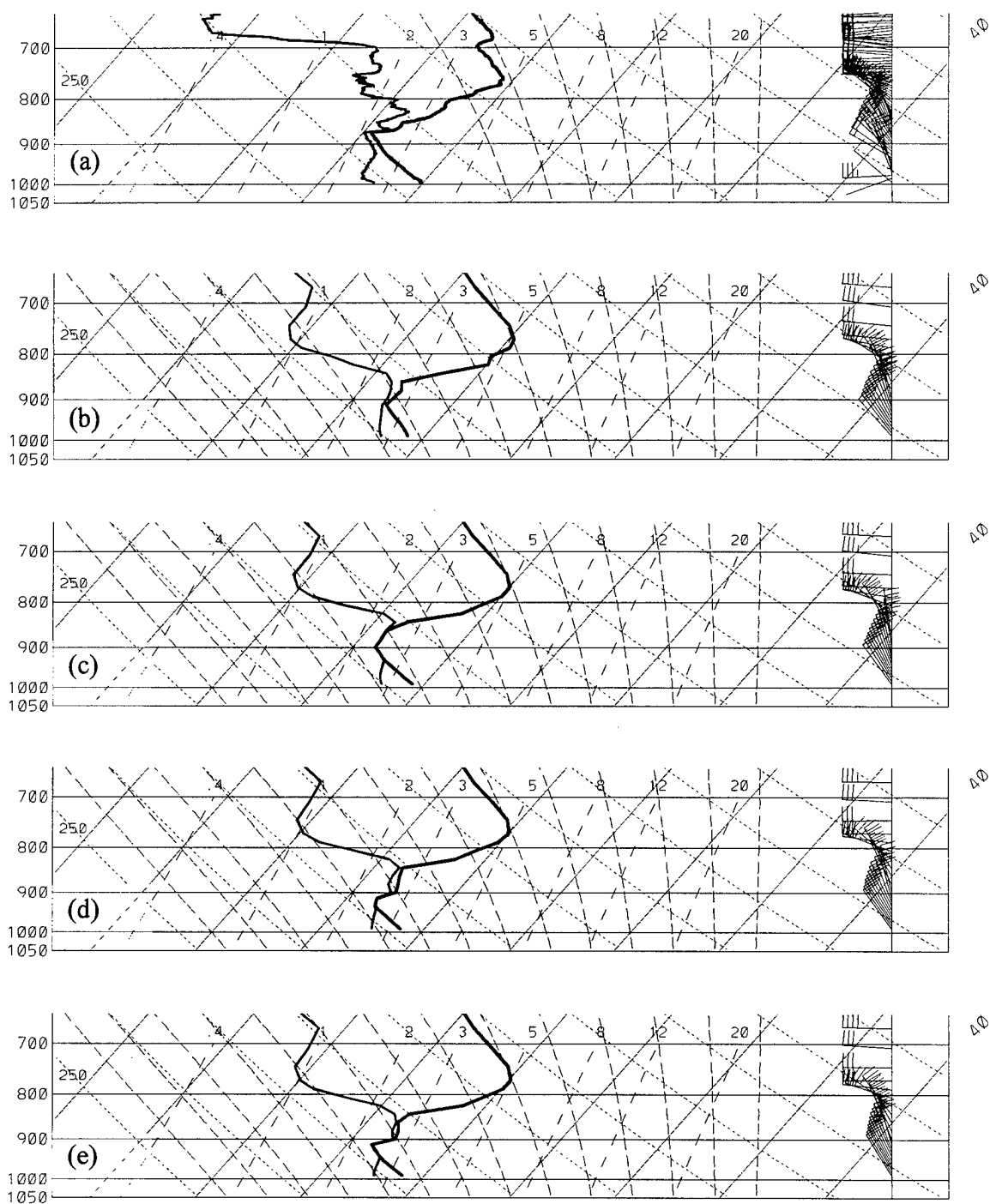


Figure 5.27. Temperature, moisture, and wind profiles valid at 11 h (1100 UTC, 12 April 1997) at facility B5 for (a) observation (b) SPB, (c) SPV, (d) BL, and (e) GS.



moist adiabatic to 870 mb. The wind profile shows strong directional shear through this layer. Again, the low-level lapse rates in Exps. SPB and SPV are less than adiabatic with SPV having a steeper lapse rate than SPB. Both of these experiments produce nocturnal PBL-depth maxima lower than that observed at B5 at 1100 UTC, 12 April 1997 (Fig. 5.24b), with SPV forecasting the best depth. Experiments BL (Fig. 5.27d) and GS (Fig. 5.27e) show an inversion base 750 m and 450 m shallower than the actual boundary layer, respectively. Therefore, during this nocturnal period, Exps. SPB and SPV produce a better forecast of PBL height than the other experiments.

Although it is also clear from Figs. 5.24 and 5.25 that all of the experiments significantly under-forecast the PBL depth and lowest model layer temperature during the second-day heating maximum, between 2000-2300 UTC 13 April 1997, it is most apparent at B1 (Fig. 5.24a). Examination of observed and model soundings at this location and time (Fig. 5.28) provide some insight into this problem. The observed temperature profile in Fig. 5.28a shows a very strong ( $4^{\circ}\text{C}$ ) and shallow (10 m), super-adiabatic layer which is not forecasted in any of the model experiments (Fig. 5.28b-e). Soundings at the other sites at this time (not shown) also show a super-adiabatic layer, although not as strong as that seen at B1. It is important to note that the observed sounding, with data reported nearly every 10 m, has much greater vertical resolution than the models used here. The lowest model layer in all experiments is 60 m deep, which limits even the GS TKE model's ability to produce super-adiabatic layers. But resolution is not the only reason for the large errors in the PBL depth and temperature during the

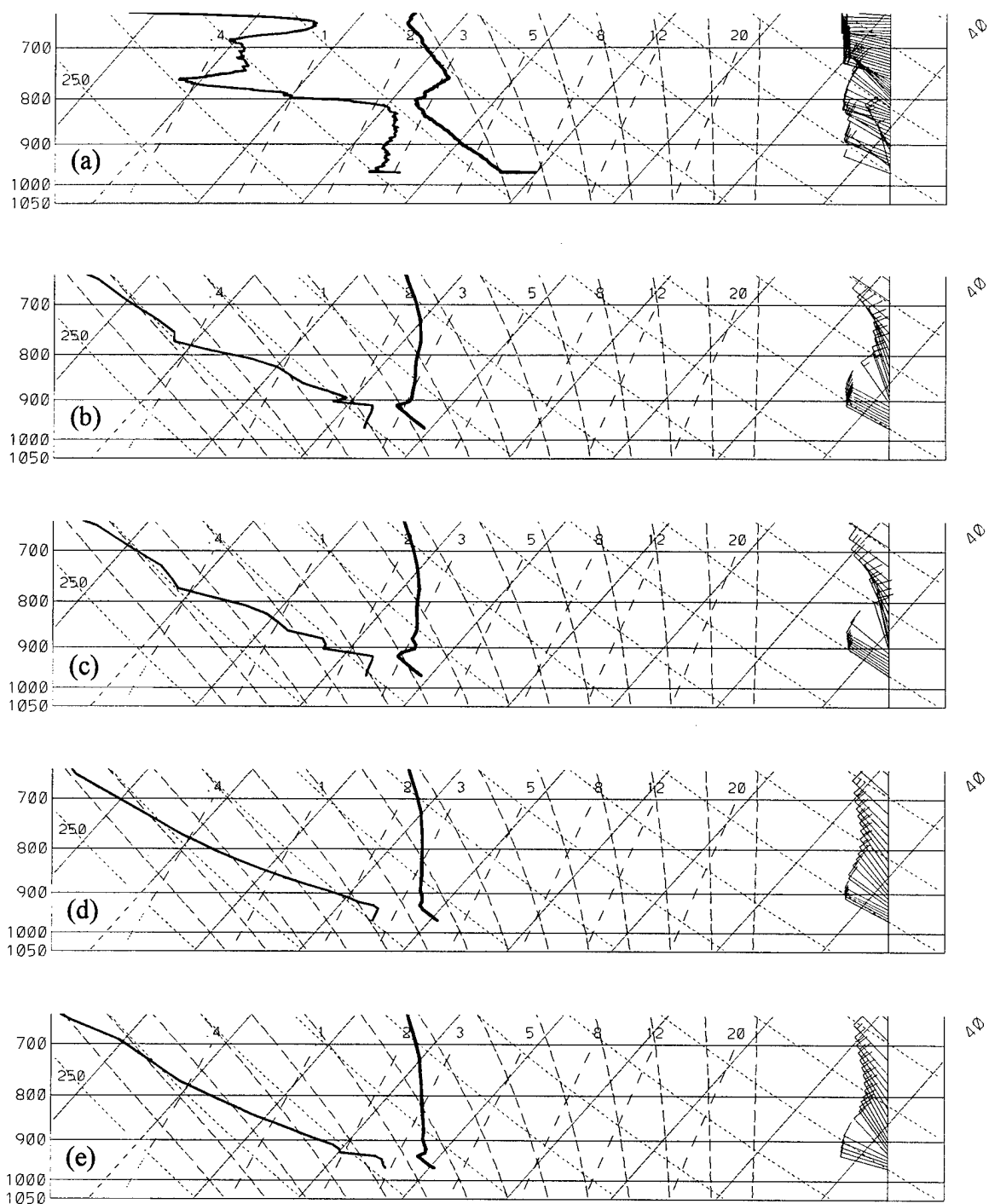


Figure 5.28. Temperature, moisture, and wind profiles valid at 44 h (2000 UTC, 13 April 1997) at facility B1 for (a) observation (b) SPB, (c) SPV, (d) BL, and (e) GS.

second day.

Because an understanding of the low-level temperature variation is crucial to an understanding of the PBL depth trend, here we examine the parameters governing the surface energy budget described in Eq. 2.2 and low-level temperature errors shown in Fig. 5.25c for the CF. Figure 5.29a shows that for net radiation at the surface, all experiments verify quite well during the nocturnal period on day two between 24-36 h. The diurnal maximum in net radiation at 43 h (1900 UTC 13 April 1997) shows SPB to under-forecast net radiation by about  $200 \text{ W m}^{-2}$ . This result is consistent with the integrated cloud water (Fig. 5.18) showing this experiment to produce somewhat higher amounts of cloud water at this time. More significantly, all four experiments lag the increase in net radiation prior to the second diurnal maximum. This delay, resulting from cloud produced by the models earlier than observed, significantly attenuates the time-integrated effect of net radiation (energy per unit area), resulting in delayed and/or reduced heat input at the surface, and thus under-predicted low-level temperatures. Note that the errors in the timing of SPV and SPB clouds and net radiation result in a mean bias of -50 to -55  $\text{W m}^{-2}$ , respectively for the 48-h period (Table 5.1), thus contributing to the larger -1.2 to -1.7  $^{\circ}\text{C}$  cool biases in low-level temperatures in the spectral model experiments. Figure 5.29 also shows that Exps. SPB, BL, and GS forecast the time of the first maximum of net radiation within 2 h, while over-forecasting the maximum magnitude by as much as  $300 \text{ W m}^{-2}$ . Experiment SPV underestimates the magnitude by

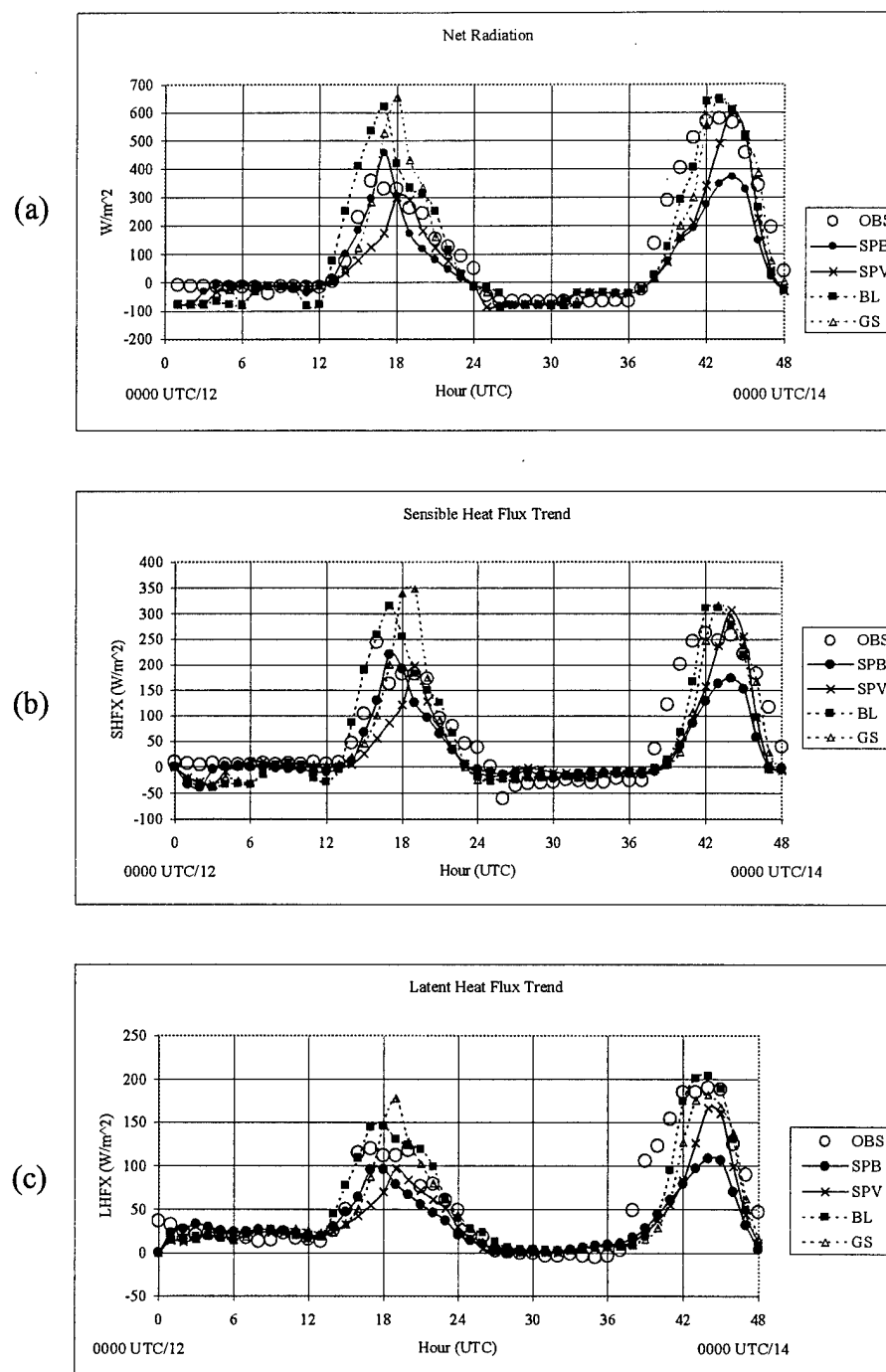


Figure 5.29. Time-series analysis, valid 0000 UTC 12 April 1997 to 0000 UTC 14 April 1997 comparing hourly observed and model-predicted (a) net radiation, (b) sensible heat flux, and (c) latent heat flux at the CF.

$50 \text{ W m}^{-2}$ , while delaying the maximum by 2 hours.

These radiative trends in Fig. 5.29a can be explained by again referring to Fig. 5.18, the integrated cloud water. It shows that Exp. SPV has cloud that persists almost until the time of maximum net radiation, reducing and delaying that maximum, while BL and GS have significantly less cloud water and proportionately greater and earlier net radiation maxima. Additionally, the second maximum of cloud water produced by SPB at 2100 UTC, 12 April 1997 corresponds to its earlier decrease of net radiation at that time. The 30-36-h forecast period, valid 0600-1200 UTC 13 April 1997 shows that all models have a slightly greater net radiation than observed. Again referring to Fig. 5.18, cloud is present in all experiments, increasing the back longwave radiation to the surface.

Figure 5.29b shows sensible heat flux and Fig. 5.29c displays latent heat flux at CF. Both of these figures reflect the patterns seen in the net radiation and model cloud. For example, the time of maximum net radiation corresponds to the time of maximum sensible and latent heat fluxes for each experiment. Thus, the cloud forecast greatly influences the net radiation, which influences ground temperature and the surface heat and moisture fluxes, which influence the PBL depth. It is interesting to note that the day-one PBL height (Fig 5.24c) and low-level temperature (Fig 5.25c) maxima at CF are well-predicted by BL and GS despite over-forecasts of net radiation and sensible and latent heat fluxes caused by under-forecasting cloud (Fig. 5.18). The errors tended to cancel in this case. For Exp. SPV on the other hand, the net radiation maximum at CF was under-predicted and delayed due to over-forecasting cloud. The sensible and latent

heat fluxes were also under-predicted and delayed, as were the low-level temperature maximum and PBL height. Therefore, model cloud and radiation physics greatly affect the performance of a given PBL model.

Again with the intent of better understanding the complexity of computing of the PBL depth trend, a study is made of the individual tendency terms in the prognostic equation (Eq. 2.36) for PBL depth used by the spectral model (only the terms from Exp. SPB are shown here). Figure 5.30 shows trends of the instantaneous values of these terms at 15-minute intervals over the 48-h forecast period at the CF. Comparing these curves to the PBL depth trend shown in Fig. 5.24c for SPB, it is possible to determine which terms (physical processes) make the largest contribution to the features discussed earlier in this section. The changes in PBL depth will be proportional to the sum of tendency terms.

It is apparent that the first nocturnal maximum in this experiment (7-h forecast, valid 0700 UTC, 12 April 1997) is generated by the combined effect of entrainment of warm air from above the boundary layer and horizontal advection of greater PBL depth into the CF. These two terms offset the negative effect of subsidence behind the cold front (i.e., downward environmental vertical velocity). Both of the rises in PBL depth prior to the afternoon maxima (17-20-h forecast, valid 1700-2000 UTC, 12 April 1997 and 40-45-h forecast, valid 1600-2100 UTC, 13 April 1997) must be attributed primarily to the entrainment term.

The sudden decrease of PBL depth after the first diurnal maximum (23-27-h forecast,

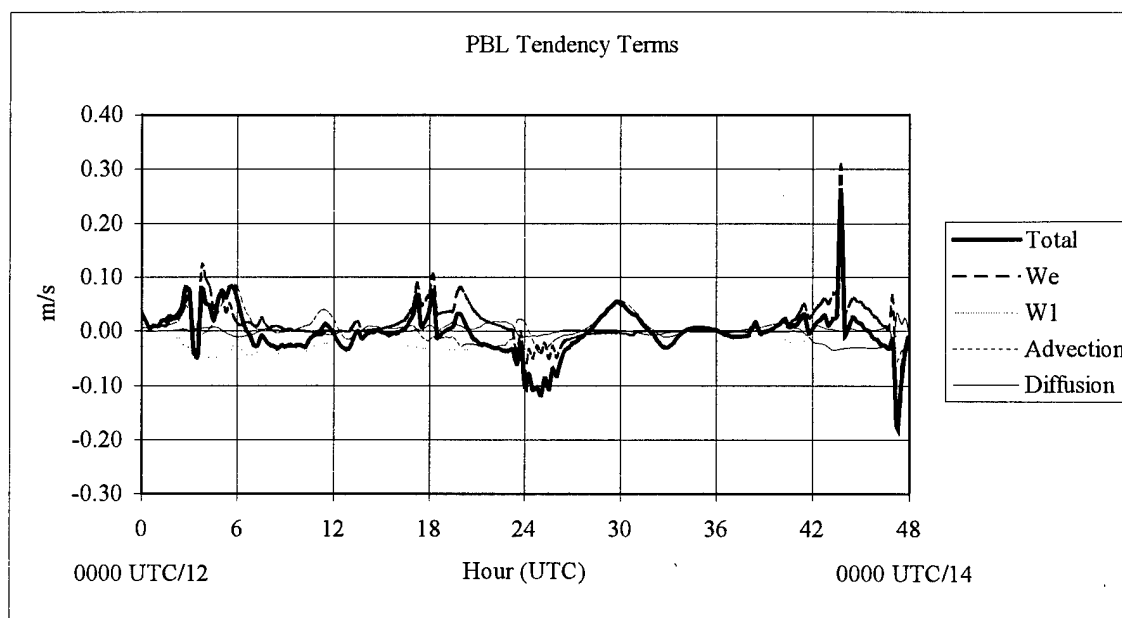


Figure 5.30. Time-series analysis, valid 0000 UTC 12 April 1997 to 0000 UTC 14 April 1997 comparing the relative contribution of the spectral model PBL tendency terms of Eq. 2.36 to the total PBL tendency for Exp. SPB at CF. Tendencies are plotted at 15-minute intervals.

valid 2300 UTC, 12 April 1997 - 0300 UTC, 13 April 1997) is the result of nearly equal contributions of negative environmental vertical velocity, entrainment, and horizontal advection. The decrease following the second diurnal maximum (47-48-h forecast, valid 2300 UTC, 13 April 1997 - 0000 UTC, 14 April 1997) is mainly due to entrainment. A nocturnal maximum appears at the CF during the second night (28-32-h forecast, valid 0400-0800 UTC, 13 April 1997) and an examination of Fig. 5.30 shows it to be solely the effect of horizontal advection of greater values of PBL depth into the grid-square.

Figure 5.31 is included to show the effect of the PBL height diagnosis within Exp. SPB at a point undergoing deep moist convection in southwest Louisiana, since no convection takes place within the AC site during this case. This figure shows the value of PBL depth at every time-step from the onset of convection until its cessation 40 minutes later. The figure demonstrates that the PBL depth continues to increase immediately following the onset of convection, then gradually falls to the minimum value allowed by the scheme, the height of the lowest full model layer (60 m), for the remainder of the convective period. These results are quite reasonable and suggest that the transition from prognostic mode to diagnostic mode during deep convection was successful.

The final part of this section will present an overview of the ARM-CART case error statistics (Table 5.1). An ordinal rank is assigned to each experiment based on its overall verification against the independent data from the AC site (Table 5.2). Most of the statistics shown here are generated based on model performance at all five facilities,



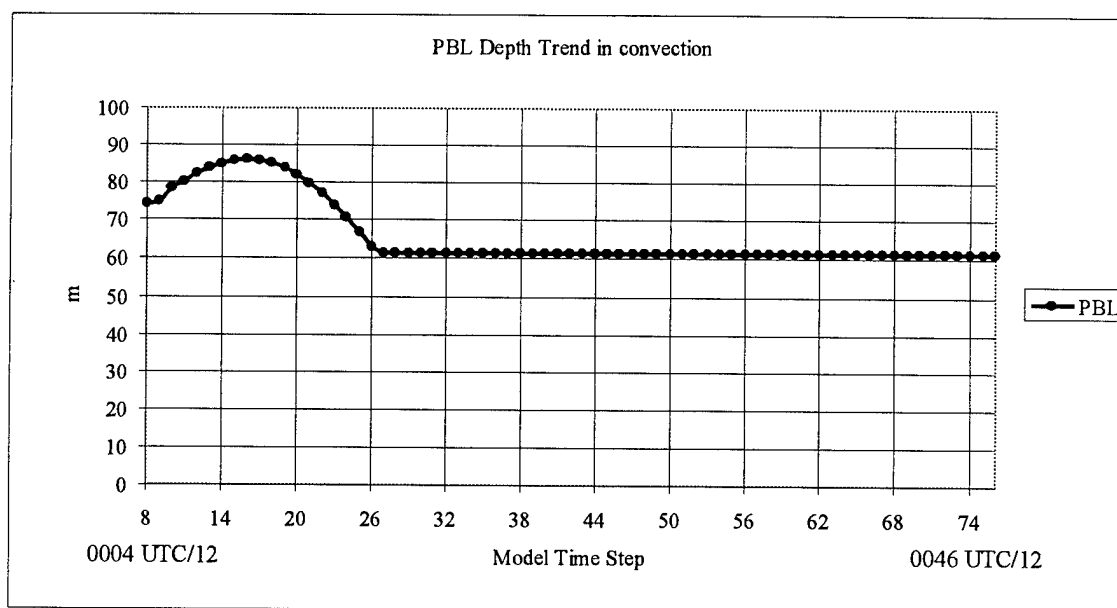


Figure 5.31. Time-series analysis, valid 0004 UTC 12 April 1997 to 0046 UTC 12 April 1997 showing PBL depth during deep convection (diagnosis mode) over southwest Louisiana for Exp. SPB. PBL depths are plotted every time-step (36 s).

Five-Facility	MEAN ERROR				MEAN ABS ERROR				RMS ERROR			
Average Rank	SPB	SPV	BL	GS	SPB	SPV	BL	GS	SPB	SPV	BL	GS
Sfc Layer Wnd Spd	4.0	3.0	2.0	1.0	4.0	3.0	2.0	1.0	4.0	3.0	2.0	1.0
Sfc Layer Wnd Dir	4.0	3.0	1.5	1.5	3.0	3.0	3.0	4.0	2.5	1.0	2.5	4.0
Sfc Layer Temp.	3.0	4.0	2.0	1.0	3.5	3.5	1.0	2.0	3.5	3.5	1.5	1.5
Sfc Layer Spec. Hum.	3.0	3.0	3.0	1.0	2.5	2.5	2.5	2.5	3.5	3.5	1.5	1.5
SUM OF RANKS	14.0	13.0	8.5	4.5	13.0	12.0	8.5	9.5	13.5	11.0	7.5	8.0
SFC LAYER RANK	4.0	3.0	2.0	1.0	4.0	3.0	1.0	2.0	4.0	3.0	1.0	2.0

Five-Facility	MEAN ERROR				MEAN ABS ERROR				RMS ERROR			
Average Rank	SPB	SPV	BL	GS	SPB	SPV	BL	GS	SPB	SPV	BL	GS
900mb Temperature	3.0	4.0	2.0	1.0	3.5	3.5	1.5	1.5	4.0	3.0	1.5	1.5
800mb Temperature	3.5	3.5	2.0	1.0	4.0	3.0	1.5	1.5	3.5	3.5	1.5	1.5
700mb Temperature	4.0	3.0	2.0	1.0	4.0	3.0	1.5	1.5	3.5	3.5	2.0	1.0
900mb Spec. Humidity	3.0	3.0	3.0	1.0	3.5	1.5	1.5	3.5	3.5	3.5	2.0	1.0
800mb Spec. Humidity	1.5	1.5	3.5	3.5	2.5	2.5	2.5	2.5	2.5	2.5	2.5	2.5
700mb Spec. Humidity	3.0	3.0	3.0	1.0	2.0	2.0	2.0	4.0	2.5	2.5	2.5	2.5
SUM OF RANKS	18.0	18.0	15.5	8.5	19.5	15.5	10.5	14.5	19.5	18.5	12.0	10.0
VERTICAL RANK	3.5	3.5	2.0	1.0	4.0	3.0	1.0	2.0	4.0	3.0	2.0	1.0

Central Facility Rank	MEAN ERROR				MEAN ABS ERROR				RMS ERROR			
	SPB	SPV	BL	GS	SPB	SPV	BL	GS	SPB	SPV	BL	GS
Surface Pressure	3.0	4.0	2.0	1.0	4.0	3.0	1.0	2.0	4.0	3.0	1.0	2.0
Surface Rel. Hum.	3.0	4.0	1.0	2.0	3.5	3.5	1.0	2.0	3.5	3.5	1.0	2.0
Net Radiation	4.0	3.0	1.0	2.0	4.0	2.0	3.0	1.0	4.0	3.0	1.0	2.0
Sensible Heat Flux	4.0	3.0	1.0	2.0	4.0	3.0	1.0	2.0	3.5	2.0	1.0	3.5
Latent Heat Flux	4.0	3.0	1.0	2.0	4.0	3.0	1.0	2.0	4.0	3.0	1.0	2.0
Int. Cloud Water	2.0	2.0	4.0	2.0	3.5	3.5	1.5	1.5	2.0	4.0	2.0	2.0
SUM OF RANKS	20.0	19.0	10.0	11.0	23.0	18.0	8.5	10.5	21.0	18.5	7.0	13.5
CF RANK	4.0	3.0	1.0	2.0	4.0	3.0	1.0	2.0	4.0	3.0	1.0	2.0

Five-Facility	MEAN ERROR				MEAN ABS ERROR				RMS ERROR			
Average PBL Depth Rank	SPB	SPV	BL	GS	SPB	SPV	BL	GS	SPB	SPV	BL	GS
0 to 48-h PBL Depth	1.0	2.0	4.0	3.0	1.0	2.0	4.0	3.0	1.0	2.0	4.0	3.0
Nighttime PBL	2.0	1.0	3.0	4.0	1.0	2.0	3.0	4.0	1.0	2.0	3.0	4.0
Daytime PBL	1.0	2.0	3.0	4.0	1.0	2.0	4.0	3.0	1.0	2.0	4.0	3.0
SUM OF RANKS	4.0	5.0	10.0	11.0	3.0	6.0	11.0	10.0	3.0	6.0	11.0	10.0
PBL Depth Rank	1.0	2.0	3.0	4.0	1.0	2.0	4.0	3.0	1.0	2.0	4.0	3.0

	MEAN ERROR				MEAN ABS ERROR				RMS ERROR			
	SPB	SPV	BL	GS	SPB	SPV	BL	GS	SPB	SPV	BL	GS
SUM OF CATEGORY RANKS	12.5	11.5	8.0	8.0	13.0	11.0	7.0	9.0	13.0	11.0	8.0	8.0
GRAND RANK	4.0	3.0	1.5	1.5	4.0	3.0	1.0	2.0	4.0	3.0	1.5	1.5

Table 5.2. ARM-CART case ordinal ranking of experiments.

except for those observations available only at the CF (surface pressure, net radiation, fluxes of sensible and latent heat, and integrated cloud water). These statistics are listed separately. Finally, the comparative computational efficiency of the experiments is addressed.

A close examination of Table 5.1 reveals that the experimental results are fairly comparable. The five-facility averaged mean absolute error over the 48-h period for surface winds vary by  $1 \text{ m s}^{-1}$  and 1 degree for the four experiments. The RMS errors of surface temperature agree to within  $1^\circ\text{C}$  for all four experiments as well, and the surface-layer specific humidity errors vary by only  $0.1 \text{ g kg}^{-1}$ . Errors for the vertical distribution of temperature and moisture show similar comparability. At the AC CF, surface pressure RMS errors vary by less than 1 mb among the four experiments. A significant difference is seen in the mean error of net radiation between the two spectral experiments which have a negative bias of 50 to  $55 \text{ W m}^{-2}$  and Exps. BL and GS which have biases of +3 and  $-9 \text{ W m}^{-2}$  respectively. This is primarily due to forecasts of cloud water which greatly affect timing and magnitude of the radiation forcing. Finally, we see that the PBL depth error produced by the spectral experiments is considerably smaller than the other two experiments, during both nighttime and daytime periods.

Table 5.2 presents ordinal ranks based on the 48-h verification statistics in Table 5.1. These ranks are subdivided into categories including surface-layer variables, vertical temperature and moisture structure, the surface energy budget and PBL depth. A rank is provided for each meteorological field for mean error, mean absolute error, and RMS

error, and these individual ranks are summed to give the category rank. A final overall rank is determined based on the lowest sum of category ranks. In most cases the differences among experimental errors are quite small; thus, the statistical significance of these rankings is not well known. In general, the BL and GS PBL models alternated between best and second best, while the two spectral-model experiments alternated between third and fourth. For PBL depth, however, the spectral models consistently outperformed the other two models. Again, it cannot be determined within the scope of this work whether the differences between the spectral and "high-resolution" experiments are the result of the spectral architecture or the choice of closure.

Figure 5.32 compares the normalized total MM5 computation time for each of the experiments in the ARM-CART case. The spectral model reduces total computation time by 10-14 percent over the other two "high-resolution" PBL models. As in the idealized case (Fig. 5.15) this means the spectral model is several times faster than the other PBL models tested. The apparent difference of efficiency between the spectral and non-spectral experiments was 25 percent in the idealized case. This difference is most likely reduced in this real-data case by the necessity for the spectral model to diagnose the PBL depth for grid-points experiencing deep convection, while no convection was present in the idealized case. Moreover, as a result of the variety of meteorological conditions across the domain through the forecast period, more computation time is spent in non-PBL physics modules thereby reducing the relative contribution of the PBL scheme to the total computation time.

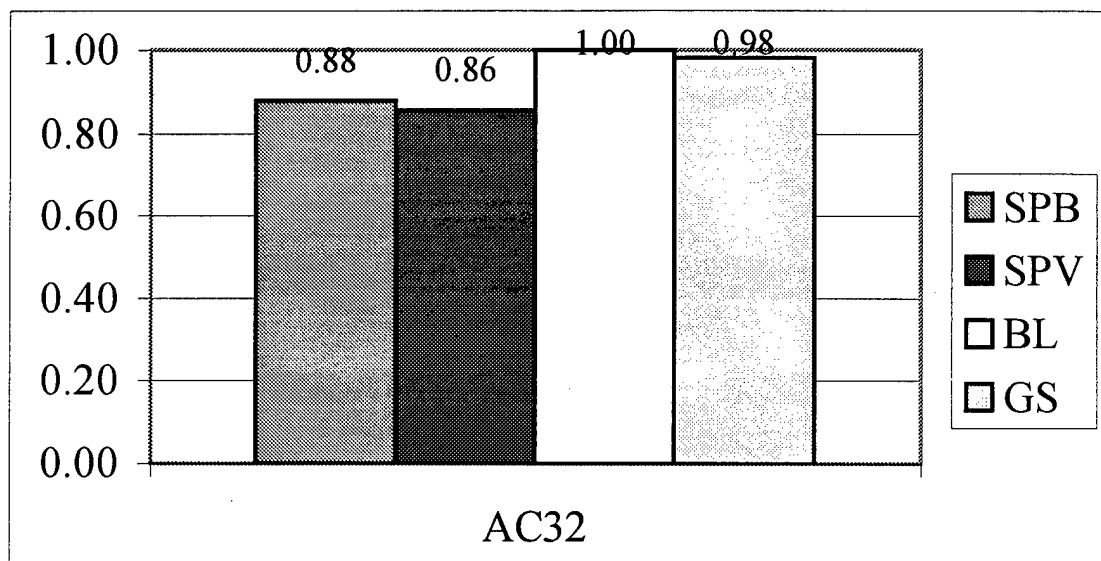


Figure 5.32. Normalized total MM5 computation time for ARM-CART case experiments.

## Chapter 6 SUMMARY AND CONCLUSIONS

### 6.1 Summary

Bulk or integral PBL models such as the mixed-layer model are very fast computationally, but oversimplify the vertical structure of mean atmospheric properties within the boundary layer. Conversely, high-resolution (multi-layer) schemes like the Blackadar and Gayno-Seaman PBL models attempt to realistically describe the vertical structure within the PBL, yet account for a significant percentage (25 percent or more) of the total model computation time. The Otte-Wyngaard spectral PBL model is an attempt to realistically describe the vertical structure of the boundary layer in a computationally efficient manner.

This work developed and tested the Otte-Wyngaard spectral PBL scheme, which uses a prognostic equation for PBL height for use within the framework of the three-dimensional MM5 for the first time. Using idealized conditions in the first case, the spectral model produced realistic solutions for a coastal-zone environment. A layer of marine stratus, which sloped downwards towards the idealized coastline, formed within the first 12 hours of the experiment and persisted through the remainder of the 24-h period, in agreement with the two "high-resolution" models and conditions expected based on climatology (Neiburger et al. 1961). Nocturnal cooling resulted in the formation of a radiation inversion over land, and daytime radiative heating then deepened the land boundary layer, dissipated cloud and fog which had formed there in the morning hours, and forced the onset of a sea-breeze circulation. The depth of the PBL, the extent, duration, and concentration of cloud water, the magnitude of horizontal and vertical

gradients of temperature, and the strength of the sea-breeze after 24 hours were reasonable, and comparable to those generated by the Blackadar and Gayno-Seaman models. The production of all of these phenomena by the spectral model within MM5 indicated a successful coupling of the spectral PBL architecture with the MM5, and a proper interaction of the PBL model with the non-PBL MM5 physics and dynamics modules. This work demonstrated proof-of-concept of the spectral architecture. It must be emphasized that the specific PBL closure used within this general framework can easily be upgraded.

Although the vertical structure of atmospheric properties within the spectral PBL model is represented by Legendre polynomials, reducing vertical grid-space resolution still had a negative impact on the ability of this model to describe the boundary layer and inversion strength. The spectral scheme responded to reduced vertical grid resolution by weakening the vertical gradients, which reduced the "jump" of model variables across the inversion which, in part, weakened the intensity of the entrainment. A secondary, but no less important, manifestation of the effect of decreased vertical grid-space resolution involved the non-PBL physics. It was more difficult to saturate thicker model layers, causing cloud layers to form more slowly and with lower concentrations of cloud water which, in turn, had an impact on longwave and shortwave radiation. This effect was apparent in all three PBL schemes.

The second case used real data and introduced the effects of complex terrain and a variety of atmospheric stability conditions. Preliminary experiments indicated the failure of the prognostic PBL height equation during deep convection. This prompted the

evaluation of several algorithms for *diagnosis* of PBL depth at grid points experiencing deep convection, as well as to initialize the PBL depth field.

The differences in the evolution of the boundary-layer depth prognosed by the two versions of the spectral model tested here revealed a marked sensitivity to the initial diagnosis of PBL depth. Because the depth of the PBL determines the depth over which the spectral parameterization operates within the MM5, these differing PBL trends resulted in distinctly different cloud forecasts and, hence, very different radiative and thermal properties. Moreover, the spectral PBL model's prognosis of PBL depth is numerically complex, and may differ considerably from that *diagnosed* from the model's mass and wind profiles, as was found during deep convection.

Verification of this real-data case with independent special data from the ARM-CART site appeared to indicate that the Blackadar and Gayno-Seaman PBL models more accurately described many of the meteorological fields, compared to the spectral model. However, the differences among experiments were often small, making the statistical ranking of experiments deceptive. The spectral model appeared to describe the cloud cover over the ARM-CART site more realistically than the other two models, producing more cloud the first day than the second day, as observed. The version of the spectral model that used the Bulk-Richardson method (Vogelezang and Holtslag, 1996) for initial diagnosis even generated two distinct maxima of integrated cloud water; however, the timing of these maxima differed somewhat from that measured by a microwave radiometer. The large sensitivity to differences in timing between observed cloud and cloud generated by the model adversely affected the evolution of net radiation, surface



fluxes (which drive entrainment fluxes) and surface-layer temperature. It was noted that the spectral model produced a weaker diurnal cycle of surface-layer temperature trend than that observed or generated by the other models, as would be expected with more cloud cover.

The results from both the idealized coastal-zone case and the real-data case demonstrated that the spectral model is several times faster than either the Blackadar or Gayno-Seaman PBL models, reducing total MM5 computation time by 15-25 percent over the "high-resolution" models, while describing generally comparable realistic vertical structure within the boundary layer.

## 6.2 Future Work

Because only one real-data case with verification using independent data was studied here, the Otte-Wyngaard spectral PBL model must undergo further testing. A logical next step is to study the ability of the model to describe the structure and evolution of the marine boundary layer in a real-data case. Many more cases will be needed to determine the general applicability of the spectral PBL in MM5.

In addition, it was shown that the boundary-layer structure within the spectral model was still dependent upon vertical grid resolution, possibly due to the entrainment calculations. Many widely used PBL models have difficulty producing accurate entrainment properties (Ayotte et al. 1996); thus it is of critical importance that the inversion layer be handled more realistically so that there is less sensitivity of the entrainment effects to the vertical grid resolution. A spectral model currently under

development at Penn State is expected to better represent the sub-gridscale physics of the interfacial layer and improve entrainment calculations (Otte 1998, personal communication).

This study also revealed a weakness of both the Blackadar and Gayno-Seaman models during stable conditions, when they set the PBL depth to zero when it may not be zero. Implementation of the Bulk-Richardson diagnosis method of Vogelesang and Holtslag (1996) within these PBL schemes during stable conditions should be tested.

## REFERENCES

- Abramowitz, M. and I. A. Stegun, 1970: *Handbook of Mathematical Functions*. U.S. Government Printing Office, 1046 pp.
- Ayotte, K. W., P. P. Sullivan, A. Andr  n, S. C. Doney, A. A. M. Holtslag, W. G. Large, J. C. McWilliams, C.-H. Moeng, M. J. Otte, J. J. Tribbin, and J. C. Wyngaard, 1996: An evaluation of neutral and convective planetary boundary-layer parameterizations relative to large eddy simulations. *Boundary-Layer Meteorol.*, **79**, 131-175.
- Banta, R. M., 1995: Sea breezes shallow and deep on the California coast. *Mon. Wea. Rev.*, **123**, 3614-3622.
- Betts, A. K., 1973: Non-precipitating cumulus convection and its parameterization. *Quart. J. Roy. Meteor. Soc.*, **99**, 178-196.
- Blackadar, A. K., 1976: Modeling the nocturnal boundary layer. *Preprints of Third Symposium on Atmospheric Turbulence and Air Quality*, Raleigh, NC, 19-22 October 1976, Amer. Meteor. Soc., Boston, 46-49.
- Blackadar, A. K., 1979: High-resolution models of the planetary boundary layer. *Advances in Environmental Science and Engineering*, 1, No. 1. Pfafflin and Ziegler, Eds., Gordon and Breach Sci. Publ., New York, 50-85.
- Burden, R. L., J. D. Faires, and A.C. Reynolds, 1981: Numerical Analysis, Second Edition. Prindle, Weber and Schmidt. Boston, MA 598 pp.
- Dudhia, J., 1989: Numerical study of convection observed during the winter monsoon experiment using a mesoscale two-dimensional model. *J. Atmos. Sci.*, **46**, 3077-3107.
- Dudhia, J., 1993: A nonhydrostatic version of the Penn State/NCAR mesoscale model: Validation tests and simulation of an Atlantic cyclone and cold front. *Mon. Wea. Rev.*, **121**, 1493-1513.
- Fiedler, B. H., and C.-H. Moeng, 1985: A practical integral closure model for the mean vertical transport of a scalar in a convective boundary layer. *J. Atmos. Sci.*, **42**, 359-363.
- Gayno, G. A., 1994: Development of a higher-order, fog producing boundary layer model suitable for use in numerical weather prediction. *M.S. Thesis, The Pennsylvania State University*, 104pp.

- Gayno, G. A., N. L. Seaman, A. M. Lario and D. R. Stauffer, 1994: Forecasting visibility using a 1.5 order closure boundary layer scheme in a 12-km non-hydrostatic model. *Preprints, Tenth Conference on Numerical Weather Prediction*, Portland, Oregon, Amer. Meteor. Soc., July 17-22, 18-20.
- Grell, G. A., J. Dudhia, D. R. Stauffer, 1994: A description of the fifth-generation Penn State/NCAR mesoscale model (MM5). *NCAR Technical Note-398+STR*, National Center for Atmospheric Research (NCAR), Boulder, 138pp.
- Kain, J. S., and Fritsch, J. M., 1993: Convective parameterization in mesoscale models: The Kain-Fritsch scheme. *The representation of cumulus convection in numerical models*, AMS monogram., K.A. Emanuel, and D.J. Raymond, EDS., 165-170.
- Leidner, S. M., 1995: Improving California coastal-zone numerical weather prediction by dynamic initialization of the marine boundary layer. *M.S. Thesis, The Pennsylvania State University*, 158 pp.
- Leidner, S. M., and D. R. Stauffer, 1996: Improving California coastal-zone forecasting by initialization of the marine boundary layer. *Preprints, Eleventh Conference on Numerical Weather Prediction*, Norfolk, VA, Amer. Meteor. Soc. 177-179.
- Lilly, D. K., 1968: Models of cloud-topped mixed layers under a strong inversion. *Quart. J. Roy. Meteor. Soc.*, **94**, 292-309.
- Mass, C. F., and Y.-H. Kuo, 1998: Regional real-time numerical weather prediction: current status and future potential. *Bull. Amer. Meteor. Soc.*, **79**, 253-263.
- Mellor, G. L., and T. Yamada, 1974: A hierarchy of turbulence closure models for the planetary boundary layer. *J. Atmos. Sci.*, **31**, 1791-1806.
- Moeng, C.-H., and P. P. Sullivan, 1994: A comparison of shear and buoyancy driven planetary boundary layer flows. *J. Atmos. Sci.*, **51**, 999-1022.
- Neiburger, M., D. Johnson and C. Chien, 1961: *Studies of the Structure of the Atmosphere Over the Eastern Pacific Ocean in Summer: I Inversion Over the Eastern North Pacific Ocean*, Univ. Calif. Publ. Meteor., **1**, No. 1, 94 pp.
- Nicholls, S., 1984: The dynamics of stratocumulus: Aircraft observations and comparisons with a mixed layer model. *Quart. J. Roy. Meteor. Soc.*, **110**, 783-820.
- Nieuwstadt, F. T. M., and H. Tennekes, 1981: A rate equation for the nocturnal boundary-layer height. *J. Atmos. Sci.*, **38**, 1418-1428.

- Otte, M. J. and J. C. Wyngaard, 1996: A general framework for an "Unmixed Layer" PBL model. *J. Atmos. Sci.*, **53**, 2652-2670.
- Slingo, A., 1989: A GCM parameterization for the shortwave radiative properties of water clouds. *J. Atmos. Sci.*, **46**, 1419-1427.
- Stauffer, D. R., M. J. Otte, D. T. Pawlak, and J. C. Wyngaard, 1997: A New Spectral Boundary-Layer Parameterization for the MM5: Coupling Methodology and Performance Evaluations, *Preprints, Twelfth Conference on Numerical Weather Prediction*, Phoenix, AZ, Amer. Meteor. Soc. 124-127.
- Stephens, G. L., 1984: The parameterization of radiation for numerical weather prediction and climate models. *Mon. Wea. Rev.*, **112**, 826-867.
- Stroud, A. H., 1974: Numerical Quadrature and Solution of Ordinary Differential Equations, *Applied Mathematical Sciences*, Vol. 10, Springer-Verlag New York, Heidelberg, Berlin, 338pp.
- Stull, R. B., 1984: Transilient turbulence theory. Part I: The concept of eddy mixing across finite distances. *J. Atmos. Sci.*, **41**, 3351-3367.
- U.S. Department of Energy, 1997: Atmospheric Radiation Measurement Fact sheet, 1997.
- Vogelezang, D. H. P., and A. A. M. Holtslag, 1996: Evaluation and model impacts of alternative boundary-layer height formulations. *Boundary-Layer Meteorol.*, **81**, 245-269.
- Williams, R. T., N. L. Seaman, D. R. Stauffer, and J. C. Wyngaard, 1997: Mesoscale simulation of electromagnetic refractivity in surface and elevated ducts during the VOCAR experiment., *Preprints, Second Conference on Coastal Atmospheric and Oceanic Prediction and Processes*, Phoenix, AZ, Amer. Meteor. Soc. 122-126.
- Wyngaard, J. C., and R. A. Brost, 1984: Top-down and bottom diffusion of a scalar in the convective boundary layer. *J. Atmos. Sci.*, **44**, 102-112.
- Zeman, O., 1979: Parameterization of the dynamics of stable boundary layers and nocturnal jets. *J. Atmos. Sci.*, **36**, 792-804.
- Zhang, D. L. and R.A. Anthes, 1982: A high-resolution model of the planetary boundary layer-sensitivity tests and comparison with SESAME-79 data. *J. Appl. Meteor.*, **114**, 1330-1339.